Metal-Organic Frameworks for the CO2 Reduction Reaction

A Selectivity Study

Roohi, K.

DOI
10.4233/uuid:e6fefbf7-6bc1-4a8c-a019-b44e212435d4

Publication date
2025

Document Version
Final published version

Citation (APA)
Roohi, K. (2025). *Metal-Organic Frameworks for the CO2 Reduction Reaction: A Selectivity Study* . [Dissertation (TU Delft), Delft University of Technology]. https://doi.org/10.4233/uuid:e6fefbf7-6bc1-4a8c-a019-b44e212435d4

METAL-ORGANIC FRAMEWORKS FOR THE CO_2 REDUCTION REACTION

A SELECTIVITY STUDY

METAL-ORGANIC FRAMEWORKS FOR THE CO_2 REDUCTION REACTION

A SELECTIVITY STUDY

Dissertation

for the purpose of obtaining the degree of doctor
at Delft University of Technology
by the authority of the Rector Magnificus, prof.dr.ir. T.H.J.J. van der Hagen,
chair of the Board for Doctorates
to be defended publicly on Wednesday 7 January 2026 at 15:00 o'clock

by

Khatereh ROOHI

Master of Science in Catalysis Engineering, Amirkabir University of Technology (Tehran Polytechnic), Iran
born in Ghazvin, Iran

This dissertation has been approved by the promotors.

Composition of the doctoral committee:

Prof. dr. ir. H.H.G. Savenije	Chairman
Prof. dr. ir. J.M.C Mol,	Delft University of Technology, *promotor*
Dr. P. Taheri,	Delft University of Technology, *promotor*
Independent members:	
Dr. N. Shepelin	Paul Scherrer Institute (PSI)
Prof. dr. P. P. Pescarmona	University of Groningen
Dr. ir. M. A. van der Veen	Delft University of Technology
Prof. dr. ir. T. J. H. Vlugt ,	Delft University of Technology
Dr. K. R. Rossi,	Delft University of Technology

Keywords: Atomic-Scale Modification, Selectivity, Metal-Organic Frameworks, CO_2 Reduction Reaction

Printed by: Ridderprint

Cover by: Khatereh Roohi

ISBN 978-94-6518-210-0

An electronic copy of this dissertation is available at
https://repository.tudelft.nl/.

Just another brick in the vast wall of science, laid with care and curiosity.

CONTENTS

SUMMARY

The rising concentration of atmospheric carbon dioxide (CO_2), primarily caused by fossil fuel combustion, poses a major challenge to climate stability. Among various strategies for mitigating CO_2 emissions, the electrochemical CO_2 reduction reaction (CO_2RR) has emerged as a promising technology for converting CO_2 into energy-rich products such as carbon monoxide and formate, using renewable electricity. Despite its potential, CO_2RR suffers from sluggish kinetics, low product selectivity, and parasitic hydrogen evolution, making the development of efficient and stable electrocatalysts a central focus of current research.

This dissertation explores how metal-organic frameworks (MOFs), owing to their modular design and tunable coordination environments, can be transformed into highly selective electrocatalysts for CO_2RR. MOFs offer a unique structural platform where metal nodes and organic linkers can be independently tailored to tune catalytic properties at the atomic level. However, their low intrinsic conductivity and limited mechanistic understanding have so far hindered their widespread application in electrocatalysis. Especially in the case of copper, which remains the most intrinsically active and extensively studied catalyst for CO_2RR, linear scaling relationship (LSR) between key intermediates of the reaction, imposes fundamental limitations on selectivity, presenting a major obstacle for its industrial application.

To address these limitations, this research investigates a series of rational design strategies for enhancing MOF performance in CO_2RR. One key direction involves tailoring the coordination geometry and electronic environment of copper sites. By introducing sulfur-based ligands in place of traditional carboxylates, it is shown that the local structure of the Cu centers can be engineered to favor formate formation. In particular, the development of a novel quasi-two-dimensional CuSBDC framework was achieved via a one-pot synthesis incorporating methylthiol ligands, demonstrating that sulfur coordination plays a decisive role in stabilizing the *OCHO intermediate while suppressing competing hydrogen evolution. Density functional theory (DFT) simulations confirm that these compositional modifications alter intermediate binding energetics and improve the overall electronic structure, resulting in high Faradaic efficiencies for formate with negligible CO production.

Another strategy explored in this work focuses on fine-tuning the copper coordination environment within the same MOF. By reducing the coordination number from five to four through selective removal of an axial oxygen ligand, a significant shift in product selectivity from CO to formate was observed. Operando Raman spectroscopy and DFT were employed to monitor the interfacial reaction intermediates in real time, revealing a distinct spectroscopic fingerprint for the *OCHO intermediate on the surface of a copper-based catalyst. In parallel, the dissertation explores conductivity enhancement strategies to overcome electron-transport bottlenecks. By integrating Cu-MOFs with conductive

carbon nanotubes, composite electrodes are created that combine high selectivity with significantly improved current densities. Furthermore, post-synthetic carbonization of two-dimensional Cu-MOFs is used to generate conductive, porous carbons. The degree of carbonization and precursor chemistry are found to influence not only electrical conductivity, but also morphology, copper dispersion, and heteroatom retention, affecting CO_2RR performance.

In summary, this dissertation demonstrates that the electrocatalytic performance of MOFs for CO_2RR can be significantly enhanced through precise structural and chemical modifications. In particular, it highlights how the local coordination environment, linker composition, and overall framework topology can be engineered to selectively stabilize specific reaction intermediates. Such structural control is especially critical in multi-intermediate reactions like CO_2 reduction, where small changes in the electronic or geometric structure of the catalyst can tip the balance between competing pathways. By systematically tuning copper coordination, introducing heteroatoms, and forming conductive composites, this work establishes MOFs as powerful model systems for probing and directing product selectivity. These findings provide valuable mechanistic insights and design guidelines that contribute to the development of next-generation catalysts for sustainable CO_2 conversion.

SAMENVATTING

De stijgende concentratie van koolstofdioxide (CO_2) in de atmosfeer, voornamelijk veroorzaakt door de verbranding van fossiele brandstoffen, vormt een grote uitdaging voor de stabiliteit van het klimaat. Onder de verschillende strategieën om CO_2-emissies te beperken, is de elektrochemische CO_2-reductiereactie (CO_2RR) naar voren gekomen als een veelbelovende technologie voor het omzetten van CO_2 in energierijke producten zoals koolmonoxide en formiaat, met behulp van hernieuwbare elektriciteit. Ondanks dit potentieel, wordt CO_2RR gehinderd door trage reactiemechanismen, lage productselectiviteit en concurrerende waterstofvorming, waardoor de ontwikkeling van efficiënte en stabiele elektrokatalysatoren een centraal aandachtspunt is binnen het huidige onderzoek.

Dit proefschrift onderzoekt hoe metaal-organische roosters (MOFs), dankzij hun modulaire opbouw en afstembare coördinatieomgevingen, kunnen worden omgevormd tot uiterst selectieve elektrokatalysatoren voor CO_2RR. MOFs bieden een uniek structureel platform waarbij metaalclusters en organische liganden onafhankelijk van elkaar kunnen worden aangepast om katalytische eigenschappen op atomaire schaal te sturen. Hun intrinsiek lage geleidbaarheid en het beperkte mechanistische inzicht in hun gedrag hebben hun brede toepassing in de elektrokatalyse echter tot nu toe belemmerd. Vooral in het geval van koperde intrinsiek meest actieve en meest onderzochte katalysator voor CO_2RRvormt de lineaire schaalrelatie (LSR) tussen sleuteltussenproducten van de reactie een fundamentele beperking voor de selectiviteit, wat een groot obstakel vormt voor industriële toepassing.

Om deze beperkingen aan te pakken, onderzoekt dit onderzoek een reeks rationele ontwerpstrategieën om de prestaties van MOFs in CO_2RR te verbeteren. Een belangrijke aanpak richt zich op het aanpassen van de coördinatiegeometrie en de elektronische omgeving van kopercentra. Door zwavelhoudende liganden in plaats van traditionele carboxylaatgroepen in te voeren, wordt aangetoond dat de lokale structuur van de Cu-centra zodanig kan worden ontworpen dat formiaatvorming wordt bevorderd. In het bijzonder werd een nieuw quasi-tweedimensionaal CuSBDC-rooster ontwikkeld via een éénpotsynthese met methylthiool-liganden, waarmee wordt aangetoond dat zwavelcoördinatie een beslissende rol speelt in de stabilisatie van het *OCHO-intermediair en de onderdrukking van concurrerende waterstofvorming. Dichtheidsfunctionaaltheorie (DFT)-simulaties bevestigen dat deze compositie-aanpassingen de bindingsenergietermodynamica van tussenproducten veranderen en de elektronische structuur verbeteren, wat leidt tot hoge Faradische efficiëntie voor formiaat met verwaarloosbare CO-productie.

Een andere strategie in dit werk richt zich op het verfijnen van de kopercoördinatie binnen hetzelfde MOF-systeem. Door het coördinatiegetal van vijf naar vier te verlagen via selectieve verwijdering van een axiale zuurstofligand, werd een duidelijke verschuiving in productspecificiteit van CO naar formiaat waargenomen. Operando Raman-

spectroscopie en DFT werden ingezet om de intermediaire reactieproducten aan het oppervlak in real-time te volgen, waarbij een onderscheidende spectroscopische vingerafdruk voor het *OCHO-intermediair op een koper-oppervlak werd geïdentificeerd. Parallel hieraan worden in het proefschrift strategieën onderzocht om de geleidbaarheid te verbeteren en elektronische bottlenecks te overwinnen. Door Cu-MOFs te integreren met geleidende koolstofnanobuisjes, worden composietelektroden gecreëerd die hoge selectiviteit combineren met aanzienlijk verbeterde stroomdichtheden. Daarnaast wordt post-synthetische carbonisatie van tweedimensionale Cu-MOFs toegepast om geleidende, poreuze koolstofmaterialen te genereren. De mate van carbonisatie en de keuze van precursor blijken invloed te hebben op zowel de elektrische geleidbaarheid als op de morfologie, koperverdeling en retentie van heteroatomen, wat uiteindelijk de CO_2RR-prestaties beïnvloedt.

Samenvattend toont dit proefschrift aan dat de elektrokatalytische prestaties van MOFs voor CO_2RR aanzienlijk kunnen worden verbeterd door precieze structurele en chemische modificaties. In het bijzonder wordt benadrukt hoe de lokale coördinatieomgeving, ligandensamenstelling en algemene roosterstructuur kunnen worden ontworpen om specifieke reactietussenproducten selectief te stabiliseren. Dergelijke structurele controle is van cruciaal belang bij multi-intermediaire reacties zoals CO_2-reductie, waarbij kleine veranderingen in de elektronische of geometrische structuur van de katalysator het evenwicht tussen concurrerende reactiekanalen kunnen bepalen. Door systematisch kopercoördinatie aan te passen, heteroatomen te introduceren en geleidende composieten te vormen, positioneert dit werk MOFs als krachtige modelsystemen voor het bestuderen en sturen van productspecificiteit. Deze bevindingen bieden waardevolle mechanistische inzichten en ontwerpprincipes die bijdragen aan de ontwikkeling van katalysatoren van de volgende generatie voor duurzame CO_2-conversie.

1

INTRODUCTION

1

The escalating concentration of Carbon dioxide (CO_2) in the atmosphere, having risen from 280 ppm in the early 1800s to 405 ppm in recent years, poses a severe threat to global climate stability [1]. This issue is mostly due to combustion of fossil fuels, causing global warming, ocean acidification and the risk of catastrophic climate events. To mitigate the CO_2 impacts and prevent further global warming, it is crucial to reduce net anthropogenic CO_2 emissions to zero [2, 3]. Achieving this target requires reducing total CO_2 emissions by shifting the consumption paradigm from traditional fossil fuels to low-carbon energy sources such as nuclear, wind, and solar. However, the intrinsic intermittency of solar or wind resources requires long-term and large-scale storage for their further deployment as replacements for fossil fuels [4], whereas nuclear power development is hampered by public sentiment over its safety, and the disposal of its radioactive by-products [5]. Therefore, considerable research has been conducted on the topic of developing techniques for consumption of CO_2 as an alternative solution. So far, various approaches have been established for converting CO_2 into valuable products. These techniques include biological processes [6], chemical processes such as hydrogeneration [7], carboxylation with CO_2 [8], mineralization [9], photochemical processes [10], plasma technologies [11], and electrochemical methods [12]. Among these, thermochemical and photochemical methods have been extensively explored, but both face significant limitations. Thermochemical CO_2 conversion typically requires high temperatures, high pressures, and an external supply of hydrogen, which limits its feasibility at scale due to energy intensity [13]. Photochemical routes, while conceptually appealing, often suffer from low product selectivity and insufficient conversion rates [14]. In contrast, electrochemical CO_2 reduction has emerged as a particularly attractive strategy, owing to its ability to operate under mild conditions and its tunable reaction rate via applied potential.

1.1. ELECTROCHEMICAL CO_2 REDUCTION REACTION

While fossil fuels will remain a major energy source, electrochemical CO_2RR offers a pathway to convert CO_2 into fuels and value-added chemicals. Employing renewable energy resources, such as wind and solar power, CO_2RR provides a simple and sustainable way to close the carbon-neutral cycle as shown in Fig. 1.1 [15, 16]. Among various methods by which CO_2 can be converted into valuable products, electrochemical CO_2RR stands out due to its:

- Compatibility with renewable energy sources like solar and wind power [17],
- Ability to produce valuable fuels and chemicals such as carbon monoxide, formic acid, alcohols, and hydrocarbons [18],
- Simple, scalable process that can operate under mild conditions [19],
- Highly manageable reaction steps, enabling the adjustment of electrochemical parameters with a relatively high level of efficiency in conversion [20],
- Products are heavily utilized in petrochemical-based processes - e.g. syngas as a building block - or as fuels, thus, no new infrastructure is needed [21].

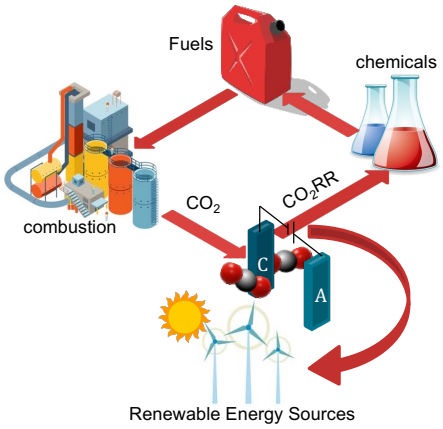

Figure 1.1: Schematic of the carbon-neutral cycle, in which CO_2 generated from fuel combustion is converted back into fuels through an electrochemical process powered by renewable energy sources.

Direct electroreduction of CO_2 is particularly promising as it allows for conversion to products that can be integrated into existing carbon recycling systems and offer opportunities for renewable energy storage [22]. This technology enables the production of various chemical feedstocks or materials for recycling within industrial plants, including carbon monoxide (CO), methane (CH_4), ethylene (C_2H_4), methanol (CH_3OH), ethanol (CH_3CH_2OH), and formic acid (HCOOH) [23]. Products such as alcohols and formic acid can be sold on commodity markets, while CO or syngas can be recycled as carbon feedstock to lower production costs and CO_2 emissions [24]. CO_2RR is a multi-electron process that results in a variety of products depending on the numbers of electrons and protons present in the reaction which are listed in table 1.1 [25]. The particular product or range of products varies based on the nature of the catalytic material. For instance, 16 different products have been identified in the case of metallic copper as an electrocatalyst [26].

Additionally, CO_2RR involves a complex mechanism with sluggish reaction kinetics. Given that CO_2 molecule has an extraordinarily stable linear structure, substantial negative potential is needed to turn adsorbed CO_2 molecules into $*CO_2^-$, which may further be transformed into a variety of chemicals or intermediates [27]. This step is usually considered to be the rate determining step (RDS) in CO_2 conversion reaction. Another key challenge of CO_2RR is the competitve hydrogen evolution reaction (HER) from the electrolysis of water, which occurs at the interface of the cathode/electrolyte in aqueous media together with CO_2RR (See Fig. 1.2). HER occupies catalytic active sites that could otherwise interact with CO_2, significantly reducing the efficiency of CO_2 reduction [28]. Moreover, as a multi-electron (2-12 electrons) transfer process involving multiple intermediates, CO_2 can thermodynamically be reduced to a mixture of C_1, C_2, and C_3 products; however, achieving selectivity toward a specific product remains challenging [27]. To decrease the post-reaction separation costs, selectivity is

the key parameter.

Table 1.1: Standard redox potentials for CO_2 reduction related half reactions [25, 29].

Half reactions	E° (V vs. RHE)
$CO_2 + 2H^+ + 2e \rightarrow HCOOH$	-0.2 (for pH < 4)
$CO_2 + 2H^+ + 2e \rightarrow CO + H_2O$	-0.1
$CO_2 + 4H^+ + 4e \rightarrow HCHO + H_2O$	-0.07
$CO_2 + 6H^+ + 6e \rightarrow CH_3OH + H_2O$	0.02
$CO_2 + 8H^+ + 8e \rightarrow CH_4 + 2H_2O$	0.17
$CO_2 + 12H^+ + 12e \rightarrow CH_2CH_2 + 4H_2O$	0.08
$CO_2 + 12H^+ + 12e \rightarrow CH_3CH_2OH + 3H_2O$	0.09

A catalyst, by definition, is a substance that enables a chemical reaction to occur or increase its rate without being consumed in the reaction. It is mainly considered to be the meeting point of the reactants with each other, as well as the place where intermediates and products form [30]. To evaluate the performance of a CO_2RR catalyst, key parameters include Faradaic efficiency (FE), activation overpotential, and current density. FE measures the selectivity of the reaction for a specific product, overpotential reflects the activity of the catalyst by comparing applied and thermodynamic potentials (see table 1.1), and current density represents the rate of reaction, normalized to the electrochemically active surface area [31]. The ideal catalyst material would actively, selectively, and effectively convert CO_2 into valuable chemicals [1]. Activity and selectivity are vital catalytic parameters with respect to the rate of conversion and the preference of the catalytic material toward a single reaction pathway. While some noble metals, such as Au, Ag, and Pd, are highly preferential toward CO_2RR over HER, their scarcity and high price hinder their applicability as industrial electrocatalysts [32]. Thus, it is widely accepted that CO_2RR electrocatalysts should be inexpensive, possess abundant active sites, be electrically conductive, preferentially favor CO_2RR over HER, and have a high surface area while producing only one CO_2RR product.

Pioneering investigations on CO_2RR catalysis, by Hori et al. [33], have shown that among all transition metals, copper-based electrodes exhibit the highest catalytic activity in converting CO_2 into valuable chemicals. Based on their studies, metal catalysts could be split into four categories of 1) CO-catalysts (such as Au, Ag, Zn), 2) formate-catalysts (such as Pb, In, and Sn), 3) Non-active catalysts (such as Fe, Pt, and Ni) and lastly, Cu. Copper, among all transition metals, is capable of producing a mixture of hydrocarbons, alcohols, and CO. In general, transition metals and metal oxides have been widely investigated for the electrochemical reduction of CO_2 [34]. This is due to vacant orbitals and active d electrons, which are able to energetically facilitate the bonding between the metal and the CO_2. However, the limitations of bulk metals in many terms such as electrochemical active surface area, reaction rate and in case of Cu, poor carbon-based product selectivity, necessitate further manipulation of metal structures. Therefore, the focus of catalyst research in CO_2RR studies has gradually shifted from Hori's initial research to investigating the structural effects on reaction activity and pathway rather than material properties [35, 36].

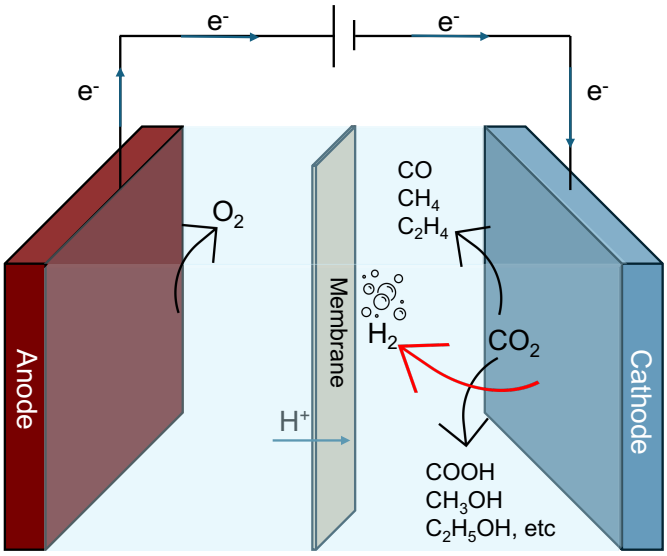

Figure 1.2: Schematic of a CO_2RR electrolyzer

1.2. IMPORTANCE OF SELECTIVITY IN CO_2 REDUCTION

In contrast to the HER, CO_2RR still requires significant research and development to become a mature technology. Challenges related to efficiency, selectivity, and conversion rate must be addressed for electrochemical CO_2RR to be a viable option for a renewable future. These challenges can be systematically studied and optimized from various perspectives-namely, the focus of this dissertation, which examines how the proper design of electrocatalysts can contribute to overcoming these limitations [37]. A key question that arises is how an electrocatalyst can be designed to enhance the process. Poor selectivity can pose a significant challenge, as the cost of separating products from a catalyst with low selectivity, even if it exhibits high activity, can render the process economically unfeasible. Unless a highly efficient method is developed to selectively produce higher-carbon products with exceptionally high FEs, a more viable approach would be to prioritize the production of key chemical building blocks, such as formate/formic acid and CO. These intermediates can then be upgraded through well-established chemical and electrochemical processes, such as Fischer-Tropsch synthesis [38]. Advancing both selective catalysis and efficient separation technologies in tandem is essential for developing sustainable CO_2RR [39]. When it comes to multiproduct reactions, the interaction of key intermediates with the catalyst could determine the reaction pathway and its selectivity [31]. In any catalytic reaction, it is widely known that the bonding strength of the reaction species (i.e., reactants, intermediates, and products) to the surface of the catalyst should strike a balance neither too strong nor too weak [40].

Three key intermediates of the CO_2RR are *COOH, *CO and *COH (as shown in dashed red boxes in Fig. 1.3). The bond order conservation theory and the electron

counting rules suggest that the bonding energies of intermediates to the surface of the metal catalysts are interconnected linearly [40, 41]. This universal concept is called linear scaling relationship (LSR) and has been practically calculated for transition metal (TM) catalysts in CO_2RR. LSR of the binding energies of *CO, *COOH and *CHO is largely responsible for the modest FE of copper catalysts in CO_2RR. Regulating the binding energies of these intermediates on the surface of the electrocatalyst can enhance the FE of carbonous products [42]. In this regard, many techniques from alloying, doping, metal/metal oxide interfaces, grain boundaries, facets and many other structure-oriented modifications have been used to achieve this control [43].

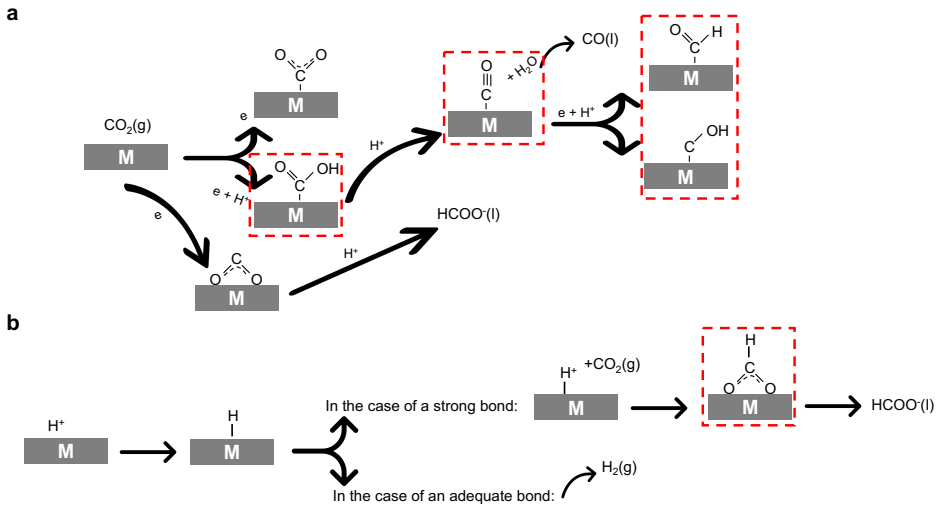

Figure 1.3: Plausible pathways of CO_2RR (M = Metal), **a**, pathways to CO and HCOOH, **b**, pathway of CO_2RR to formate and HER in case of adsorption of H+ on the surface of the metal [44]. Dashed red boxes are representatives of key intermediates of CO_2RR.

1.3. IMPORTANCE OF TARGETED PRODUCTS IN CATALYST DESIGN

Targeted products in catalytic CO_2RR, fundamentally dictate the nature of the catalyst materials and design strategies, influencing surface properties, electronic structure, and active site composition. For example, in the most recent studies in the field [45, 46], it has been shown that the formation of long-chain hydrocarbons requires a catalyst capable not only of CO_2 activation but also Fischer-Tropsch-like polymerization, which is not efficiently facilitated by Cu-based electrocatalysts. Unlike Cu, which binds CO too weakly and favors the production of C1 and C2 products, transition metals like Co and Ni, particularly if designed to contain M/M-oxide

interfaces, enable C-C coupling and chain propagation by stabilizing key intermediates. Thus, the structural design of the catalysts could change depending on the selective production of the desired products.

One of the most effective structural modification strategies in catalyst design is atomic level dispersion of metal centers, which enhances catalytic performance by increasing the uniformity and structural complexity of the active site [47]. The size and spatial distribution of the active catalytic sites play a critical role in dictating product selectivity. Notably, most single-atom catalysts (SACs) investigated for CO2RR predominantly produce CO with exceptional efficiency, often rivaling their pristine metal counterparts [1, 48]. The fundamental reason for this behavior lies in the separation of catalytic sites by organic linkers, which effectively suppresses CC coupling and limits the formation of C_{2+} products [49]. Research has demonstrated that facilitating CC coupling, which proceeds via COCO intermediate interactions, enhances C_{2+} selectivity. This effect can be achieved through well-defined surface binding motifs, a CO-rich local environment, and cooperative interactions across multiple active sites [50].

The question that naturally arises, then, is: what product should be targeted? Given that CO_2RR technology is not yet mature or industrialized, it is difficult to directly align research efforts with industrial demands. Instead, research should focus on defining key parameters and evaluating which products hold the most promise for future applications. For instance, one study concluded that formate/formic acid and carbon monoxide have the highest normalized market price among all CO_2RR products [51], suggesting that these may be the most economically viable targets for further development. Considering this, in this dissertation, we prioritize materials that inherently favor the production of lighter carbon products while suppressing CC coupling. Metal-organic frameworks (MOFs) emerge as promising candidates not only because their porous structure provides a high surface area, customizable pore structures, and facile and controllable synthesis, but also because their well-defined single-atom catalytic sites and tunable structures enable selective CO_2 reduction. Moreover, their tunable structure allows precise control over the coordination environment and electronic properties, providing a unique platform for optimizing catalytic performance in CO_2RR [52, 53].

1.4. METAL-ORGANIC FRAMEWORK- BASED ELECTROCATALYSTS

MOFs are a subclass of coordination polymers (CPs) characterized by their crystalline, porous structures and strong metal-ligand interactions. These materials consist of metal nods bonded to organic linkers, forming highly ordered frameworks with tunable pore sizes, shapes, and chemical environments. Metalligand coordinative bonds are stronger than hydrogen bonds, and they have more spatial control than some other interactions, such as $\pi\pi$ stacking. Their exceptional surface area and structural flexibility enable applications in gas storage, separation, sensing and catalysis, making them a versatile platform for advanced material design. The growing interest in MOFs stems from the simultaneity of three key characteristics: crystallinity,

porosity, and strong metal-ligand interactions. This distinctive combination of properties makes MOFs a unique and highly valuable class of materials [54].

In the context of aqueous electrocatalytic CO_2RR, MOFs combine the favourable characteristics of both heterogeneous and homogeneous catalysts. Due to their porosity, MOFs provide a large surface area, manifesting their suitability for any catalytic applications. The crystalline structured-nature of MOFs enables precise control of the active catalytic centre at the atomic scale [55]. In addition, a variety of metals and organic molecules can be incorporated together to form a MOF, resulting in over 20,000 reported MOFs to date from the first ever reported by Yaghi et al. [56, 57]. It is commonly accepted that the redox-active metal sites within MOFs, such as Fe, Co, Ni, Cu, or Mn, are the active sites capable of delivering catalytic activity [58]. The design and optimization of MOFs for electrocatalytic CO_2RR are typically guided by mechanistic studies of high-energy intermediates and the reaction pathway as well as computational analyses of MOF activity, composition, and structure using tools such as DFT, which provide significant opportunities for advancing catalyst design in CO_2RR [59]. Nevertheless, despite possessing many structural benefits, the limited charge transport characteristics of chemically stable MOFs frequently hinder their utilization as direct electrocatalysts.

MOFs tend to produce lighter products like CO and formic acid because their complex structure and single-atom dispersion hinder C-C coupling in most cases, limiting the formation of heavier C_{2+} products [60]. However, despite their advantages in improving the selectivity, the use of MOFs in electrocatalyst applications has been hindered by poor conductivity; therefore, low activity [61]. This issue arises mainly from the presence of carboxylate linkers in the multidimensional frameworks. The high electronegativity of the oxygen atoms in these carboxylates increases the potential barrier for electron transfer through the organic linkers [62]. As a result, the overlap between oxygen atoms and metal d-orbitals is reduced, causing the low conductivity typically seen in most MOFs [63]. Therefore, design strategies that not only help with breaking LSR to improve selectivity but also helps overcoming electronic limitations is essential to unlocking the full potential of MOFs as efficient electrocatalysts. This statement provides the most general explanation of the objective of this dissertation: how MOFs can be designed to selectively convert CO_2 into one product while showing enhanced catalytic performance.

1.5. THESIS OUTLINE

This dissertation systematically explores how the atomicscale design and postsynthetic modification of MOFs can overcome long-standing challenges related to selectivity and conductivity in electrochemical CO_2RR. The current chapter, chapter 1, introduces the social and technical challenges and outlines the thesis objectives. This continues with Chapter 2, including a comprehensive review of the current landscape of pristine MOFs and MOF composites used in CO_2RR, outlining the major obstacles that limit their performancenamely, insufficient catalytic activity, poor product selectivity, and low intrinsic conductivity. This chapter establishes a foundation for understanding how MOF structureproperty relationships govern electrocatalytic performance.

Building on these insights, Chapter 3 presents a set of rational design strategies aimed at breaking the conventional linear scaling relations that typically constrain selectivity in transition metal-based catalysts. Specifically, it highlights how variations in metal centers, organic linkers, and coordination environments can be used to independently modulate binding energies of key intermediates. This structural tunability is presented as a key advantage of MOFs for engineering catalytic sites tailored toward specific CO_2RR pathways.

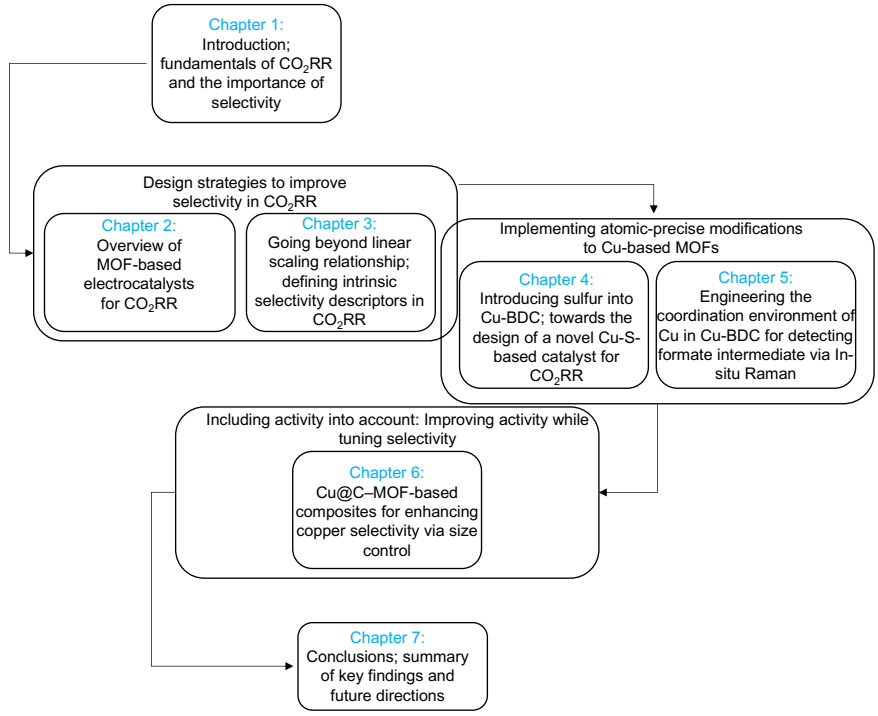

Figure 1.4: Schematic of the thesis outline

Chapters 4 and 5 apply these principles experimentally using copperbenzenedicarboxylate (Cu-BDC) MOFs as a model platform. Chapter 4 describes the synthesis and characterization of a novel planar [CuS]organic framework, in which the introduction of sulfur into the coordination sphere facilitates selective conversion of CO_2 to formate. The reaction mechanism is investigated through electrochemical analysis and DFT simulations, which together reveal that sulfur coordination tunes the adsorption energetics to favor the *OCHO intermediate.

Chapter 5 continues this theme by demonstrating that modulating the copper coordination numberfrom fivefold to fourfoldwithin the same MOF structure can dramatically alter the product distribution. Using a combination of 3D electron diffraction, X-ray photoelectron spectroscopy (XPS), operando Raman spectroscopy, and DFT, this study establishes that the removal of a single axial ligand destabilizes

*COOH relative to *OCHO, resulting in a shift in selectivity from CO to formate. This chapter underscores the power of coordination number control as a design lever in MOF-based catalysis.

In Chapter 6, the focus shifts toward improving conductivity through structural transformation. Two-dimensional MOFs are subjected to carbonization under varying conditions to produce Cu-doped nanoporous carbons. The chapter investigates how temperature, atmosphere, and structural integrity influence the resulting materials conductivity, morphology, and residual heteroatom content. These parameters are then correlated with CO_2RR activity and selectivity, offering insights into how carbonization can convert insulating MOFs into efficient, conductive electrocatalysts.

Chapter 7 concludes the dissertation by synthesizing the findings across all chapters into a unified framework. It emphasizes how precise control over coordination environments and targeted postsynthetic modifications can be synergistically combined to address the dual challenge of selectivity and conductivity in MOF-based CO_2RR. Finally, the chapter outlines future directions for advancing these materials toward industrial scalability, including hybrid composite strategies and in situ characterization approaches for mechanistic insight.

1.5.1. RESEARCH QUESTIONS

To guide these studies, this thesis addresses the following key questions:

1. (RQ1) What design principles enable MOFs to disrupt linear scaling relationships and favor the formation of a single CO_2RR product? (Chapters 2-3)

2. (RQ2) How can the modular tunability of MOFs , specifically through variations in ligand identity, coordination number, and framework topology, be leveraged to enhance the stabilization of the *OCHO intermediate and promote selective formate production? (Chapter 4-5)

3. (RQ3) Which spectroscopic features can serve as reliable operando fingerprints for identifying the presence of *OCHO intermediates on Cu-based MOFs, and how can these be used to track selectivity in real time? (Chapter 5)

4. (RQ4) How do carbonization of 2D MOFs into Cu-doped porous carbons influence CO_2RR activity and selectivity? (Chapter 6)

BIBLIOGRAPHY

[1] M. Li, H. Wang, W. Luo, P. C. Sherrell, J. Chen, and J. Yang. "Heterogeneous single-atom catalysts for electrochemical CO_2 reduction reaction". In: *Advanced Materials* 32.34 (2020), p. 2001848.

[2] Q. Wang, C. Cai, M. Dai, J. Fu, X. Zhang, H. Li, H. Zhang, K. Chen, Y. Lin, H. Li, *et al.* "Recent advances in strategies for improving the performance of CO_2 reduction reaction on single atom catalysts". In: *Small Science* 1.2 (2021), p. 2000028.

[3] B. Zhang, Y. Jiang, M. Gao, T. Ma, W. Sun, and H. Pan. "Recent progress on hybrid electrocatalysts for efficient electrochemical CO_2 reduction". In: *Nano Energy* 80 (2021), p. 105504.

[4] T. N. Nguyen, M. Salehi, Q. V. Le, A. Seifitokaldani, and C. T. Dinh. "Fundamentals of electrochemical CO_2 reduction on single-metal-atom catalysts". In: *ACS Catalysis* 10.17 (2020), pp. 10068–10095.

[5] A. Bagger, W. Ju, A. S. Varela, P. Strasser, and J. Rossmeisl. "Electrochemical CO_2 reduction: a classification problem". In: *ChemPhysChem* 18.22 (2017), pp. 3266–3273.

[6] P. Yaashikaa, P. S. Kumar, S. J. Varjani, and A. Saravanan. "A review on photochemical, biochemical and electrochemical transformation of CO_2 into value-added products". In: *Journal of CO_2 Utilization* 33 (2019), pp. 131–147.

[7] R.-P. Ye, J. Ding, W. Gong, M. D. Argyle, Q. Zhong, Y. Wang, C. K. Russell, Z. Xu, A. G. Russell, Q. Li, *et al.* "CO_2 hydrogenation to high-value products via heterogeneous catalysis". In: *Nature communications* 10.1 (2019), p. 5698.

[8] W. Zhang, Z. Chen, Y.-X. Jiang, L.-L. Liao, W. Wang, J.-H. Ye, and D.-G. Yu. "Arylcarboxylation of unactivated alkenes with CO_2 via visible-light photoredox catalysis". In: *Nature Communications* 14.1 (2023), p. 3529.

[9] A. D. Kamkeng, M. Wang, J. Hu, W. Du, and F. Qian. "Transformation technologies for CO_2 utilisation: Current status, challenges and future prospects". In: *Chemical Engineering Journal* 409 (2021), p. 128138.

[10] K. Li, B. Peng, and T. Peng. "Recent advances in heterogeneous photocatalytic CO_2 conversion to solar fuels". In: *Acs Catalysis* 6.11 (2016), pp. 7485–7527.

[11] M. Ong, S. Nomanbhay, F. Kusumo, and P. Show. "Application of microwave plasma technology to convert carbon dioxide (CO_2) into high value products: A review". In: *Journal of Cleaner Production* 336 (2022), p. 130447.

[12] D. R. Kauffman, J. Thakkar, R. Siva, C. Matranga, P. R. Ohodnicki, C. Zeng, and R. Jin. "Efficient electrochemical CO_2 conversion powered by renewable energy". In: *ACS applied materials & interfaces* 7.28 (2015), pp. 15626–15632.

[13] W. Wang, S. Wang, X. Ma, and J. Gong. "Recent advances in catalytic hydrogenation of carbon dioxide". In: *Chemical Society Reviews* 40.7 (2011), pp. 3703–3727.

[14] S. C. Roy, O. K. Varghese, M. Paulose, and C. A. Grimes. "Toward solar fuels: photocatalytic conversion of carbon dioxide to hydrocarbons". In: *ACS nano* 4.3 (2010), pp. 1259–1278.

[15] Y. Zhou, K. Wang, S. Zheng, X. Cheng, Y. He, W. Qin, X. Zhang, H. Chang, N. Zhong, and X. He. "Advancements in electrochemical CO_2 reduction reaction: A review on CO_2 mass transport enhancement strategies". In: *Chemical Engineering Journal* (2024), p. 150169.

[16] M. G. Kibria, J. P. Edwards, C. M. Gabardo, C.-T. Dinh, A. Seifitokaldani, D. Sinton, and E. H. Sargent. "Electrochemical CO_2 reduction into chemical feedstocks: from mechanistic electrocatalysis models to system design". In: *Advanced Materials* 31.31 (2019), p. 1807166.

[17] T. Zheng, K. Jiang, and H. Wang. "Recent advances in electrochemical CO_2-to-CO conversion on heterogeneous catalysts". In: *Advanced materials* 30.48 (2018), p. 1802066.

[18] Y. Zou and S. Wang. "An investigation of active sites for electrochemical CO_2 reduction reactions: from in situ characterization to rational design". In: *Advanced Science* 8.9 (2021), p. 2003579.

[19] B. Kumar, J. P. Brian, V. Atla, S. Kumari, K. A. Bertram, R. T. White, and J. M. Spurgeon. "New trends in the development of heterogeneous catalysts for electrochemical CO_2 reduction". In: *Catalysis Today* 270 (2016), pp. 19–30.

[20] C. Long, X. Li, J. Guo, Y. Shi, S. Liu, and Z. Tang. "Electrochemical reduction of CO_2 over heterogeneous catalysts in aqueous solution: recent progress and perspectives". In: *Small Methods* 3.3 (2019), p. 1800369.

[21] S. Hernández, M. A. Farkhondehfal, F. Sastre, M. Makkee, G. Saracco, and N. Russo. "Syngas production from electrochemical reduction of CO 2: current status and prospective implementation". In: *Green Chemistry* 19.10 (2017), pp. 2326–2346.

[22] S. Zhang, Q. Fan, R. Xia, and T. J. Meyer. "CO_2 reduction: from homogeneous to heterogeneous electrocatalysis". In: *Accounts of chemical research* 53.1 (2020), pp. 255–264.

[23] M. Sajna, S. Zavahir, A. Popelka, P. Kasak, A. Al-Sharshani, U. Onwusogh, M. Wang, H. Park, and D. S. Han. "Electrochemical system design for CO_2 conversion: A comprehensive review". In: *Journal of Environmental Chemical Engineering* (2023), p. 110467.

[24] S. Xu and E. A. Carter. "Theoretical insights into heterogeneous (photo) electrochemical CO_2 reduction". In: *Chemical reviews* 119.11 (2018), pp. 6631–6669.

[25] R. Kortlever, J. Shen, K. J. P. Schouten, F. Calle-Vallejo, and M. T. Koper. "Catalysts and reaction pathways for the electrochemical reduction of carbon dioxide". In: *The journal of physical chemistry letters* 6.20 (2015), pp. 4073–4082.

[26] Z. Gu, H. Shen, L. Shang, X. Lv, L. Qian, and G. Zheng. "Nanostructured copper-based electrocatalysts for CO_2 reduction". In: *Small Methods* 2.11 (2018), p. 1800121.

[27] S. Jin, Z. Hao, K. Zhang, Z. Yan, and J. Chen. "Advances and challenges for the electrochemical reduction of CO_2 to CO: from fundamentals to industrialization". In: *Angewandte Chemie* 133.38 (2021), pp. 20795–20816.

[28] Z. Kou, X. Li, T. Wang, Y. Ma, W. Zang, G. Nie, and J. Wang. "Fundamentals, on-going advances and challenges of electrochemical carbon dioxide reduction". In: *Electrochemical Energy Reviews* 5.1 (2022), pp. 82–111.

[29] W. Zhang, Y. Hu, L. Ma, G. Zhu, Y. Wang, X. Xue, R. Chen, S. Yang, and Z. Jin. "Progress and perspective of electrocatalytic CO_2 reduction for renewable carbonaceous fuels and chemicals". In: *Advanced Science* 5.1 (2018), p. 1700275.

[30] J. T. Richardson. *Principles of catalyst development*. Springer, 2013.

[31] D. Voiry, H. S. Shin, K. P. Loh, and M. Chhowalla. "Low-dimensional catalysts for hydrogen evolution and CO_2 reduction". In: *Nature Reviews Chemistry* 2.1 (2018), p. 0105.

[32] F. Franco, C. Rettenmaier, H. S. Jeon, and B. R. Cuenya. "Transition metal-based catalysts for the electrochemical CO 2 reduction: from atoms and molecules to nanostructured materials". In: *Chemical Society Reviews* 49.19 (2020), pp. 6884–6946.

[33] Y. Hori, H. Wakebe, T. Tsukamoto, and O. Koga. "Electrocatalytic process of CO selectivity in electrochemical reduction of CO_2 at metal electrodes in aqueous media". In: *Electrochimica Acta* 39.11-12 (1994), pp. 1833–1839.

[34] G. Liu, T. Tran-Phu, H. Chen, and A. Tricoli. "A review of metal-and metal-oxide-based heterogeneous catalysts for electroreduction of carbon dioxide". In: *Advanced Sustainable Systems* 2.8-9 (2018), p. 1800028.

[35] E. Tayyebi, J. Hussain, Y. Abghoui, and E. Skúlason. "Trends of electrochemical CO_2 reduction reaction on transition metal oxide catalysts". In: *The Journal of Physical Chemistry C* 122.18 (2018), pp. 10078–10087.

[36] Z. Cai, Y. Wu, Z. Wu, L. Yin, Z. Weng, Y. Zhong, W. Xu, X. Sun, and H. Wang. "Unlocking bifunctional electrocatalytic activity for CO_2 reduction reaction by win-win metal–oxide cooperation". In: *ACS Energy Letters* 3.11 (2018), pp. 2816–2822.

[37] Y. Y. Birdja, E. Pérez-Gallent, M. C. Figueiredo, A. J. Göttle, F. Calle-Vallejo, and M. T. Koper. "Advances and challenges in understanding the electrocatalytic conversion of carbon dioxide to fuels". In: *Nature Energy* 4.9 (2019), pp. 732–745.

[38] O. Bushuyev, P. De Luna, C. Dinh, L. Tao, G. Saur, J. Van De Lagemaat, S. Kelley, and E. Sargent. *What should we make with CO_2 and how can we make it? Joule 2: 825–832*. 2018.

[39] J. B. Greenblatt, D. J. Miller, J. W. Ager, F. A. Houle, and I. D. Sharp. "The technical and energetic challenges of separating (photo) electrochemical carbon dioxide reduction products". In: *Joule* 2.3 (2018), pp. 381–420.

[40] J. Pérez-Ramírez and N. López. "Strategies to break linear scaling relationships". In: *Nature Catalysis* 2.11 (2019), pp. 971–976.

[41] F. Abild-Pedersen, J. Greeley, F. Studt, J. Rossmeisl, T. R. Munter, P. G. Moses, E. Skulason, T. Bligaard, and J. K. Nørskov. "Scaling Properties of Adsorption Energies for Hydrogen-Containing Molecules<? format?> on Transition-Metal Surfaces". In: *Physical review letters* 99.1 (2007), p. 016105.

[42] T. Z. Gani and H. J. Kulik. "Understanding and Breaking Scaling Relations in Single-Site Catalysis: Methane to Methanol Conversion by Fe^{IV} = O". In: *Acs Catalysis* 8.2 (2018), pp. 975–986.

[43] D.-H. Nam, O. Shekhah, G. Lee, A. Mallick, H. Jiang, F. Li, B. Chen, J. Wicks, M. Eddaoudi, and E. H. Sargent. "Intermediate binding control using metal–organic frameworks enhances electrochemical CO_2 reduction". In: *Journal of the American Chemical Society* 142.51 (2020), pp. 21513–21521.

[44] P. Saha, S. Amanullah, and A. Dey. "Selectivity in electrochemical CO_2 reduction". In: *Accounts of chemical research* 55.2 (2022), pp. 134–144.

[45] P. Preikschas, J. Zhang, R. R. Seemakurthi, Z. Lian, A. J. Martín, S. Xi, F. Krumeich, H. Ma, Y. Zhou, N. López, *et al.* "CO_2 Electroreduction to Long-Chain Hydrocarbons on Cobalt Catalysts". In: *Advanced Energy Materials* 14.47 (2024), p. 2401447.

[46] Y. Zhou, A. J. Martín, F. Dattila, S. Xi, N. López, J. Pérez-Ramírez, and B. S. Yeo. "Long-chain hydrocarbons by CO_2 electroreduction using polarized nickel catalysts". In: *Nature Catalysis* 5.6 (2022), pp. 545–554.

[47] X.-F. Yang, A. Wang, B. Qiao, J. Li, J. Liu, and T. Zhang. "Single-atom catalysts: a new frontier in heterogeneous catalysis". In: *Accounts of chemical research* 46.8 (2013), pp. 1740–1748.

[48] J. Shan, C. Ye, Y. Jiang, M. Jaroniec, Y. Zheng, and S.-Z. Qiao. "Metal-metal interactions in correlated single-atom catalysts". In: *Science Advances* 8.17 (2022), eabo0762.

[49] Z. Zhang, Z. Yang, L. Liu, Y. Wang, and S. Kawi. "Catalytic CO_2 Conversion to C1 Chemicals over Single-Atom Catalysts". In: *Advanced Energy Materials* 13.42 (2023), p. 2301852.

[50] A. Xu, S.-F. Hung, A. Cao, Z. Wang, N. Karmodak, J. E. Huang, Y. Yan, A. Sedighian Rasouli, A. Ozden, F.-Y. Wu, *et al.* "Copper/alkaline earth metal oxide interfaces for electrochemical CO_2-to-alcohol conversion by selective hydrogenation". In: *Nature Catalysis* 5.12 (2022), pp. 1081–1088.

[51] M. Jouny, W. Luc, and F. Jiao. "General techno-economic analysis of CO_2 electrolysis systems". In: *Industrial & Engineering Chemistry Research* 57.6 (2018), pp. 2165–2177.

[52] Z. Liang, C. Qu, W. Guo, R. Zou, and Q. Xu. "Pristine metal–organic frameworks and their composites for energy storage and conversion". In: *Advanced Materials* 30.37 (2018), p. 1702891.

[53] H. Furukawa, K. E. Cordova, M. OKeeffe, and O. M. Yaghi. "The chemistry and applications of metal-organic frameworks". In: *Science* 341.6149 (2013), p. 1230444.

[54] A. Corma, H. Garcia, and F. Llabrés i Xamena. "Engineering metal organic frameworks for heterogeneous catalysis". In: *Chemical reviews* 110.8 (2010), pp. 4606–4655.

[55] Y. Zhang, X. Zhang, Y. Zhu, B. Qian, A. M. Bond, and J. Zhang. "The Origin of the Electrocatalytic Activity for CO_2 Reduction Associated with Metal-Organic Frameworks". In: *ChemSusChem* 13.10 (2020), pp. 2552–2556.

[56] O. M. Yaghi, G. Li, and H. Li. "Selective binding and removal of guests in a microporous metal–organic framework". In: *Nature* 378.6558 (1995), pp. 703–706.

[57] H. Li, M. Eddaoudi, M. O'Keeffe, and O. M. Yaghi. "Design and synthesis of an exceptionally stable and highly porous metal-organic framework". In: *nature* 402.6759 (1999), pp. 276–279.

[58] H. Zhang, J. Li, Q. Tan, L. Lu, Z. Wang, and G. Wu. "Metal–organic frameworks and their derived materials as electrocatalysts and photocatalysts for CO_2 reduction: Progress, challenges, and perspectives". In: *Chemistry–A European Journal* 24.69 (2018), pp. 18137–18157.

[59] H. B. Aiyappa, J. Masa, C. Andronescu, M. Muhler, R. A. Fischer, and W. Schuhmann. "MOFs for electrocatalysis: from serendipity to design strategies". In: *Small Methods* 3.8 (2019), p. 1800415.

[60] N. Kornienko, Y. Zhao, C. S. Kley, C. Zhu, D. Kim, S. Lin, C. J. Chang, O. M. Yaghi, and P. Yang. "Metal–organic frameworks for electrocatalytic reduction of carbon dioxide". In: *Journal of the American Chemical Society* 137.44 (2015), pp. 14129–14135.

[61] C. A. Downes and S. C. Marinescu. "Electrocatalytic metal–organic frameworks for energy applications". In: *ChemSusChem* 10.22 (2017), pp. 4374–4392.

[62] L. Sun, M. G. Campbell, and M. Dinc. "Electrically conductive porous metal–organic frameworks". In: *Angewandte Chemie International Edition* 55.11 (2016), pp. 3566–3579.

[63] L. S. Xie, G. Skorupskii, and M. Dinc. "Electrically conductive metal–organic frameworks". In: *Chemical reviews* 120.16 (2020), pp. 8536–8580.

2

MOF-BASED ELECTROCATALYSTS FOR CO_2 REDUCTION REACTION

Abstract

The increasing concentration of CO_2 is a serious concern for society. Electrochemical conversion of CO_2 into valuable products, including fuels, offers a viable solution and helps close the carbon-neutral cycle. Metal-organic frameworks (MOFs) composites, due to their high porosity, large surface area, and significant chemical tunability, are considered to be a promising class of catalyst materials for the CO_2 reduction reaction (CO_2RR). This book chapter focuses on the fundamentals of CO_2RR and mechanism of the reaction followed by discussing the recent advancements in MOF composite electrocatalysts for CO_2RR including MOF-supported electrocatalysts, conductive supported MOF composites, graphene and carbonous MOF composites, MOF-MXenes, MOF-polymers and polyoxometalate.

Modified portions of this chapter have been published in the following book chapter:
K. Roohi, J. Coppen, A. Mol, P. Taheri, Metal-Organic Framework Composites as Electrocatalyst for Carbon Dioxide Conversion. Applications of Metal-Organic Framework Composites. *Elsevier*, 2025. 539-565.

2.1. Introduction

MOFs, as defined above, are a class of crystalline porous materials formed by linking metal-containing units, often called secondary building units (SBUs), with polydentate organic ligands through strong coordination bonds. This process, known as reticular synthesis, results in extended one-, two-, or three-dimensional networks with permanent porosity. The modular construction of MOFs provides a high degree of design flexibility, allowing systematic variation of both the metal nodes and organic linkers to achieve a vast library of structures with diverse properties. This particular aspect of MOFs is what makes them the focus of this dissertation. MOFs typically consist of transition metals such as Cu, Zn, Zr, or Fe coordinated with organic ligands like carboxylates, azolates, or phosphonates. The strength and geometric directionality of these metalligand bonds causes robustness and crystallinity to the frameworks. A major breakthrough in MOF chemistry came with the realization that using rigid geometries such as squares or octahedra in SBUs leads to predictable topologies and enhanced porosity. The first proof of permanent porosity in MOFs was established through low-pressure nitrogen and CO_2 sorption measurements, notably with zinc terephthalate-based MOFs and later MOF-5, which became a benchmark for porosity and structural robustness.

This combination of structural tunability and exceptional surface area which often exceeds 5000 m^2/g, makes MOFs ideal for applications in gas storage, separation, and catalysis. Innovations such as postsynthetic modification (PSM) and the development of multivariate MOFs (MTV-MOFs), where multiple functionalities are incorporated within a single framework, and MOF composites, have further broadened the scope of MOF chemistry. These advancements enable precise control over pore environments and allow for heterogeneity in functionally active sites.

Postsynthetic modification (PSM) has become a powerful strategy in MOF chemistry, enabling the tuning of chemical reactivity within the framework without disrupting its overall crystallinity. This is particularly valuable for catalytic applications, where active sites can be introduced or fine-tuned post-synthesis to achieve desired functionalities. Furthermore, multivariate MOFs (MTV-MOFs) incorporate multiple types of linkers or functionalities within a single framework, allowing for precise spatial and electronic tuning of the pore environment. Additionally, in a broader aspect, mostly in the field of electrocatalysis although an important research focuses on novel synthesis and modification methods, a new research trend investigates the combination of MOFs with a variety of nano- and micro-particles known as MOF composites [1]. MOF composites are combination of functional materials such as carbon substrates, nanoparticles, polymers, enzymes with MOF which have further improved physico -chemical properties like mechanical stability, conductivity and catalytic performance.

These strategies, combined with the inherent modularity of MOFs, allow for the rational design of frameworks tailored to specific applications, such as selective catalysis or charge transport. The ability of MOFs to maintain their crystallinity and structure upon functionalization distinguishes them from other porous materials. Their tunable chemical environment, combined with the availability of robust synthetic strategies, positions MOFs as a unique class of materials for both fundamental research and practical applications in catalysis, energy storage, and

environmental remediation. In this chapter, we review the MOF-based electrocatalysts for CO_2RR together with recent advances on catalytic design and performance improvement. The current state-of-the-art MOF and MOF composites including metal and metal oxide nanoparticle @ MOFs, metal/metal oxide @ pyrolysed MOF, MOF @ conductive substrates, MOF @ carbon substrates, MOF @ MOF, MOF @ polymers and polyoxometalates and MOF- MXene composites are discussed and their potential performance in CO_2RR are summarized.

2.2. PRISTINE MOFS AS ELECTROCATALYSTS

In the context of CO_2 reduction reactions, MOFs- where metal centers often function as isolated catalytic sites- offer the unique advantage of breaking LSR and improving reaction selectivity [2]. It is well known that downsizing metal nanostructures into atomically distributed centers, known as single atom catalysis (SAC), is an effective approach for metal catalysts [3]. The size and spatial distribution of catalytic active sites play a critical role in dictating product selectivity. Notably, most SACs investigated for CO2RR predominantly produce CO with exceptional efficiency, often rivaling their pristine metal counterparts [3, 4]. Primarily, the fundamental reason for this behavior lies in the separation of catalytic sites by organic linkers, which effectively suppresses CC coupling and limits the formation of C2+ products [5]. Research has demonstrated that facilitating CC coupling, which proceeds via CO-CO intermediate interactions, enhances C_{2+} selectivity. This effect can be achieved through well-defined surface binding motifs, a CO-rich local environment, and cooperative interactions across multiple active sites [6]. Therefore, MOFs, with their structurally intricate frameworks and atomically dispersed metal centers, inherently hinder the formation of C_{2+} species while favoring the selective production of lighter products such as CO and HCOOH. This controlled single-site environment underscores the potential of MOFs as tunable electrocatalysts for achieving high selectivity in CO_2 reduction. It is worth mentioning that according to a study by Jouny et al. formic acid and carbon monoxide have the highest normalized market price among all the other CO_2RR products [7]. Table 2.1 lists the state-of-the-art MOF electrocatalysts for CO_2RR, showing that in the majority of cases, the reduction reaction terminates at CO. Other factors, such as the stability of MOFs and the coordination environment, also influence product distribution and will be further in the next chapters.

Table 2.1: Recent state-of-the-art MOF electrocatalysts for CO_2RR

Material	Electrolyte	Potential (V vs. RHE)	PCD (mA/cm^2)	FE %	Product(s)	ref.
Cu-THQ	1 M KOH-1 M choline chloride	-0.45	157.4	91	CO	[8]
Cu(L)SO_4.2H_2O	0.1 M $KHCO_3$	-0.89	3	77.5	CO	[9]
Ni(NC)	1 M KOH	-0.75	-	99	CO	[10]
Cu-DBC	0.1 M $KHCO_3$	-1.4	6.38	56	CH_4	[11]
ZIF-8	0.25 M K_2SO_4	-1.1	6.9	81	CO	[12]
Cu-TTCOF	1 M KOH	-0.9	≈40	43.6	CH_4	[13]
Cu_3(HHTQ)$_2$	0.1 M $KHCO_3$	-0.4	-	53.6	CH_3OH	[14]
Bi-BTC	0.5 M $KHCO_3$	-0.86	11.2	95	HCOOH	[15]
Cu(II) phthalocyanine	0.5 M $KHCO_3$	-1.06	13	66	H_2	[16]

However, despite the advantages of MOFs in improving the selectivity of CO_2RR,

their use as electrocatalyst has been hindered by poor conductivity, therefore, low activity [17]. This issue arises mainly from the presence of carboxylate linkers in the multidimensional frameworks. The high electronegativity of the oxygen atoms in these carboxylates increases the potential barrier for electron transfer through the organic linkers [18]. This limitation together with their low stability in most of the electrolytes lead to poduction of different MOF composite in order to tune the conductivity and in general electrochemical activity. In the next chapters, we will discuss different methods that can be used to improve the chemical structure of MOFs to enhance their electrocatalytic performance for CO_2RR. However, the focus of this chapter is to present different strategies for compositing MOFs with other active materials to improve their performance for CO_2RR.

2.3. MOFs as Supports

This group of MOF composites has been extensively researched for CO_2RR, involving materials where the MOF serves as a porous support, with active catalytic sites such as metal and metal oxide nanoparticles (NPs) are deposited on [19]. The incorporation of MOFs, improves the electrocatalytic performance of NPS due to their porous structures and large specific surface area. Cu_2O particles, known for their tunable crystal facets and relatively stable bulk-phase structure, are considered promising candidates for studying the mechanism of CO_2 reduction. However, significant hydrogen production during the electrocatalytic process often results in a reduced FE for hydrocarbons. To improve the overall hydrocarbon FE, it is crucial to enhance the CO_2 adsorption capacity of Cu_2O. Cu_2O@Cu-MOF catalyst, When employed as an electrocatalyst for the electrochemical reduction of CO_2, demonstrates exceptional performance, with a total FE for hydrocarbons (CH_4 and C_2H_4) reaching 79.4 %, notably featuring a FE of 63.2 % for CH_4 [20]. The multifunctionality of the synthesized Cu_2O@Cu-MOF, encompassing adsorption, activation, and catalysis, stems from the synergistic interaction between Cu-MOF and Cu_2O.

In addition, metallic nanoparticles are recognized as suitable catalysts for CO_2 reduction reactions; however, their tendency to agglomerate diminishes their catalytic efficiency [21]. MOFs, with their high surface area and notable porosity, can prevent this agglomeration and enhance the catalytic performance of nanoparticles encapsulated within them. Silver is one of the most extensively studied metals for electrochemical CO_2 reduction, producing CO as the main product due to weak CO adsorption on its surface [22]. Both CO_2 electroreduction to CO and the competing HER take place concurrently on Ag NPs. In this regard, Jiang et al. [23] investigated the Ag/ZIF-7 MOF composite as a CO_2 electroreduction catalyst and higher CO faradaic efficiency and current density was observed (80.5% and 26.2 mA cm^{-2} at −1.2 V) compared to its prinstine components. This improved performance is attributed to the large accessible surface area and the synergistic interaction between Ag nanoparticles and ZIF-7 MOF.

As another example of MOF supports, in a study by Yi, JunDong, et al. [24] uniform Cu_2O(111) NPs were fabricated on a conductive CuHHTP framework via electrochemical treatment, resulting in conversion of some Cu^{2+} centers within MOF

into 3.5 nm Cu_2O NPs with exposed (111) crystal planes. The Cu_2O@CuHHTP composite demonstrated high conductivity and excellent performance in CO_2 electroreduction to CH_4, achieving 73% Faradaic efficiency and 10.8 mA/cm^2 partial current density. The small size of the NPs, exposed crystal planes, and released hydroxyl groups (OH-) from the HHTP ligand contributed to the high CH_4 selectivity, while the CuHHTP support enhanced electron transfer for better current density. Furthermore, in a more recent study zirconium-based PCN-222 MOFs with metalloporphyrin Cu centers and incorporated gold nanoneedles were successfully synthesized using ligand carboxylates as reducing agents. Compared to similar MOF components, AuNN@PCN-222(Cu) exhibited a significantly enhanced ethylene production with a Faradaic efficiency of 52.5% [25] (Fig. 2.1). Some of the other Metal/Metal oxide-MOF composites and their CO_2RR performance, are listed in Table 2.2.

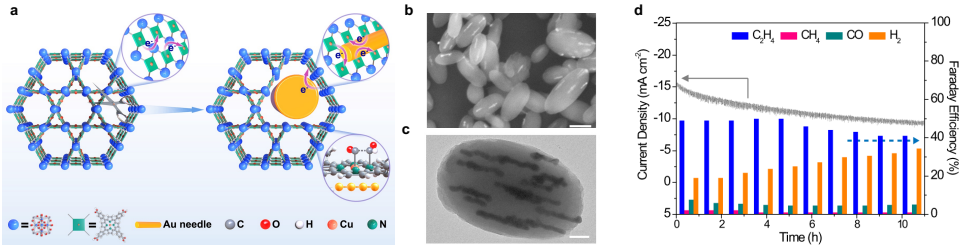

Figure 2.1: a, Incorporation of Au nanoneedles into PCN-222(Cu) to alter the charge transfer and pathway of CO_2RR. **b**, SEM image of the composit, scale bar, 250 nm, **c** TEM image of the composit, scale bar, 50 nm. **d** Chronoamperometric stability tests for AuNN@PCN-222(Cu) at -1.2 V vs RHE [25].

Metal-metal oxide MOF composites could be synthesized with various methods such as liquid impregnation. In this method, desolvated MOFs are soaked in metal precursor solutions and then reduced to form MNPs within the pores. Incipient wetness impregnation involves using a solution with a volume equal to the MOF's pore volume for precise control over metal loading. Gas-phase infiltration (MOCVD) is another method, in which, exposes desolvated MOFs to volatile metal precursors under vacuum, followed by reduction or decomposition to produce MNPs. The double solvent method (DSM) employs both hydrophilic and hydrophobic solvents to minimize MNP aggregation on the MOF surface. Redox-active MOFs use the inherent redox properties of MOF to reduce metal ions into nanoparticles without additional reducing agents. Photochemical reduction leverages light to facilitate MNP formation within MOFs, while colloidal deposition and urea precipitation methods, though effective, often result in surface aggregation of NPs [26]. One method of preparing metal based MOF-derived composites is pyrolysis or carbonization of the pristine MOF.

Carbonization is a process frequently used to produce carbon rods and other carbon

Table 2.2: List of studied Metal/Metal oxide-MOF composites and their performance for CO_2RR. With permission from [21, 27, 28]

MOF composite	Electrolyte	Potential	Product(s)	FE (%)	Ref.
Ag/Co-MOF	0.1M $KHCO_3$	-1.8 V vs. SCE	CO	55.6	[29]
CuO/Cu-MOF	0.1 M $KHCO_3$	-1.1 V	C_2H_4	50	[30]
Ag@Al-PMOF	0.1 M $KHCO_3$	-1.1 V	CO	55.8± 2.8	[31]
Cu_2O/Cu-MOF	0.1 M $KHCO_3$	-1.71 V vs. RHE	CH_4	63.2	[20]
Cu_2O/Cu-MOF	0.1 M $KHCO_3$	-1.71 V vs. RHE	CH_4	63.2	[20]
Bi_2O_3/2D- Zr-TATB-MOF	0.5 M $KHCO_3$	-0.97 V vs. RHE	HCOOH	≈85	[32]
SnO_2/2D- Zr-TATB-MOF	0.5 M $KHCO_3$	-0.97 V vs. RHE	HCOOH	≈35	[32]
In_2O_3/2D- Zr-TATB-MOF	0.5 M $KHCO_3$	-0.97 V vs. RHE	HCOOH	≈45	[32]

nano-sized materials. In this process, by increasing the temperature, bonds between carbon and other elements (i.e O, N, S, TMs) in the organic building unit within MOF structure, break. These elements leave the material, allowing carbon atoms to bond with each other, resulting in a framework composed of pure carbon [33]. Metallic centers, on the other hand, do not evaporate, resulting in a transition metal decorated porous carbon framework. Since pure carbon structures have much higher electrical conductivity than organic linkers, the metal-doped nanoporous carbon exhibits higher conductivity than pristine MOF. Additionally, nanoporous carbons are known for their chemical stability [34]. To ensure a desired structure, proper carbonization settings are crucial. Factors such as ramp-up temperature speed, carbonization temperature, process duration, and inert gas flow influence the final product, among which, the holding temperature is the most significant [35].

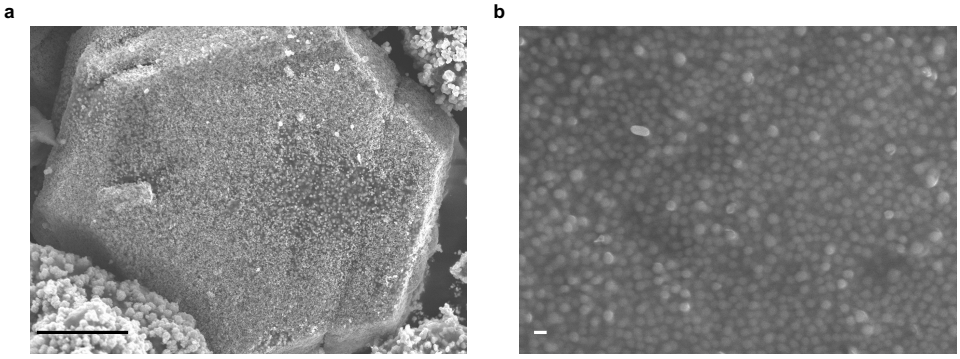

Figure 2.2: SEM Figures of carbonized Cu-BTC at 650∘C in different magnifications **a** 10 μm and **b**, 100 nm. Formation of Copper clusters smaller than 100 nm on the surface of MOF framework is visible.

Fig. 2.2 represents the scanning electron microscopic images of carbonized HKUST-1 MOF known as Cu-BTC, at the holding temperature of 650°C. As can be seen, the copper clusters form on the surface of the carbon framework with similar morphology

as the pristine MOF crystals. These clusters act now as catalytic sites whereas the carbon framework in the substrate helps with better charge transfer resulting in higher current density than the pristine MOF. In this regard, K. Zhao et al. [36] carbonized Cu-BTC at 900 °C, 1000 °C and 1100 °C. The results showed that the 1000 °C sample has a FE of about 45 % for CH_3OH and 27 % for C_2H_5OH at a potential of -0.3 V vs SHE. The electrode was made of an ink containing active material, high-purity water and Nafion deposited on commercial carbon paper using a spin coating technique. A two-compartment electrolysis cell was filled with 0.1 M $KHCO_3$ electrolyte and equipped with a Nafion membrane for ion transport. They also found that with increasing temperature, the pore size and thus the specific surface area decreases. Nevertheless, the 1000 °C sample showed better performance for CO_2RR than the 900 °C one. This was attributed to the lower charge transfer resistance of the 1000 °C sample, Showing that the specific surface area is not the only important factor to consider for a CO_2RR catalyst when considering the charge transfer parameter.

Among the electrocatalytic materials produced by MOF template carbonization for CO_2RR, ZIF-derived carbons are predominant. Specifically, those derived from ZIF-8, are particularly noteworthy. in a different study on carbonized MOFs, since zinc is not an electrocatalytically active metal for CO_2RR, it is removed during the high-temperature carbonization process and thus, various strategies have been developed to incorporate active TM into the structure. Consequently, several studies have combined Fe with ZIF-8 to produce Fe-containing N-doped carbon electrocatalysts for CO_2 to CO conversion[37]. This material achieved 97% FE for CO at -0.56 V vs. RHE, whereas its Fe-free counterpart reached 100% FE(C)O but required a higher potential of -0.86 V vs. RHE.

2.4. MOFs on Conductive Substrates

One of the limitations of MOFs is their low electrical conductivity, which restricts their electrochemical applications. Graphene which is a one-atom-thick carbon lattice with a cellular structure, offers exceptional electronic conductivity and a large surface area [38]. These properties enhance interactions with MOFs, making it an ideal anchor material with significant potential for improving the performance of MOF-based electrocatalysts [39]. Moreover, the two-dimensional (2D) non-metallic semiconductor g-C_3N_4 has garnered significant attention in recent scientific research. g-C_3N_4 possesses remarkable characteristics, such as excellent physicochemical properties, an ideal band gap, a distinctive optoelectronic structure, high stability in air (up to 600°C), low cost, and abundant availability in nature. Although this specific composite has mostly been utilized as a photo(electro)catalyst in CO_2RR due to its small bandgap [40]. In addition to these materials, carbon nanotubes (CNTs) are emerging as another highly promising candidate for functional applications. CNTs are highly structured carbon allotropes with a large aspect ratio. They exist in two primary forms: single-walled carbon nanotubes, with diameters ranging from 0.4 to 2 nm, and multi-walled carbon nanotubes, with diameters spanning

2 to 100 nm [41]. Both types are characterized by exceptional tensile strength, ultra-lightweight nature, and remarkable chemical and thermal stability. One example of this composite is [PCN-222(Fe)/CNTs], synthesized via a solvothermal method by incorporating iron porphyrin-centered PCN-222(Fe) onto CNTs. This composite exhibited excellent performance in CO_2 electroreduction, achieving a Faradaic efficiency (FE) of 90% for CO production at an overpotential of -0.6 V, at the optimal ratio of m(Fe-TCPP):m(CNTs) = 1:30. The enhanced performance was attributed to the conductive support provided by CNTs, which increased electrical conductivity and improved the overall structure of the MOF composite [42].

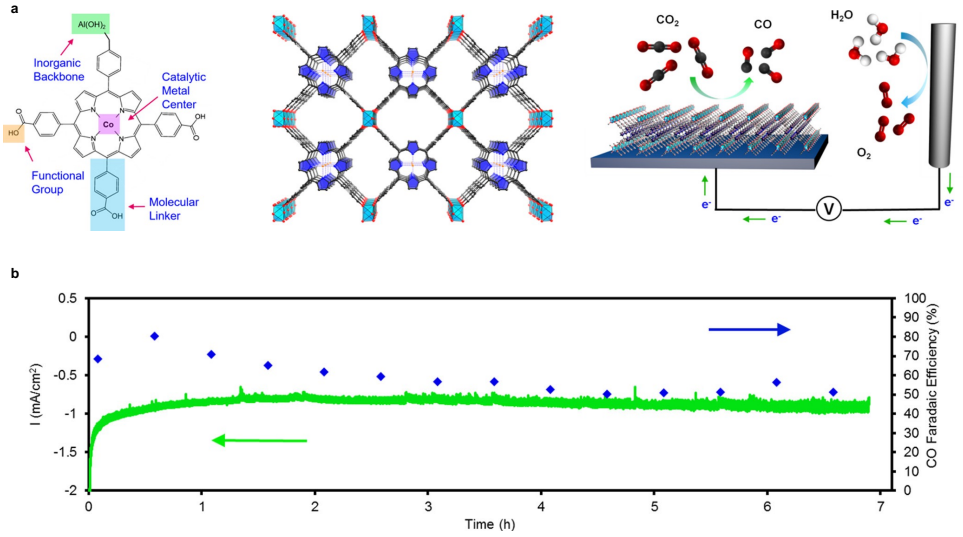

Figure 2.3: a, The organic building units, in the form of cobalt-metalated TCPP, assembled into a 3D MOF, Al2(OH)2TCPP-Co with variable inorganic building blocks. In the structure (in the middle), each carboxylate is bound to the aluminum inorganic backbone. The MOF is integrated with a conductive substrate to achieve a functional CO_2 electrochemical reduction system (in the right). **b**, Stability of the MOF catalyst evaluated by chronoamperometric measurements in combination with faradaic efficiency measurements. Reprinted with permission from [43].

In another example, a $ReL(CO)_3Cl$ (L = 2,2-bipyridine-5,5-dicarboxylic acid) thin film was grown on the surface of an FTO conductive glass electrode, exhibiting 93 ± 5% Faradaic efficiency for CO production, which is the highest reported so far and exceeds those reported for covalant organic frameworks thin films [44]. In the context of MOF-FTO composites, in a study by Nikolay, et al. [43], examination of a cobaltporphyrin MOF, $Al_2(OH)_2$TCPP-Co (TCPP-H2 - 4,4',4",4"'-(porphyrin-5,10,15,20-tetrayl)tetrabenzoate) revealed a selectivity for CO production in excess of 76% and stability over 7 hours (Fig. 2.3b).

2.5. MOFs on Porous Materials

MOFs could be also incorporated inside other porous structures such as porous carbon, Ni foam and in the form of core shell with other MOFs [45]. Considering the inherent diversity of MOFs, combining different MOFs offers significant potential for advancements in synthesis, structural design, and performance applications [46]. Building MOFs@MOFs is not only of interest for structural research but also an efficient approach to boost application performance by harnessing the synergistic properties of two distinct MOFs. In a 2020 review study by Wu, Ming-Xue, et al., it is well discussed that for selective catalysis, many MOFs@MOFs catalysts are typically designed with active metal nanoparticle-loaded MOFs as core materials and MOFs with tailored pore sizes serving as the filtering shell [47]. While limited research has focused on creating selective MOFs@MOFs catalysts electrochemical CO_2RR, this approach holds significant potential for further development. An example of MOF-MOF composites is CuBi-based metal-organic frameworks (HKUST-1 and CAU-17) supported in gas diffusion electrodes showed the FE of 28.3 % for production of Ethanol. The findings initially revealed that incorporating bismuth as a co-catalyst reduced the required overpotential, indicating a synergistic interaction between copper and bismuth in the CO_2 reduction pathway [48]. A similar case applies to the incorporation of MOFs into porous carbon materials such as carbon black. In a study by Raut, Vrushali, et al., it was demonstrated that MOF-5 on carbon black supports exhibits significantly higher conductivity compared to either pristine MOF-5 or carbon black alone in alkaline solutions, which could be advantageous for CO_2RR [49]. Another example of MOF-porous carbon composite is a recent study by Krishnamoorthy, et al. [50] which demonstrates the high efficiency of a composite of HKUST-1 and activated carbon as an electrocatalyst for CO_2 reduction. In this study, HKUST-1 nanoparticles were embedded into a conductive porous carbon, creating strong π-π interactions between the aromatic linkers od MOF and the graphitic carbon, leading to a lateral conductivity of 17.2 S/m. The composite showed a high electroactive surface coverage of 155 nmol/cm^2, and in CO_2-saturated conditions, exhibited excellent catalytic performance. The onset potential for CO_2 reduction was -0.31 V vs. RHE, with a high reduction current density of -18 mA/cm^2 at -1.0 V. Additionally, the composite remained stable during 12 hours of operation, and formic acid was identified as the main product.

2.6. MOF-Polymer/Polyoxometalate Composites

The commercialization of MOFs has been hindered by their crystalline or microcrystalline forms (e.g., powders), which limit their integration into various technologies [51]. To address this, efforts have been made to develop processable materials that combine MOFs with polymers, enhancing their practical utility. These materials are being developed using two approaches: a top-down method where MOFs are synthesized first and then integrated into polymers, and a bottom-up method where hybrid materials are formed concurrently with MOF synthesis. Common polymers used in the synthesis of MOF/polymer composites are shown in Fig **??**. The use of MOF/polymer composites in CO_2RR also need more scientific attention. In a

2020 study, Yang et. al, using a NiMOFpolymer composite as a precursor to pyrolysis, prepared a catalyst that consists of highly dispersed NiNx species. It was shown that incorporating a polymer within the MOF pores helps stabilize the collapsible MOF structure and prevents nickel aggregation during pyrolysis. This process results in the formation of single-atom nickel species within nitrogen-doped carbon, significantly enhancing activity, CO selectivity, and stability [52, 53].

Polyoxometalates (POMs) are nanoscale, discrete metal-oxygen clusters composed of earth-abundant metals and exhibit unique structures. Often referred to as electronic sponges [54]. POMs can hold a large number of electrons and engage in reversible, stepwise multi-electron transfer processes while maintaining their structural integrity. Incorporating POMs into MOF channels can shorten the electron transport distance and improve the efficiency of electron transfer from the electrode to the active sites of the electrocatalyst, thereby enhancing the effectiveness of CO_2RR [55, 56]. Research into POMs and MOFs is currently gaining momentum due to their unique structural features, catalytic potential, and other inherent properties. For instance, due to their high electron mobility, PCN-222(Co) has increasingly been selected as a supportive framework for Co-metalloporphyrins, which consist of active single cobalt metal sites and conjugated π-electron porphyrin planes [21].

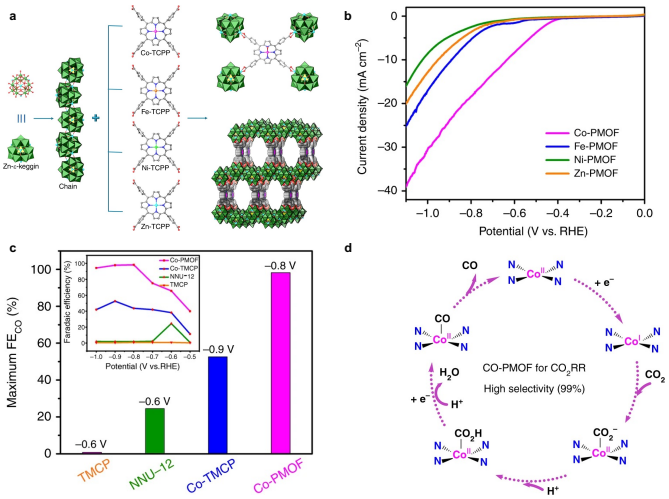

Figure 2.4: a, Schematic illustration of the structures of M-PMOFs (M= Co, Fe, Ni, Zn). Linker = TCPP and zigzag POM chains. **b**, Linear sweep voltammetric curves showing electrocatalytic performances of different composites. **c**, Maximum FECO of different composites. **d**, Proposed mechanistic scheme for the CO_2RR on Co-PMOF. [57].

As an example, a directional electron-transfer channel was successfully constructed at a molecular level by synthesizing mixed-valence POM@MOFs composites through post-modification. The combination of POMs and catalytic single-metal site Co in the porphyrin-based MOF resulted in a composite with enhanced electron-transfer

efficiency. Catalytic CO_2RR using H-POM@PCN-222(Co) exhibited a high Faradaic efficiency for CO (96.2%) and satisfying stability for over 10 hours. DFT calculations confirmed that POM introduction accelerated multi-electron transfer, enriching the electron density at the Co center and reducing RDS energy in the CO_2RR process [58].

Furthermore, assembling reductive polyoxometalates (POMs) and metalloporphyrins to construct MOFs are shown to be promising candidates to enhance the efficiency and selectivity of CO_2RR. Polyoxometalate-metalloporphyrin organic frameworks (PMOFs) facilitate efficient electron transfer in electrocatalytic CO_2 reduction due to the direct communication between the POM unit and metalloporphyrin. Reported in a novel strudy by Yi-Rong, et al. [57] Co-PMOF stands out, selectively converting CO_2 to CO with a remarkable 99% faradaic efficiency, at -0.8 V, and excellent stability for over 36 hours. Moreover, DFT calculations highlight the superior performance of Co-PMOF and the synergistic effect between reductive POM and Co-porphyrin.

2.7. MOF / MXene Composites

Metal-Organic Frameworks offer the combined benefits of both heterogeneous and homogeneous catalysts. Integrating MOFs with conductive two-dimensional MXene nanosheets can further enhance their electrocatalytic efficiency. The MXene@MOF hybrids exhibit superior performance due to their increased surface area, greater number of accessible active sites, enhanced catalytic activity, and improved stability [59]. An example of this, Fe-Nx/N/Ti_3C_2, was synthesized by pyrolyzing MOFs supported by Ti_3C_2 MXene. The negative charge of Ti_3C_2 MXene allows MOFs to anchor firmly on its surface, preventing aggregation, while its metallic conductivity enhances electron transfer. The strong interaction between Fe-N_x-C and Ti_3C_2 MXene also helps regulate the catalytic activity [60]. However, there are not many studies on the use of MXene-MOF composites for CO_2RR, this example shows the high potential of these materials.

2.8. Conclusion and Outlook

MOF composites, due to their unique structural features, are increasingly being developed to replace conventional electrocatalysts for converting CO_2 into valuable products. While the application of MOF composites for CO_2RR has shown promise, there are not many studies in this topic. In this regard, more understanding of the performance of MOF composites as electrocatalysts will help designing more efficient compounds. Moreover, most CO_2RR studies using MOF composites have only been demonstrated in labs, and scaling this process to an industrial level is crucial to addressing atmospheric CO_2. Notably, MOF composite electrocatalysts are considered to be a cost-effective catalyst materials. Thus, further studies are essential to refine these materials for electrochemical CO_2 reduction. The current research indicates that MOF composites have significantly improved electrocatalytic performance for CO_2RR comparing to conventional catalyst materials. Despite advancements, their use in this area is still in the early stages. Practical applications are hindered by challenges such as limited recycling and stability under certain reaction conditions. Therefore, the

development of MOF composites with more stable structures is necessary for broader applications.

Additionally, while many methods for synthesis of MOF composites have been reported, each comes with limitations. It is essential to explore new, versatile approaches to construct functional MOF materials, particularly for controlling guest species within MOF matrices. Significant attention has also been given to MOFs that are responsive to environmental stimuli, opening up the possibility of creating smart, responsive electrocatalysts. Further research will clarify the relationship between the structure and function of MOF composites and aid in the design of innovative materials for CO_2RR and other energy conversion applications. In summary, addressing the current challenges through more in-depth research will pave the way for the development of low-cost, high-performance MOF composites. This progress will ultimately enable benchmark performances for electrochemical CO_2 reduction in practical renewable energy applications.

BIBLIOGRAPHY

[1] J. Yu, C. Mu, B. Yan, X. Qin, C. Shen, H. Xue, and H. Pang. "Nanoparticle/MOF composites: preparations and applications". In: *Materials Horizons* 4.4 (2017), pp. 557–569.

[2] Y.-S. Wei, M. Zhang, R. Zou, and Q. Xu. "Metal–organic framework-based catalysts with single metal sites". In: *Chemical Reviews* 120.21 (2020), pp. 12089–12174.

[3] M. Li, H. Wang, W. Luo, P. C. Sherrell, J. Chen, and J. Yang. "Heterogeneous single-atom catalysts for electrochemical CO_2 reduction reaction". In: *Advanced Materials* 32.34 (2020), p. 2001848.

[4] J. Shan, C. Ye, Y. Jiang, M. Jaroniec, Y. Zheng, and S.-Z. Qiao. "Metal-metal interactions in correlated single-atom catalysts". In: *Science Advances* 8.17 (2022), eabo0762.

[5] Z. Zhang, Z. Yang, L. Liu, Y. Wang, and S. Kawi. "Catalytic CO_2 Conversion to C1 Chemicals over Single-Atom Catalysts". In: *Advanced Energy Materials* 13.42 (2023), p. 2301852.

[6] A. Xu, S.-F. Hung, A. Cao, Z. Wang, N. Karmodak, J. E. Huang, Y. Yan, A. Sedighian Rasouli, A. Ozden, F.-Y. Wu, *et al.* "Copper/alkaline earth metal oxide interfaces for electrochemical CO_2-to-alcohol conversion by selective hydrogenation". In: *Nature Catalysis* 5.12 (2022), pp. 1081–1088.

[7] M. Jouny, W. Luc, and F. Jiao. "General techno-economic analysis of CO_2 electrolysis systems". In: *Industrial & Engineering Chemistry Research* 57.6 (2018), pp. 2165–2177.

[8] L. Majidi, A. Ahmadiparidari, N. Shan, S. N. Misal, K. Kumar, Z. Huang, S. Rastegar, Z. Hemmat, X. Zou, P. Zapol, *et al.* "2D copper tetrahydroxyquinone conductive metal-organic framework for selective CO_2 electrocatalysis at low overpotentials". In: *Advanced Materials* 33.10 (2021), p. 2004393.

[9] T. Yan, P. Wang, Z.-H. Xu, and W.-Y. Sun. "Copper (II) frameworks with varied active site distribution for modulating selectivity of carbon dioxide electroreduction". In: *ACS Applied Materials & Interfaces* 14.11 (2022), pp. 13645–13652.

[10] C. F. Wen, F. Mao, Y. Liu, X. Y. Zhang, H. Q. Fu, L. R. Zheng, P. F. Liu, and H. G. Yang. "Nitrogen-stabilized low-valent Ni motifs for efficient CO_2 electrocatalysis". In: *ACS Catalysis* 10.2 (2019), pp. 1086–1093.

[11] Y.-Y. Liu, H.-L. Zhu, Z.-H. Zhao, N.-Y. Huang, P.-Q. Liao, and X.-M. Chen. "Insight into the Effect of the d-Orbital Energy of Copper Ions in Metal–Organic Frameworks on the Selectivity of Electroreduction of CO_2 to CH4". In: *Acs Catalysis* 12.5 (2022), pp. 2749–2755.

[12] X. Jiang, H. Li, J. Xiao, D. Gao, R. Si, F. Yang, Y. Li, G. Wang, and X. Bao. "Carbon dioxide electroreduction over imidazolate ligands coordinated with Zn (II) center in ZIFs". In: *Nano Energy* 52 (2018), pp. 345–350.

[13] Y. Zhang, L.-Z. Dong, S. Li, X. Huang, J.-N. Chang, J.-H. Wang, J. Zhou, S.-L. Li, and Y.-Q. Lan. "Coordination environment dependent selectivity of single-site-Cu enriched crystalline porous catalysts in CO_2 reduction to CH4". In: *Nature Communications* 12.1 (2021), p. 6390.

[14] J. Liu, D. Yang, Y. Zhou, G. Zhang, G. Xing, Y. Liu, Y. Ma, O. Terasaki, S. Yang, and L. Chen. "Tricycloquinazoline-based 2D conductive metal-organic frameworks as promising electrocatalysts for CO_2 reduction". In: *Angewandte Chemie International Edition* 60.26 (2021), pp. 14473–14479.

[15] X. Zhang, Y. Zhang, Q. Li, X. Zhou, Q. Li, J. Yi, Y. Liu, and J. Zhang. "Highly efficient and durable aqueous electrocatalytic reduction of CO 2 to HCOOH with a novel bismuth–MOF: experimental and DFT studies". In: *Journal of Materials Chemistry A* 8.19 (2020), pp. 9776–9787.

[16] Z. Weng, Y. Wu, M. Wang, J. Jiang, K. Yang, S. Huo, X.-F. Wang, Q. Ma, G. W. Brudvig, V. S. Batista, *et al.* "Active sites of copper-complex catalytic materials for electrochemical carbon dioxide reduction". In: *Nature communications* 9.1 (2018), p. 415.

[17] C. A. Downes and S. C. Marinescu. "Electrocatalytic metal–organic frameworks for energy applications". In: *ChemSusChem* 10.22 (2017), pp. 4374–4392.

[18] L. Sun, M. G. Campbell, and M. Dinc. "Electrically conductive porous metal–organic frameworks". In: *Angewandte Chemie International Edition* 55.11 (2016), pp. 3566–3579.

[19] X. Zhao, H. Xu, X. Wang, Z. Zheng, Z. Xu, and J. Ge. "Monodisperse metal–organic framework nanospheres with encapsulated core–shell nanoparticles Pt/Au@ Pd@{CO_2 (oba) 4 (3-bpdh) 2} 4H2O for the highly selective conversion of CO_2 to CO". In: *ACS applied materials & interfaces* 10.17 (2018), pp. 15096–15103.

[20] X. Tan, C. Yu, C. Zhao, H. Huang, X. Yao, X. Han, W. Guo, S. Cui, H. Huang, and J. Qiu. "Restructuring of Cu2O to Cu2O@ Cu-metal–organic frameworks for selective electrochemical reduction of CO_2". In: *ACS applied materials & interfaces* 11.10 (2019), pp. 9904–9910.

[21] K.-G. Liu, F. Bigdeli, A. Panjehpour, A. Larimi, A. Morsali, A. Dhakshinamoorthy, and H. Garcia. "Metal organic framework composites for reduction of CO_2". In: *Coordination Chemistry Reviews* 493 (2023), p. 215257.

[22] X.-G. Zhang, X. Jin, D.-Y. Wu, and Z.-Q. Tian. "Selective electrocatalytic mechanism of CO_2 reduction reaction to CO on silver electrodes: a unique reaction intermediate". In: *The Journal of Physical Chemistry C* 122.44 (2018), pp. 25447–25455.

[23] X. Jiang, H. Wu, S. Chang, R. Si, S. Miao, W. Huang, Y. Li, G. Wang, and X. Bao. "Boosting CO 2 electroreduction over layered zeolitic imidazolate frameworks decorated with Ag 2 O nanoparticles". In: *Journal of Materials Chemistry A* 5.36 (2017), pp. 19371–19377.

[24] J.-D. Yi, R. Xie, Z.-L. Xie, G.-L. Chai, T.-F. Liu, R.-P. Chen, Y.-B. Huang, and R. Cao. "Highly selective CO_2 electroreduction to CH4 by in situ generated Cu2O single-type sites on a conductive MOF: stabilizing key intermediates with hydrogen bonding". In: *Angewandte Chemie* 132.52 (2020), pp. 23849–23856.

[25] X. Xie, X. Zhang, M. Xie, L. Xiong, H. Sun, Y. Lu, Q. Mu, M. H. Rummeli, J. Xu, S. Li, *et al.* "Au-activated N motifs in non-coherent cupric porphyrin metal organic frameworks for promoting and stabilizing ethylene production". In: *Nature Communications* 13.1 (2022), p. 63.

[26] Q.-L. Zhu and Q. Xu. "Metal–organic framework composites". In: *Chemical Society Reviews* 43.16 (2014), pp. 5468–5512.

[27] K. A. Adegoke, J. O. Ighalo, J. Conradie, C. R. Ohoro, J. F. Amaku, K. O. Oyedotun, N. W. Maxakato, K. G. Akpomie, E. S. Okeke, C. Olisah, *et al.* "Metal-organic framework composites for electrochemical CO_2 reduction reaction". In: *Separation and Purification Technology* (2024), p. 126532.

[28] J.-M. Huang, X.-D. Zhang, J.-Y. Huang, D.-S. Zheng, M. Xu, and Z.-Y. Gu. "MOF-based materials for electrochemical reduction of carbon dioxide". In: *Coordination Chemistry Reviews* 494 (2023), p. 215333.

[29] S.-Y. Zhang, Y.-Y. Yang, Y.-Q. Zheng, and H.-L. Zhu. "Ag-doped Co3O4 catalyst derived from heterometallic MOF for syngas production by electrocatalytic reduction of CO_2 in water". In: *Journal of Solid State Chemistry* 263 (2018), pp. 44–51.

[30] A. I. Skoulidas. "Molecular dynamics simulations of gas diffusion in metal-organic frameworks: argon in CuBTC". In: *Journal of the American Chemical Society* 126.5 (2004), pp. 1356–1357.

[31] Y. T. Guntern, J. R. Pankhurst, J. Vávra, M. Mensi, V. Mantella, P. Schouwink, and R. Buonsanti. "Nanocrystal/metal–organic framework hybrids as electrocatalytic platforms for CO_2 conversion". In: *Angewandte Chemie* 131.36 (2019), pp. 12762–12769.

[32] H. Liu, H. Wang, Q. Song, K. Küster, U. Starke, P. A. van Aken, and E. Klemm. "Assembling metal organic layer composites for high-performance electrocatalytic CO_2 reduction to formate". In: *Angewandte Chemie International Edition* 61.9 (2022), e202117058.

[33] R.-M. Wang, S.-R. Zheng, and Y. Zheng. "Reinforced materials". In: Dec. 2011, pp. 56–60. ISBN: 9780857092212. DOI: 10.1533/9780857092229.1.29.

[34] B. N. Bhadra, A. Vinu, C. Serre, and S. H. Jhung. "MOF-derived carbonaceous materials enriched with nitrogen: Preparation and applications in adsorption and catalysis". In: *Materials Today* 25 (2019), pp. 88–111. ISSN: 1369-7021. DOI: https://doi.org/10.1016/j.mattod.2018.10.016. URL: https://www.sciencedirect.com/science/article/pii/S1369702118306655.

[35] V. K. Abdelkader-Fernández, D. M. Fernandes, and C. Freire. "Carbon-based electrocatalysts for CO_2 electroreduction produced via MOF, biomass, and other precursors carbonization: A review". In: *Journal of CO_2 Utilization* 42 (2020), p. 101350. ISSN: 2212-9820. DOI: https://doi.org/10.1016/j.jcou.2020.101350. URL: https://www.sciencedirect.com/science/article/pii/S221298202030980X.

[36] K. Zhao, Y. Liu, X. Quan, S. Chen, and H. Yu. "CO_2 Electroreduction at Low Overpotential on Oxide-Derived Cu/Carbons Fabricated from Metal Organic Framework". In: *ACS Applied Materials & Interfaces* 9.6 (2017), pp. 5302–5311.

[37] V. K. Abdelkader-Fernandez, D. M. Fernandes, and C. Freire. "Carbon-based electrocatalysts for CO_2 electroreduction produced via MOF, biomass, and other precursors carbonization: A review". In: *Journal of CO_2 Utilization* 42 (2020), p. 101350.

[38] Y. Peng, J. Xu, J. Xu, J. Ma, Y. Bai, S. Cao, S. Zhang, and H. Pang. "Metal-organic framework (MOF) composites as promising materials for energy storage applications". In: *Advances in Colloid and Interface Science* 307 (2022), p. 102732.

[39] S. Li and F. Huo. "Metal–organic framework composites: from fundamentals to applications". In: *Nanoscale* 7.17 (2015), pp. 7482–7501.

[40] M. Usman, Z. Zeb, H. Ullah, M. H. Suliman, M. Humayun, L. Ullah, S. N. A. Shah, U. Ahmed, and M. Saeed. "A review of metal-organic frameworks/graphitic carbon nitride composites for solar-driven green H2 production, CO_2 reduction, and water purification". In: *Journal of Environmental Chemical Engineering* 10.3 (2022), p. 107548.

[41] S. Kempahanumakkagari, K. Vellingiri, A. Deep, E. E. Kwon, N. Bolan, and K.-H. Kim. "Metal–organic framework composites as electrocatalysts for electrochemical sensing applications". In: *Coordination Chemistry Reviews* 357 (2018), pp. 105–129.

[42] e. a. Xu Lin-Wei. "The boosting of electrocatalytic CO 2-to-CO transformation by using the carbon nanotubes-supported PCN-222 (Fe) nanoparticles composite." In: *Journal of Materials Science* (2022).

[43] N. Kornienko, Y. Zhao, C. S. Kley, C. Zhu, D. Kim, S. Lin, C. J. Chang, O. M. Yaghi, and P. Yang. "Metal–organic frameworks for electrocatalytic reduction of carbon dioxide". In: *Journal of the American Chemical Society* 137.44 (2015), pp. 14129–14135.

[44] L. Ye, J. Liu, Y. Gao, C. Gong, M. Addicoat, T. Heine, C. Wöll, and L. Sun. "Highly oriented MOF thin film-based electrocatalytic device for the reduction of CO 2 to CO exhibiting high faradaic efficiency". In: *Journal of Materials Chemistry A* 4.40 (2016), pp. 15320–15326.

[45] J. Liu, C. Chen, K. Zhang, and L. Zhang. "Applications of metal–organic framework composites in CO_2 capture and conversion". In: *Chinese Chemical Letters* 32.2 (2021), pp. 649–659.

[46] Y. Xue, S. Zheng, H. Xue, and H. Pang. "Metal–organic framework composites and their electrochemical applications". In: *Journal of Materials Chemistry A* 7.13 (2019), pp. 7301–7327.

[47] M.-X. Wu, Y. Wang, G. Zhou, and X. Liu. "Core–shell MOFs@ MOFs: diverse designability and enhanced selectivity". In: *ACS Applied Materials & Interfaces* 12.49 (2020), pp. 54285–54305.

[48] J. Albo, M. Perfecto-Irigaray, G. Beobide, and A. Irabien. *Cu/Bi metal-organic framework-based systems for an enhanced electrochemical transformation of CO_2 to alcohols, J. CO_2 Util. 33 (2019) 157–165.*

[49] V. Raut, B. Bera, M. Neergat, and D. Das. "Metal-Organic Framework and Carbon Black supported MOFs as dynamic electrocatalyst for oxygen reduction reaction in an alkaline electrolyte". In: *Journal of Chemical Sciences* 133 (2021), pp. 1–9.

[50] K. Sathiyan, A. Dutta, V. Marks, O. Fleker, T. Zidki, R. D. Webster, and A. Borenstein. "Nano-encapsulation: overcoming conductivity limitations by growing MOF nanoparticles in meso-porous carbon enables high electrocatalytic performance". In: *NPG Asia Materials* 15.1 (2023), p. 18.

[51] Z. Chen, M. C. Wasson, R. J. Drout, L. Robison, K. B. Idrees, J. G. Knapp, F. A. Son, X. Zhang, W. Hierse, C. Kühn, *et al.* "The state of the field: from inception to commercialization of metal–organic frameworks". In: *Faraday discussions* 225 (2021), pp. 9–69.

[52] S. Yang, J. Zhang, L. Peng, M. Asgari, D. Stoian, I. Kochetygov, W. Luo, E. Oveisi, O. Trukhina, A. H. Clark, *et al.* "A metal–organic framework/polymer derived catalyst containing single-atom nickel species for electrocatalysis". In: *Chemical science* 11.40 (2020), pp. 10991–10997.

[53] B. Deeraj, J. S. Jayan, A. Raman, A. Asok, R. Paul, A. Saritha, and K. Joseph. "A comprehensive review of recent developments in metal-organic framework/polymer composites and their applications". In: *Surfaces and Interfaces* 43 (2023), p. 103574.

[54] Y. Liu, C. Tang, M. Cheng, M. Chen, S. Chen, L. Lei, Y. Chen, H. Yi, Y. Fu, and L. Li. "Polyoxometalate@ metal–organic framework composites as effective photocatalysts". In: *ACS Catalysis* 11.21 (2021), pp. 13374–13396.

[55] J. Du, Y.-Y. Ma, W.-J. Cui, S.-M. Zhang, Z.-G. Han, R.-H. Li, X.-Q. Han, W. Guan, Y.-H. Wang, Y.-Q. Li, *et al.* "Unraveling photocatalytic electron transfer mechanism in polyoxometalate-encapsulated metal-organic frameworks for high-efficient CO_2 reduction reaction". In: *Applied Catalysis B: Environmental* 318 (2022), p. 121812.

[56] X.-X. Li, J. Liu, L. Zhang, L.-Z. Dong, Z.-F. Xin, S.-L. Li, X.-Q. Huang-Fu, K. Huang, and Y.-Q. Lan. "Hydrophobic polyoxometalate-based metal-organic framework for efficient CO_2 photoconversion". In: *ACS applied materials & interfaces* 11.29 (2019), pp. 25790–25795.

[57] Y.-R. Wang, Q. Huang, C.-T. He, Y. Chen, J. Liu, F.-C. Shen, and Y.-Q. Lan. "Oriented electron transmission in polyoxometalate-metalloporphyrin organic framework for highly selective electroreduction of CO_2". In: *Nature communications* 9.1 (2018), p. 4466.

[58] M.-L. Sun, Y.-R. Wang, W.-W. He, R.-L. Zhong, Q.-Z. Liu, S. Xu, J.-M. Xu, X.-L. Han, X. Ge, S.-L. Li, *et al.* "Efficient electron transfer from electron-sponge polyoxometalate to single-metal site metal–organic frameworks for highly selective electroreduction of carbon dioxide". In: *Small* 17.20 (2021), p. 2100762.

[59] T. Xu, Y. Wang, Y. Xue, J. Li, and Y. Wang. "MXenes@ metal-organic framework hybrids for energy storage and electrocatalytic application: Insights into recent advances". In: *Chemical Engineering Journal* 470 (2023), p. 144247.

[60] W. Gu, M. Wu, J. Xu, and T. Zhao. "MXene boosted metal-organic framework-derived Fe–N–C as an efficient electrocatalyst for oxygen reduction reactions". In: *International Journal of Hydrogen Energy* 47.39 (2022), pp. 17224–17232.

3

MOF Design Strategies to Disrupt Linear Scaling Relationships and Beyond

Abstract

The increasing concentration of CO_2 in the atmosphere demands innovative solutions to mitigate its impact. The electrochemical reduction of CO_2 (CO_2RR) offers a sustainable platform to convert CO_2 into valuable products, such as fuels and chemicals, contributing to a carbon-neutral cycle. Metal-organic frameworks (MOFs), with their high porosity, large surface area, and tunable structures, have emerged as a promising class of catalysts for CO_2RR. This review delves into the fundamental principles that make MOFs effective for more selective CO_2RR, particularly their ability to disrupt linear scaling relationships among key intermediates. We explore various design strategies to enhance the selectivity and overall performance of MOF electrocatalysts, including reducing dimensionality and tailoring structural and chemical properties. Key advancements in the design and modification of metal centers, organic linkers, and coordination environments are thoroughly examined, supported by insights from both theoretical and experimental studies. Special emphasis is placed on two-dimensional (2D) MOFs, such as TM-Hexaaminobenzene $(TMs)_3(HAB)_2$ and TM-Phthalocyanine (TMs-Pc), which exhibit strong in-plane conjugation and tunable catalytic properties. Using high-throughput density functional theory calculations, we uncover essential design principles and intrinsic descriptors that connect the atomic properties of transition metals to their catalytic activity. These insights not only enhance our understanding of MOFs' role in CO_2RR but also pave the way for the development of high-performing, selective, and efficient MOF catalysts for sustainable CO_2 conversion.

Modified portions of this chapter *will be submitted* as a scientific manuscript:
K. Roohi, N. Khossossi, M. Soleimani, S. Canossa, A. Mol, P. Dey, P. Taheri, Metal-Organic Framework Catalysts for Disturbing Linear Scaling Relationship and Beyond for Enhanced Selectivity in Electrochemical CO_2 Reduction Reaction

3.1. Introduction

Energy consumption continues to grow rapidly and is expected to reach a level of approximately 1.3 times greater than the current consumption rate by 2040 [1]. Fossil fuels will likely continue to be a major source of energy for the foreseeable future. It is predicted that in the coming few decades, about 500 gigatons of carbon dioxide (CO_2) will be generated from the combustion of fossil fuels, leading to excessive anthropomorphic CO_2 emission and causing various fundamental problems associated with resources, environment, and climate [2, 3]. For over 30 years, CO_2 emission issues have received significant attention and increasing investments for closing the carbon cycle [4]. To maintain environmental stability and support a sustainable society, the amount of CO_2 produced should equal the amount consumed, keeping the atmospheric CO_2 concentration constant [5].

Achieving this target requires reducing total CO_2 emissions by shifting the consumption paradigm from traditional fossil fuels to low-carbon energy sources such as nuclear, wind, and solar. However, the intrinsic intermittency of solar or wind resources requires long-term and large-scale storage for their further deployment as replacements for fossil fuels [6], whereas nuclear power development is hampered by public sentiment over its safety, and the disposal of its radioactive by-products [7]. Therefore, considerable research has been conducted on the topic of developing techniques for consumption of CO_2 as an alternative solution. So far, various approaches have been established for converting CO_2 into valuable products. These techniques include biological processes [8], chemical processes such as, hydrogeneration [9], carboxylation with CO_2 [10], mineralization [11], photochemical processes, [12], plasma technologies [13], and electrochemical methods [14].

Among various methods, the electrochemical CO_2 reduction reaction (CO_2RR) stands out due to several advantages. Firstly, it can be powered by renewable energy sources such as wind, solar, hydro, and biomass, allowing energy to be stored in synthetic chemicals [15]. Additionally, electrochemical systems have a relatively small footprint, can operate near room temperature, and require minimal chemical inputs [16]. This approach offers highly controllable reaction conditions, making it easier to adjust electrochemical parameters while maintaining high conversion efficiency [17]. The compact and modular design of electrochemical reactors also makes them suitable for extensive industrial applications [18]. Moreover, many CO_2RR products, such as syngas a key building block in petrochemical processesor fuels, can be seamlessly integrated into existing infrastructure without requiring significant changes [19]. Thus, electrocatalytic CO_2 reduction, when coupled with intermittent renewable energy sources, offers a promising path to increase the adoption of renewable energy in the fuel and chemical industries. However, the bond energy of stable C=O in CO_2 molecule is 805 kJ/mol requiring a significant activation energy to convert CO_2 to CO_2^* radical anion [20]. This step, which considers to be the rate limiting step in CO_2 conversion pathway, causes a sluggish kinetic [21]. Furthermore, at potentials significantly higher than thermodynamic thresholds, CO_2 can be transformed into a wide range of products, including formic acid, carbon monoxide, methanol, methane, ethylene, ethanol, acetate, etc. [22, 23]. In addition to the multiplicity of product challenges, another complicating aspect is the competing hydrogen evolution

reaction (HER) in aqueous environments with relatively fast kinetics [24]. Thus, an electrocatalyst is an essential element of CO_2RR. The interaction of the CO_2 molecules and other reaction intermediates with the surface of the catalyst determines the efficiency of the CO_2RR. These interactions influence the reaction pathways and, therefore, the activity and selectivity of the process [25].

Maximizing the efficiency of the CO_2RR primarily involves suppressing competing HER, however, when multiple reduction products are present, it also involves maximizing selectivity towards one specific desired product [26]. To minimize HER, many operating-related modifications could be done, such as using high pH electrolytes to reduce the availability of aqueous protons [27]. In addition to HER, in multi-product processes such as CO_2RR, the binding energy of one intermediate (e.g., *COOH) is often linearly related to that of another (e.g., *CO), due to the interaction between adsorbed intermediate and metal d-states [28]. While this relationship simplifies catalyst design by providing a consistent trend, it also imposes a fundamental limitation: optimizing the adsorption energy for one intermediate often inadvertently affects others, making it challenging to design an optimal catalyst using transition metals [29]. Breaking this relationship through catalyst design is essential for achieving higher selectivity and efficiency in CO_2RR. To address this issue, a particularly promising approach is ensemble control, which entails identifying the smallest active site and its surrounding space essential for the desired reaction, and then deliberately tailoring it [30]. While atomically controlling the metallic based catalysts is challenging, metal-ligand complexes, such as Metal-Organic Frameworks (MOFs), offer exceptional structural tunability, making them ideal materials for this purpose.

MOFs, are crystalline structures composed of metal nodes and organic linker with various abundant heteroatoms [31]. In the context of aqueous electrocatalytic CO_2 reduction, owning to their uniform pores, constructed by coordinating bridging organic ligands with metal centers, MOFs provide a large surface area [32]. Moreover, the structured nature of MOFs enables precise control of the active catalytic center at the atomic scale [33]. It is commonly accepted that the redox-active metal sites within MOFs, such as Fe, Co, Ni, Cu, or Mn, are the active sites capable of delivering catalytic activity [34]. In the synthesis of MOFs, a variety of metal nodes and organic molecules can be incorporated, resulting in over 20,000 reported MOFs [35]. Nevertheless, despite possessing an active tunable molecular structure, the limited charge transport characteristics of chemically stable MOFs, frequently hinder their utilization as direct electrocatalysts. Therefore, it is important to carefully select the metal and ligand species, engineer the MOF structure, and optimize its molecular configuration to potentially offer satisfactory electrocatalytic activity and selectivity. This could achieved by investigating the high-energy intermediates of the reaction through mechanistic studies as well as making predictions based on computational analyses of the activity, composition, and structure of MOFs [36].

Despite significant advancements in MOF-based electrocatalysis, existing review studies often focus on cataloging state-of-the-art MOFs without delving deeply into the mechanistic insights that connect their structural properties to catalytic performance. A major knowledge gap lies in understanding how the tunability of

MOFs such as modifying metal centers, linkers, and coordination environments disrupts fundamental limitations like linear scaling relationships to enhance selectivity. Additionally, while 2D MOFs and conductive MOFs have recently garnered attention, their unique advantages in CO_2RR, including electronic conductivity and active site accessibility, remain underexplored in the context of systematic design principles. Furthermore, the integration of theoretical approaches, such as density functional theory (DFT), with experimental findings to establish predictive frameworks for catalyst performance is still in its infancy. Addressing these gaps can provide a roadmap for leveraging MOF design to overcome long-standing challenges in CO_2RR, particularly in achieving high selectivity and stability under practical conditions.

3.2. Methodology

Computational Details

To calculate the free energy of elementary reactions in the CO_2 reduction process, we utilize the computational hydrogen electrode (CHE) model. This method equates the energy of a H^+/e^- pair to half the energy of a hydrogen molecule ($(1/2)H_2$) at equilibrium potential[37]. The free energy for the reactions is determined by adding corrections for zero-point energy (E_{ZPE}), heat capacity (C_p), temperature (T), and entropy (S) to the DFT-calculated total energy (E_{DFT}) [38]:

$$G = E_{DFT} + E_{ZPE} + \int C_p dT - TS \tag{3.1}$$

The corrections for E_{ZPE}, C_p, and S are derived using statistical mechanics under the harmonic approximation, with vibrational frequencies obtained from DFT calculations. It is noted that the E_{DFT} term predominantly determines the free energy, and the variations in E_{ZPE}, C_p, and S across different materials are minimal [39]. Thus, the free energy G is computed by combining E_{DFT} with the corrections listed in Table 3.1. Furthermore, a correction of -0.51 eV is applied to the free energy of CO gas molecules to rectify significant deviations observed with the GGA-PBE functional [40]. Solvation energy corrections are included for the COOH* and CO* intermediates, with values of 0.25 eV and 0.1 eV, respectively, since the solvation effects for these intermediates in CO_2RR are very small [41]. This method ensures that the calculated equilibrium potential versus CHE for the overall half-reaction of CO_2 conversion aligns closely with experimental values measured versus RHE [42].

The comprehensive reactions for CO_2 reduction are listed as follow. [43]:

$$* + CO_{2(g)} \rightarrow *CO_2 \tag{3.2}$$

$$*CO_2 + H^+ + e^- \rightarrow *COOH \tag{3.3}$$

$$*COOH + H^+ + e^- \rightarrow *CO + H_2O_{(l)} \tag{3.4}$$

$$*CO \rightarrow * + CO_{(g)} \tag{3.5}$$

In these reactions, * denotes the active site on the TMs-MOF catalyst surface, with subscripts g and l representing gas and liquid phases, respectively. The intermediates

Table 3.1: Computed thermodynamic corrections, Zero-Point Energy (ZPE), Heat-Capacity (C_p), and entropy (S) at 298K for Free Molecules and Adsorbed Intermediates (eV).

Elements	**ZPE**	$\int C_p dT$ **(0 → 298.15K)**	**TS**
CO_2	0.31	0.10	0.620
H_2O	0.58	0.10	0.65
H_2	0.27	0.09	0.42
CO	0.14	0.09	0.67
HCOOH	0.90	0.11	1.02
$*CO_2$	0.30	0.06	0.09
*COOH	0.63	0.09	0.17
*HCOO	0.62	0.10	0.20
*HCOOH	0.82	0.05	0.09
*CO	0.22	0.05	0.08
*OH	0.40	0.03	0.04

$*CO_2$, *COOH, and *CO are adsorbed on the top of TM of $(TM)_3(HAB)_2$. Adsorption energies are determined using the following equations [44]:

$$\Delta G_{*CO_2} = G(*CO_2) - G(*) - G_{CO_2} \tag{3.6}$$

$$\Delta G_{*COOH} = G(*COOH) - G(*) - (G_{CO_2} + 0.5G_{H2}) \tag{3.7}$$

$$\Delta G_{*CO} = G(*CO) - G(*) - (G_{CO_2} + G_{H2} - G_{H2O}) \tag{3.8}$$

Here, G(*) represents the ground state energy of a clean, unabsorbed MOF surface. $G(*CO_2)$, G(*COOH), and G(*CO) are the ground state energies of surfaces with $*CO_2$, *COOH, and *CO adsorbates on $(TM)_3(HAB)_2$ surface. G_{CO_2}, G_{H2}, and G_{H2O} are the energies of gaseous or liquid CO_2, H_2, and H_2O molecules, respectively.

The calculation of the overpotential (η^{CO}) is given by:

$$\eta^{CO} = \max[\Delta G_{elem}/ne] \tag{3.9}$$

where n is the number of electron transfers per elementary reaction, and ΔG_{elem} represents the free energy (ΔG_1, ΔG_2, ΔG_3, and ΔG_4) of the elementary reactions. Note that ΔG_{elem} is calculated at equilibrium, meaning that the free energy for the electrochemical step (ΔG_2, ΔG_3) of CO_2RR is adjusted by -0.12V for the CO product.

Experimental method:

Chemicals and Synthesis

$(Cu)_2$(2,3,6,7,10,11-hexahydroxytriphenylene)$_2$ (-Cu-HHTP-MOF) was commercially purchased from CD Bioparticles. Cobalt(II) nitrate ($Cu(NO_3)_2.3H_2O$, 99.999%), benzenedicarboxylic (tp-$C_8H_6O_4$), isopropanol and, $KHCO_3$ all were purchased from Sigma-Aldrich. An ultrapure purification system (Milli-Q advantage A10) produced

the deionized water purification system (19.2 MΩcm) used to make the solutions. Ni/CoMOF [CoNi(μ_3-tp)$_2$(μ_2-pyz)$_2$] MOF was synthesized in a solvothermal reaction of 1 mmol of Co(NO$_3$)$_2$ů6H$_2$O and Ni(NO$_3$)$_2$ů6H$_2$O with 2 mmol of terephthalic acid and pyrazine in 14 mL water. The mixture was then maintained at 200řC for 48 hours and subsequently cooled to room temperature at a rate of 5řC per hour.

Electrode Preparation

Dried MOF powders were mixed with Polyvinyl alcohol (PVA) as binder and carbon black (CB) as conductivity enhancer, in a water and isopropanol solution to form an ink with an active material, PVA and CB weight ratio of 18:1:1. The ink was then drop-cast onto clean glassy carbon using a pipette and dried under ambient air.

Materials Characterization

Scanning electron microscope (SEM) observation was performed with a field emission-scanning electron microscope (JEOL JSM-7401F or Magellan 400 XHR) equipped with electron dispersive spectroscopy (EDS). Working electrodes were tested in a compact H-cell inspired by Lobaccaro et al [45]. Each compartment contained 1.8 mL of 1 M KHCO3 as electrolyte and the cathode and anode chambers were separated by an anion-exchange membrane (Selemion AMV, AGC Engineering). Before each experiment, the catholyte was purged with CO_2 for 1 hour to obtain a CO_2-saturated. Chronoamperometric electrolysis measurements were carried out at applied potential -1.6 V vs. Ag/AgCl and each potential was applied for 1 h. The cell During the chronoamperometry tests, CO_2 was purged continuously into the catholyte with a flow rate of 10 mL/min. Gas product analysis from the cathode compartment was done with gas chromatography (GC from Agilent) equipped with two thermal conductivity detectors (TCD) to measure CO_2, CO, and H_2 in 2-minute intervals. A standard calibration curve was made using custom gas mixture cylinders with known concentrations of product gasses in CO_2 (Linde gas Benelux B.V.). Liquid products were investigated with a Bruker Ascend 500 (B0 = 11.7 T) magnet equipped with a NEO console NMR machine. MestreNova software was used to deconvolute the peaks Faradaic efficiencies were calculated using equation 5.1

$$\frac{n_i NF}{jt} \tag{3.10}$$

where n_i represents the number of moles of the detected product, N is the number of the transferred electrons in a reaction, F is the Faradaic constant (s A/mol), j is the current density (A) and t is the time of the measurement in seconds.

3.3. Designing Strategies of MOFs for Selective CO_2RR

As discussed so far in the previous chapters, MOFs, due to their complex structure and their single atom catalytic sites, could enhance the chance of formation of only lower carbon CO_2RR products. Similar to most of the single atom catalysts, since the surface of the active sites are small enough, C-C coupling would be hindered and

thus, CO and formate are more probable products. Notably, a gross margin estimate indicates that both of these products, present a positive business opportunity [46]. Moreover, controlling the coordination environment of the metallic atom is more practical in MOFs rather than the other structures. The reason behind this is that the coordination environment of the metal in a MOF structure is defined by the organic linker and due to the variety of organic linkers, the design process can be highly tunable. Adding the right element to the metal catalytic sites can modify the selectivity toward desired products.

The initial step in CO_2RR involves activating the CO_2 molecule. CO_2 activation and reduction are claimed to be challenging due to the highly negative redox potential required for the first electron transfer to form the $*CO_2$ radical intermediate or because CO_2 is a highly stable molecule. However, neither of these claims are entirely correct [47]. Electrocatalysts stabilize $*CO_2$ by forming a chemical bond with CO_2, resulting in a less negative redox potential. With the appropriate electrocatalyst, CO_2 can be reduced to CO or HCOOH at low overpotential. This low-overpotential reversible catalysis is associated with a two-electron process mechanism, typically involving a single intermediate, which can be optimized using a suitable catalyst. When it comes to electrocatalytic conversion of CO_2, as mentioned before, copper plays a significant role.

In this regard, as an example, in a 2020 study, De Gregorio et al. [48] investigated the catalytic properties of tailored Cu nanocatalysts under commercially relevant current densities, demonstrating their facet-dependency on the CO_2RR selectivity. As results indicate, the selectivity towards ethylene (C_2H_4) improves in the case of using Cu (100) than other facets. Yet, five other products, including CO, are detected. As an outcome of an ealier study by Bagger et. al., it was shown that all Cu facets can bind CO* without H underpotential deposition. The enlarged. This study highlights that increasing C_{2+} efficiency involves destabilizing ΔE_{H*} while stabilizing ΔE_{CO*}. The small variation in binding energies among the data points makes it difficult to determine why some Cu facets produce more C_{2+} products, aligning with previous findings on changes in product distribution due to variations in the Cu lattice constant. However, the takeaway message is that metallic copper with different crystalline structures lacks selectivity for CO_2RR products [49]. On the other hand, having copper single atoms dispersed inside different organic platforms leads to hindering complex C_{2+} products more according to different studies [50]. This was also confirmed beforehand, in 2021, by Majidi et al. [51], that by dispersing copper atoms in the form of a MOF crystal, full selectivity towards CO could be achieved in a comparable range of current density with metallic copper. Cu-THQ owing to its two-dimensional structure, shows a high current density of almost 173 mA/cm^2 at -0.45 V versus RHE with an average Faradaic efficiency of 91% toward CO. This is an example of improving selectivity by forming complex crystals of single-atom catalytic sites, as discussed in the previous section.

In addition to that, in any catalytic reaction, it is widely known that the bonding strength of the reaction species (i.e., reactants, intermediates, and products) to the surface of the catalyst should strike a balanceneither too strong nor too weak. With the advent of DFT, simulations have emerged as fundamental tools for predicting

catalytic processes. For instance, regarding the activity of the materials, volcano plots provide a systematic approach to catalyst design. A volcano plot is a design tool in which the reaction rate (e.g, overpotential) on various catalysts is plotted against their adsorption energy. However, this is not a practical concept for explaining selectivity [30, 52, 53]. When it comes to multi-product reactions, the interaction of the key intermediates with the catalyst could determine the reaction pathway and its selectivity [29].

Three key intermediates of the CO_2RR are *COOH, *CO and *COH as previously introduced in Fig. 1.3. The bond order conservation theory and the electron counting rules suggest that the bonding energies of intermediates to the surface of the metal catalysts are interconnected linearly [30, 54]. This universal concept is called linear scaling relationship (LSR) and has been practically calculated for transition metal (TM) catalysts in CO_2RR (Fig. 3.1a and b). LSR of the binding energies of *CO and *COOH and *CHO is largely responsible for the modest FE of copper catalysts in CO_2RR. Regulating the binding energies of these intermediates on the surface of the electrocatalyst can enhance the FE of carbonous products [55]. In this regard, many techniques from alloying, doping, metal/metal oxide interfaces, grain boundaries, facets and many other structural-oriented modifications have been used to achieve this control. To further investigate the effect of structural complexity on catalytic selectivity, the relationship between the binding energies of CHO, COOH, and CO, calculated by DFT, is plotted in Fig. 3.1c and d. The studied materials for this purpose are a series of HAB-based MOFs, where HAB (hexaaminobenzene) is one of the linkers used for synthesizing a class of 2D-$TM_3(HAB)_2$ MOFs. In the same figure, the lines from different facets of TMs (known as LSR for metals, as discussed earlier) are plotted. It can be seen that these MOFs, regardless of their TM, are capable of breaking the linear scaling relationship existing between their pristine metals. This indicates that complex structures, such as MOFs, could disturb the LSR of key intermediates of CO_2RR and enhance selectivity towards one carbonous products. Additionally, coordination number and environment of the metal catalyst, plays an important role on the selectivity of the catalyst [56]. Coordination interactions with neighbouring atoms are the main way to fix metal atoms in the structure of the catalyst [57].

The recent advances in the synthesis of nanostructures and nanoparticles as well as the flexibility in their formations in terms of compositional and structural properties have allowed us to take further steps beyond metallic and metal oxide nanomaterials. In this section, we will dive into the important parameters in MOF design and synthesis that can affect the selectivity and activity of the catalyst in electrochemical CO_2 reduction reaction.

3.3.1. Metal Centres

The activity and selectivity of transition metal catalysts toward each product of CO_2RR have been the subject of many theoretical and experimental studies. As previously mentioned, Cu and Cu-based catalysts are capable of converting CO_2 to most of the products including CO and HCOOH as well as CH_4, C_2H_4, CH_3OH and C_2H_5OH. In this context, there have been some other transition metals that showed activity

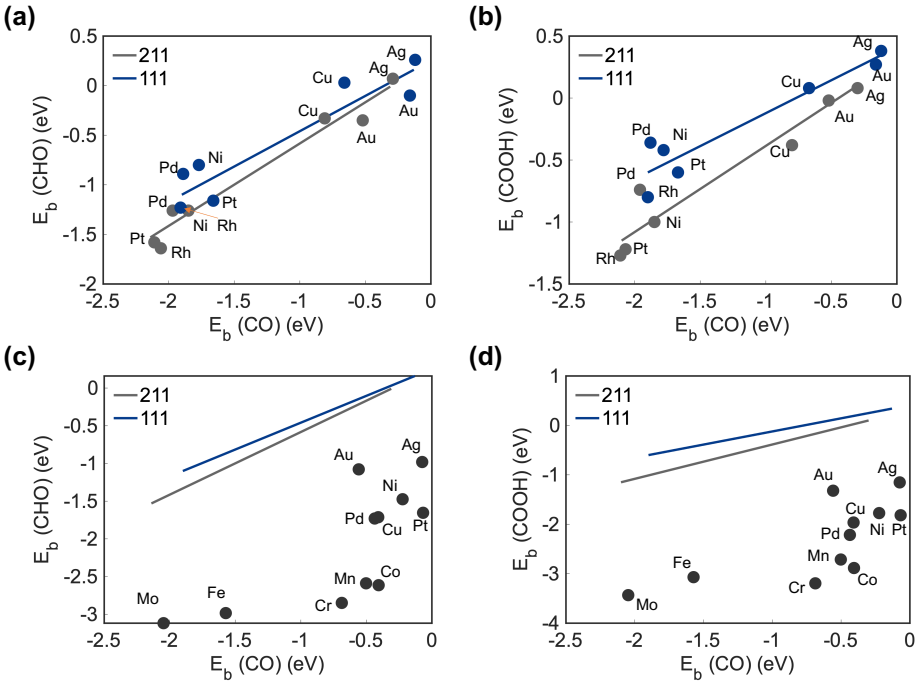

Figure 3.1: Linear scaling relationship between a: CO and CHO and b: CO and COOH intermediates on the surface of the metallic catalysts. Adapted with permission from reference number [58]. **c**, Scaling relationship between two identical intermediates as **a**, CHO and CO for $TM_3(HAB)_2$ MOFs with different TMs as metal centers. HAB = Hexaaminobenzene. **c**, Scaling relationship between COOH and CO for $TM_3(HAB)_2$-MOFs. The lines in **c** and **d** are the same lines from LSR between TMs in **a** and **b** for better comparison.

towards formate such as Pb and Sn, or CO such as Au and Ag [47]. As previously mentioned, the selectivity on the surface of a MOF could change compared to the pristine metal, due to downsizing of the catalytic size and structural enhancement. However, the reported products for MOF catalysts, do not differ from the printing metal in most of the cases. For instance, in multiple studies on MOF electrocatalysis, Zn-imidazolate MOF (ZIF-8) showed 65% FE towards CO, Co-ZIF-67 higher activity towards H_2 production rather than CO_2RR and Cu-based MOFs such as Cu-BTC selectively convert CO_2 into different products, including CH_3OH, C_2H_5OH, $C_2H_2O_4$ and CH_4 as well as CO [59, 60].

To experimentally investigate the effect of metal centres, Fig. 3.2 shows the performance of Ni/CoMOF [CoNi(μ_3-tp)$_2$(μ_2-pyz)$_2$] (tp = terephthalic acid and pyz = pyrazine) for CO_2RR. The MOF was synthesized following the synthesis procedure reported in [61]. 1 mmol of $Co(NO_3)_2.6H_2O$ and $Ni(NO_3)_2.6H_2O$ were combined with a 2 mmol of terephthalic acid and pyrazine in 14 mL of water. The mixture was then maintained at 200řC for 48 hours and subsequently cooled to room temperature at a rate of 5řC per hour. The scanning electron microscopy (SEM) image of the resulting crystals is shown in Fig. 3.2a. The synthesized MOF shows rod morphology with a diameter ranging between 1.8 and 2 μm and a length of 40 to 60 μm. As investigated with Energy Dispersive X-ray Spectroscopy (EDS) mapping, Ni/CoMOF crystallizes homogeneously, containing Co, Ni, C, N, and O from the organic linker (Fig. 3.2b,c). In terms of electrochemical performance, Co- and Ni-based MOFs have been separately investigated as electrocatalysts, showing superior activity for HER rather than CO_2RR [62]. Our results further confirm that their synergetic effect could also hinder CO_2 reduction reaction. The bi-metallic MOF shows almost 92% FE towards H_2 with small traces of CH_4 and C_2H_4 (FE$\ll$1). The measurements were carried out at a potential of -1.6 V vs. Ag/AgCl and the average recorded current density -6.12 mA/cm^2 (Fig. 3.2e). Whereas, the distribution of product changed drastically in the case of Cu_3(HHTP)$_2$ (HHTP = 2,3,6,7,10,11-hexahydroxytriphenylene) MOF at the same potential and electrolyte. Cu-HHTP is considered to be a 2D MOF, synthesized for the first time by Yaghi et al. [63] through the reaction of Cu^2+ ions with a highly conjugated HHTP linker (Fig. 3.2f). The Cu-O_4 nodes are periodically arranged in the honeycomb-like porous structure [63]. According to a study by Yu Zhang et al. [64], Cu-HHTP inhibits HER in the potential range of -0.7 to -1 V vs. RHE. It can be seen in Fig. 3.2h that the product analysis shows considerably low HER activity comparing to Co/Ni MOF. The total FE calculated for CO_2RR products is 47.3%. Having Cu surrounded by four oxygen atoms causes structural change and the generation of Cu_2O which may lead to the poor selectivity of Cu-HHTP catalyst towards one specific product [64].

Other transition metals as well as noble metals have also been investigated for electrocatalyzing CO_2 reduction reaction. It has been shown by Hod et. al that Iron-based MOF (i.e Fe-MOF-525) thinly deposited on tin oxide glass (FTO) could selectively convert CO_2 to CO with a 54% FE(CO) [65]. In another study, famous ZIF-8 with Zn metal centres (Zn(2-MeIm)$_2$), presented high catalytic activity towards CO_2 reduction to CO with Faradaic efficiency of 65% at 1.8 V versus Hg/Hg_2Cl_2 (SCE). $ReL(CO)_3Cl$ (L=2,2-bipyridine-5,5-dicarboxylic acid), into highly oriented SURMOF

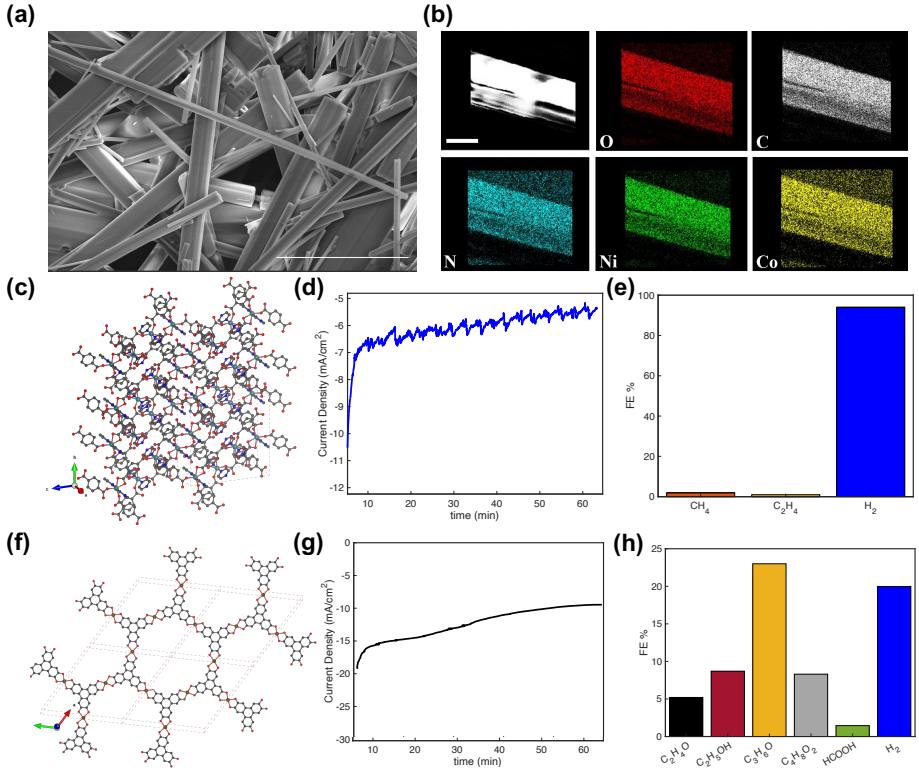

Figure 3.2: a, SEM image of Co-Ni-tp-pyz MOF. scale bar, 50 μm. **b**, EDS mapping of the as synthesized bi-metallic Co/Ni-MOF showing the presence of Co, Ni, O, N and C. **c**, 3D view Co-Ni-tp-pyz MOF structure. Colour-code: dark gray: C, dark blue: N, red: O, light gray: Ni, teal: Co. **d**, Current density recorded during CO_2 electrolysis **e**, Faradaic efficiency of the detected products on the surface of the Co/Ni-MOF at the potential of -1.6 V vs Ag/AgCl and in 1 M $KHCO_3$. **f** 3D view Cu-HHTP-MOF structure. Colour-code: dark gray: C, red: O, brown: Cu. **g**, Current density recorded for CO_2RR, **h** Faradaic efficiency of different products detected during one hour CO_2 electrolysis on the surface of Cu-HHTP MOF in 1 M $KHCO_3$ and at the potential of -1.6 V vs. Ag/AgCl.

thin films grown on FTO along the [001] direction displays excellent electrocatalytic performance with FE of 93% for reducing CO_2 to CO. Many studies to date have investigated the effect of the metal centre in MOFs on their catalytic performance; however, a conclusive and universal method to relate selectivity to the metal centre in MOFs is still needed.

In the quest for efficient and sustainable electrocatalysts for the CO_2RR, high-throughput computational screening has emerged as a vital technique. This method leverages the accuracy and precision of DFT calculations to elucidate the intricate adsorption and reaction mechanisms of various intermediates on MOF surfaces. This computational strategy not only accelerates the discovery of

high-performance MOFs, but also provides profound insights into the molecular interactions that drive CO_2RR activity. Given the expansive chemical diversity of potential MOF structures and compositions, high-throughput computational screening offers a systematic and efficient approach to pinpoint promising candidates. By concentrating on TMs incorporated within MOFs, we can investigate their distinct catalytic properties and potential to improve CO_2 reduction efficiency. In this regard, we focus on 2D ($(TMs)_3(HAB)_2$) MOFs as examples. To effectively evaluate the catalytic performance of these MOFs, it is crucial to consider key criteria such as Gibbs free energy, adsorption energies, and overpotential. These parameters provide comprehensive insights into the thermodynamics and kinetics of the CO_2 reduction reaction, guiding the identification of the most promising electrocatalysts.

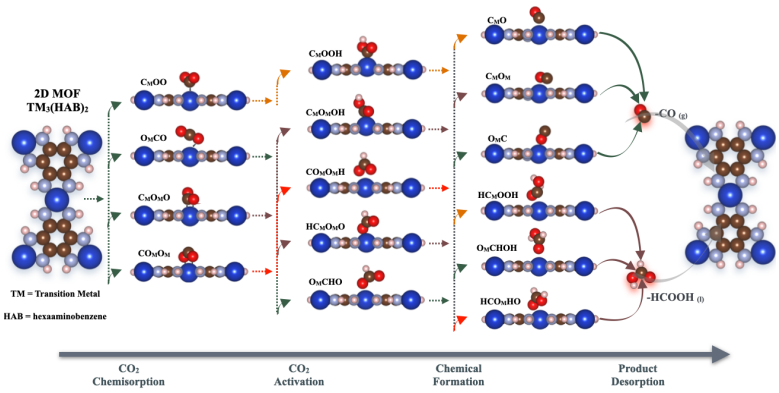

Figure 3.3: The potential intermediates involved in CO_2 reduction reaction (CO_2RR) on a 2D metal-organic framework (MOF) represented as $(TM)_3(HAB)_2$. The process encompasses four primary steps: chemisorption of CO_2, activation of CO_2, formation of chemical bonds, and desorption of the final product. For clarity, the protons and electrons ($H^+ + e^-$) in the reactions are not shown. The symbols 'g' and 'l' denote the gas and liquid phases, respectively. The colors indicate the following atoms: brown for carbon, light pink for hydrogen, light blue for nitrogen, red for oxygen, and blue for transition metal atoms.

In order to understand the electrocatalytic behaviour of TMs-MOFs, analysing the initial step of gaseous reactant adsorption on the catalyst surfaces is required. This step is crucial in determining the catalytic mechanism and activity. CO_2RR involves four primary reactions, namely CO_2 chemisorption, activation, product formation, and desorption, as depicted in Fig. 3.3. Identifying the relationship between catalytic performance and relevant intrinsic descriptors is crucial for developing a theoretical framework to screen the most effective catalysts from a wide array of 2D $TM_3(HAB)_2$ candidates. While overpotential (η) is commonly used to measure catalytic performance [66, 67], finding a predictive descriptor can significantly streamline the catalyst screening process. This study investigates the relationship between the overpotential of the CO_2 reduction reaction (η^{CO}) and the Gibbs free energies of $\Delta G_{*CO} - \Delta G_{*COOH}$, since the adsorption of *COOH and *CO significantly influences reaction pathways. Fig. 3.4(b) illustrates volcano-curve relationships

for 2D $TM_3(HAB)_2$ MOF and 2D transition metal phthalocyanines (TM-Pc), where $Ni_3(HAB)_2$ (η^{CO} = 0.37 V) and Co-Pc (η^{CO} = 0.79 V) are positioned at the peak of the volcano-curve, respectively. Generally, 2D $TM_3(HAB)_2$ MOFs exhibit superior catalytic performance compared to TM-Pc. Notably, $Ni_3(HAB)_2$ emerges as the most efficient catalyst for CO_2 reduction among these transition metals. Moreover, most $TM_3(HAB)_2$ demonstrate better CO_2 reduction catalytic activity than noble metals like Ag (211) and Au (211) surfaces [68, 69], which are widely explored and currently considered state-of-the-art catalysts for CO_2 reduction. Therefore, 2D $TM_3(HAB)_2$ MOFs represent a promising class of catalysts with high activity, potentially replacing noble-metal catalysts.

While the binding energy or Gibbs free energy has been used to establish volcano-curve relationships, identifying an intrinsic descriptor with predictive capabilities, independent of additional time-consuming DFT calculations, is more advantageous for selecting top catalysts from a wide range of materials. Recently, descriptors such as the d/p-band center [70, 71], and e_g and t_{2g} occupancy [72, 73] have been applied to explain the catalytic performance in oxygen reduction/evolution reaction and hydrogen evolution reaction for TMs-based catalysts. However, limited studies have explored the use of $TM_3(HAB)_2$ MOFs for the more complex CO_2RR. To build a volcano-curve relationship with the overpotential (η^{CO}) in $TM_3(HAB)_2$, we have identified a simple intrinsic descriptor (φ), which is defined as:

$$\varphi = \frac{\theta_d}{r_M \times n} \tag{3.11}$$

where, θ_d denotes the number of d electrons, r_M is the atomic radius and n is the periodic number of the transition metals (See Table 3.2). A positive correlation exists between this descriptor and the adsorption energy of TM intermediates. Consequently, this descriptor φ, which correlates with the adsorption of intermediates, captures the intrinsic characteristics of $TM_3(HAB)_2$, providing meaningful physical insight. By employing this intrinsic descriptor, we can not only predict the most effective catalysts but also clearly differentiate the catalytic mechanisms for 2D TM-based MOFs. Fig. 3.4c illustrates four distinct zones, each corresponding to a different reaction mechanism:

- **Zone 1 with** $\varphi < 1.00$: CO_2 reduction to CO occurs via Path 1, involving $(Ti/V/Cr)_3(HAB)_2$ catalysts;
- **Zone 2 with** $1.00 < \varphi < 2.00$: Path 2 is favored for CO_2 reduction on Mn, Fe, Co, and $(Ni)_3(HAB)_2$;
- **Zone 3 with** $2.00 < \varphi < 2.30$: CO_2 reduction follows Path 3 on $(Cu)_3(HAB)_2$;
- **Zone 4 with** $\varphi > 2.30$: CO_2 reduction proceeds via Path 4 on $(Zn)_3(HAB)_2$.

Additionally, formic acid represents a viable alternative product that competes with CO in the electrocatalytic CO_2RR. To explore this, we explored the competition between HCOOH and CO as products in CO_2RR 2D $TM_3(HAB)_2$ catalysts under uniform conditions. The pathway observed on 2D $TM_3(HAB)_2$ for this reaction

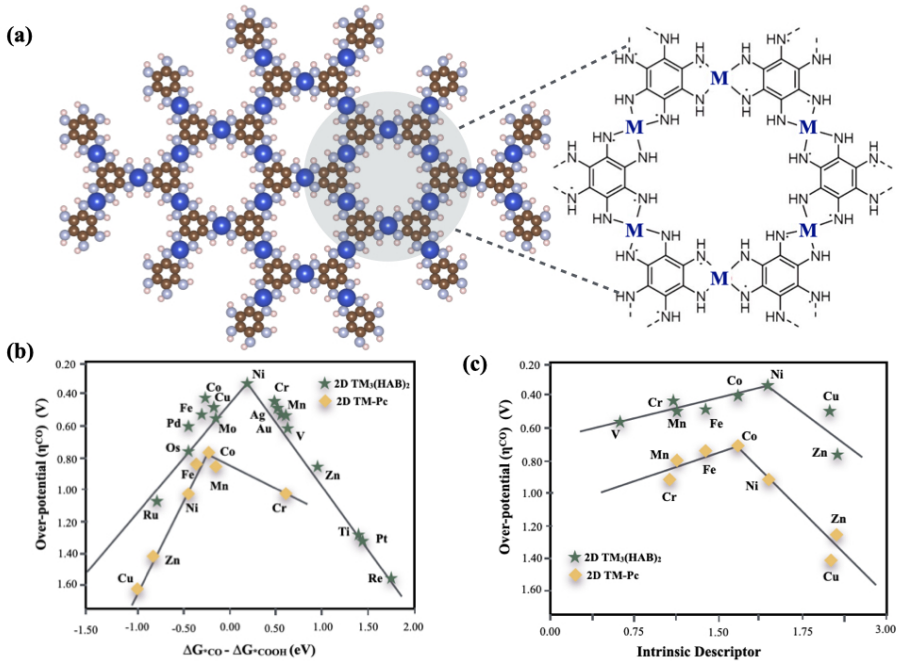

Figure 3.4: (a) Structural illustration of the 2D transition metal (TM) hexaiminobenzene (HAB) framework. (b) Overpotential of CO (η_{CO}) as a function of free energy difference between ΔG_{CO} and ΔG_{COOH} for various 2D transition metal frameworks. (c) Overpotential of CO (η_{CO}) plotted against the intrinsic descriptor for 2D TMs-HAB and TMs-Pc.

involves successive steps: $CO_2 \rightarrow {}^*CO_2 \rightarrow {}^*OCHO \rightarrow {}^*OCHOH \rightarrow HCOOH_{(l)}$. Optimal electrocatalysts with high selectivity typically exhibit lower overpotentials for CO compared to alternative products. Accordingly, we plotted the overpotential of CO (η^{CO}) against that of HCOOH (η^{HCOOH}) to analyze the dominance of each product in CO_2RR. Fig. 3.5a illustrates that most 2D $TM_3(HAB)_2$ catalysts are situated in the CO-dominated zone ($\eta^{CO} < \eta^{HCOOH}$), expect three $Rh_3(HAB)_2$, $Ru_3(HAB)_2$, and $Pt_3(HAB)_2$ which favor HCOOH production. Furthermore, hydrogen (H_2) competes also with CO in CO_2RR due to its similar thermodynamic potential [74]. To predict the competition between CO_2RR and the hydrogen evolution reaction on 2D $TM_3(HAB)_2$, the computed overpotential of HER (η^{H_2}) was evaluated alongside that of CO_2RR (η^{CO}). As shown in Fig. 3.5b, 2D $(TM)_3(HAB)_2$ catalysts with TM = Co, Fe, Ni, Mn, Au, and Ag predominantly occupy the CO-dominated zone, suggesting their potential to effectively suppress HER. Thus, these advanced 2D $TM_3(HAB)_2$ MOFs exhibit promising electrocatalytic characteristics as catalysts with heightened activity and selectivity for CO_2RR aimed at CO production.

Table 3.2: Number of d-electrons (θ_d), periodic number (n), atomic radius (r_M), and calculated intrinsic descriptor (φ) of transition metals.

TMs	θ_d	n	r_{TM}/Å	φ
Cu	10	3	1.45	2.30
Cr	5	3	1.66	1.00
Co	7	3	1.52	1.54
Fe	6	3	1.56	1.28
Ni	8	3	1.49	1.79
Ti	2	3	1.76	0.38
V	3	3	1.71	0.58
Mn	5	3	1.61	1.04
Re	5	5	1.88	0.53
Pt	9	5	1.77	1.02
Zn	10	3	1.42	2.35
Mo	5	4	1.90	0.66
Ru	7	4	1.78	0.98
Rh	8	4	1.73	1.16
Pd	10	4	1.69	1.48
Ag	10	4	1.65	1.52
Au	10	5	1.74	1.15

3.3.2. ORGANIC LINKERS

The versatility in organic linker design not only influences the structural and electronic properties of MOFs, but also opens pathways for innovative modifications to enhance their functionality. One such modification is lowering the dimensionality of MOFs, resulting in two-dimensional (2D) MOFs. In the design process of MOFs, the size, position and role of the organic linker could have a remarkable influence on the structure, electrical conductivity and thus electrocatalytic performance. In this regard, a new generation of MOFs, constructed using monomers based on benzene benzoquinone, triphenylene, coronene, phthalocyanine, and dibenzo[g,p]chrysene, has shown strong in-plane conjugation and weak out-of-plane π-π stacking. This has led to the formation of 2D crystal structures with a high surface area-to-volume ratio, making them ideal candidates for electrocatalytic applications. As a result, the topological structures of MOFs can be feasibly tailored by ligand design, resulting in diverse structures, pore geometries (e.g., triangle, square, and hexagonal), pore sizes (from non-porous to 2 nm in diameter), and surface areas [75]. These layer-stacked MOFs characterized by high in-plane conjugation and weak out-of-plane stacking, offer promising opportunities for electrocatalysis [76]. Research on 2D MOFs involves integrating theoretical molecular design, synthetic chemistry, and functional applications. Although intensive efforts have been dedicated to the preparation of new 2D MOFs, their exploration for electrochemical applications has only gained scientific attention in recent years [77]. .

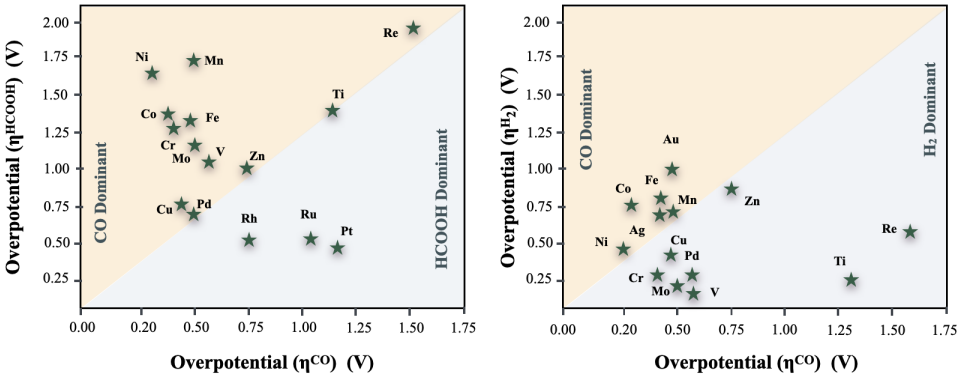

Figure 3.5: Correlation between CO overpotential (η_{CO}) and the overpotentials of HCOOH (η_{HCOOH}) and H_2 (η_{H_2}).

Despite the fact that 2D MOFs have recently shown great promise in hydrogen evolution reactions, oxygen reduction and evolution reactions, and supercapacitors, their applicability in electrochemical reactions particularly CO_2RR remains relatively unexplored. As an example, theoretical and experimental results from another study indicate $Cu_3(HHTQ)_2$ with electron-deficient, but nitrogen-rich TQ cores showing high selectivity toward CH_3OH with FE up to 53.6% [78].

3.3.3. Coordination Environments

One classification of the organic linkers could be done based on their functional groups such as carbonyl, oxygen, sulfur, or nitrogen. In the context of catalytic activity, the effect of the chemical structure of the organic linker might be better explained as the coordination environment of the metal active sites [79]. The coordination and chemical environment around the metallic active sites affect the CO_2 adsorption and activation mode, as well as the subsequent reaction pathway. Moreover, charge densities and energy levels of d-orbitals for metal centre could alter the formation energy and binding strength of key intermediates for reaction pathways of different products and therefore, modulating the selectivity of the CO_2RR [80]. For instance, in the case of Cu-HHTP, having Cu surrounded by four oxygen atoms causes structural change and the generation of Cu_2O which may lead to the poor selectivity of Cu-HHTP catalyst [64] (Fig. 3.2h). Linker engineering is considered as a novel approach to control the coordination environment of catalytic cites in MOFs towards enhanced selectivity in CO_2RR. In this regard, the potential of tuning organic ligands in MOFs to develop more efficient and selective catalysts for CO_2 reduction was studied on Zn-based MOFs (Fig. 3.6a). CALF-20 ($Zn_2(Tz)_2Ox$] Tz = 1,2,4-triazolate, Ox = oxalate)-MOF achieved a CO FE of 94.5% and a partial current density of -32.8 mA/cm^2 (Fig. 3.6b). Theoretical and experimental results indicate that superior performance of CALF-20 over ZIF-8 (Zn-zeolitic imidazolate framework) stems from its triazolate ligands, which provide multiple sp2 C active sites (Fig. 3.6c),

increased CO_2 uptake, and improved charge transfer facilitated by its oxalate linker (Fig. 3.6d) [81]. In a recent study, Wang et al. [80] showed that by changing the coordination environment of copper from Cu-I-S to Cu-N-S, in the Cu-CPs structure, high selectivity towards C_2H_4 could be achieved, compared to the dominant HCOOH production [82]. The highly electroactive Cu3d orbitals with weak CuCu interactions in CuNS ensure efficient conversion and high selectivity for the C_{2+} pathway. In contrast, the strong CuCu interactions in CuIS make CC coupling difficult, leading to high selectivity for C_1 pathways [80].

Organic functional groups can be classified into four main categories based on their chemical and structural characteristics: carbonyl-based functions, nitrogen-based functions, oxygen-based functions, and sulfur-based functions. Therefore, the coordination environment of the metal could consist of N, O, and S. Due to the limited number of studies on the effect of each p-block element on CO_{22}RR selectivity performance, it is difficult to categorize these elements based on their product preference [79, 83]. Numerous studies indicate that M-N_x moieties, for instance, are crucial for CO_2RR, but performance varies significantly among TM-N based MOFs with the same or different metals. Recently, Cu(I)-N_2 in graphene and various has been synthesized, showing poor or unknown CO_2 reduction activity. In contrast, unsaturated Ni-N_x and Co-N_x (where x<4) in carbon exhibit excellent performance in the production of CO. Notably, CoN_4 and Co-N_5 also show high CO production selectivity [84]. Moreover, as mentioned in the case of Wang et al., adding sulfur to the coordination environment of copper has been show to improve the selectivity of the catalyst towards formate/formic acid rather than CO [85].

In addition to the nature of the coordination environment, coordination number of the metallic atom is also one of the parameters that affect the performance of MOFs. Dense frameworks made from rigid, highly connected building blocks (i.e. metal ions and ligands) typically exhibit high stability due to their strong resistance to partial lattice collapse. In this regard, the fundamental principle for creating stable MOFs involves utilizing strong coordination bonds, a high coordination number of metal ions, the inertness of the metal, and other factors[86]. Although, at the same time, as coordination chemistry-related studies have shown, the catalytic activity is related to the existence of sites with low-energy electronic fluctuations. That means, in the case of TMs, since the maximum electronic fluctuations take place at high-coordination metal sites, having a lower coordination number could potentially lead to higher activity [87]. The more empty spaces available around the catalytic centre, the higher the chance of reactant adsorption and reaction occurrence. In this regard, one study on Co-based single-atom catalysis demonstrates that the catalytic specific activity of Co-N_x depends on the coordination number of the single atomic Co sites. It was found that the Co-N_2 catalyst, which has the lowest coordination number, shows the highest specific activity [88]. To conclude with the discussed example of Cu-HHTP (Fig. 3.2f), having a lower coordination number, would help with improving the activity. However, the stability of the catalytic centres might be problematic in the case of structurally sensitive reactions i.e CO_2RR. Therefore, as long as the stability of the low-coordination MOF is assured in the reaction media, the higher activity of the catalyst is expected [89, 90].

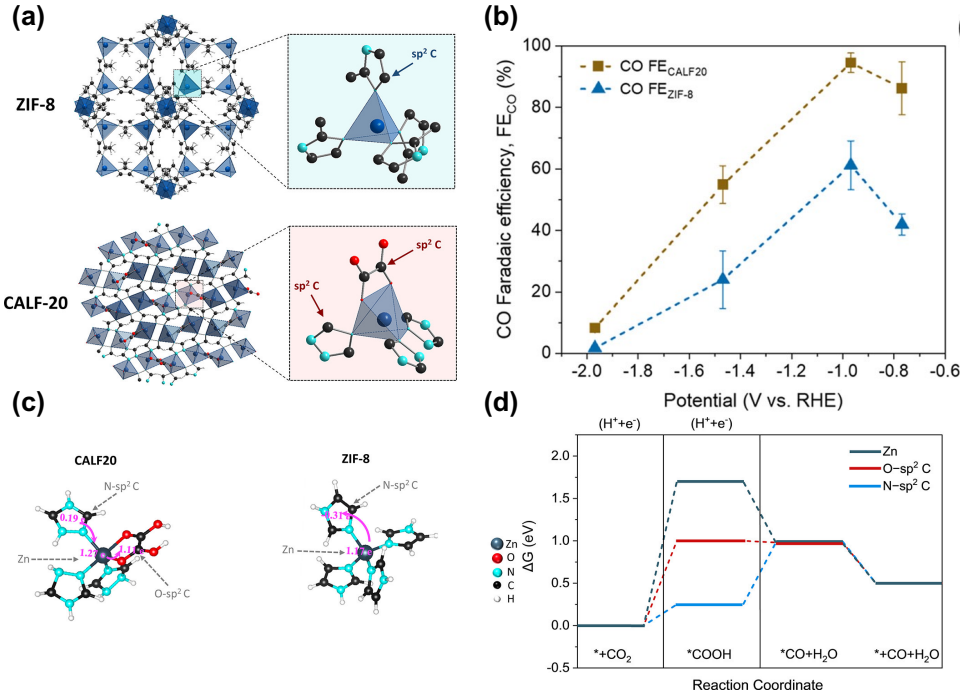

Figure 3.6: **a**, Schematic illustration of the crystal structure of ZIF-8 and CALF-20, **b**, CO Faradaic efficiencies in different potentials using ZIF-8 and CALF-20 catalysts. **c**, Truncated model structures of CALF-20 and ZIF-8 labeled with different possible active sites. The purple arrows indicate charge transfer from azolates to Zn(II), and to bidentate oxalate ligands in CALF-20, from Zn(II) to imidazolate. Bader charge indicates CALF-20 have stronger charge transfer: Zn (II, 1.27 e) in CALF-20 loses more electron than Zn (1.17 e) in ZIF-8. **d**, Calculated free energy diagram for electrochemical reduction of CO_2 to CO over CALF-20 at U = 0.00 V vs RHE [81]

.

Moreover, while metal centers in MOFs are often seen as the active sites for electrocatalysis, some research suggests that the carbons in the ligands can also play a crucial role. By modifying the electron density of the ligand with electron-donating or electron-withdrawing groups, the electrocatalytic behavior can be significantly altered. For example, in ZIF-8, the sp2 carbons of the imidazolate linker are proposed as active sites due to the fully occupied Zn^{2+} 3d orbital. enhanced CO production efficiency in CO_2RR by doping the ZIF-8 ligand with 1,10-phenanthroline was reported, increasing the Faradaic efficiency from 70% to 90.57%. DFT calculations in the same study indicated that the electron transfer from phenanthroline molecules to adjacent sp2 carbons facilitated CO_2 activation, leading to the formation of the *COOH intermediate [91]. To conclude, as theoretical research suggests, p-block elements, could contribute to CO_2 bond formation on electrocatalyst surfaces, potentially disrupting the linear scaling rela-tionships observed for transition metals. By choosing different organic

linker with different moieties, or in some cases changing the chemical structure of the existing linker, regulation of the selectivity could be achieved.

3.4. CONCLUSION

Metal-organic frameworks have quickly emerged as promising alternatives to traditional catalysts for the electrocatalysis of carbon dioxide. CO_2 can be transformed into various useful products, but the selectivity and efficiency of this conversion largely depend on the active sites within the catalyst material. In order to step forward towards industrializing the CO_2RR technology, it is important to improve the selectivity of the catalyst to avoid large expenses of product separation process. Targeting specific products is a valid strategy which happens through precise design of the catalyst. In MOFs, metal centers typically serve as catalytic active sites, with ligands aiding in the conversion process. As the size of the catalyst is been lowered to a single atom in MOFs, the selectivity of these materials for CO_2RR towards small C_1 products such as CO and HCOOH, has improved through hindering the C-C coupling. Controlling size of the catalytic active sites is one of the easiest strategies to break the linear scalling relationship existing among three key intermediates of CO_2RR, namely *CHO, CO and *HCOO. This linear scaling relationship is the main cause of poor selectivity of the metallic catalysts for CO_2RR. In addition to the size factor, tunability of MOFs allows us to enhance the selectivity as well as activity through strategies such as modifying the ligand, adding modifiers to the structure as well as post treatment of MOFs with the aim of alterign their electronic structure. The porous structure of MOFs aids in mass transport and provides a high surface area with dispersed metal nodes, increasing the number of active sites.

Despite significant improvements in the CO_2RR performance by MOF-based electrocatalysts, practical application challenges remain. Issues like limited conductivity and chemical stability. Moreover, there is a lack of systematic design studies, especially those using computational methods.Conductivity and stability are particularly problematic for MOFs, especially at the very negative potentials commonly used in CO_2RR, which are more negative than the reduction potential of many metals used in MOF preparation. Research indicates that the inherent conductivity of MOFs can be improved by combining them with conductive materials or anchoring them on conductive supports. However, many MOFs are unstable during the CO_2 reduction process in aqueous electrolytes at highly negative potentials, leading to the formation of metal and metal oxide nanoparticles (NPs) that act as electrocatalysts for CO_2RR. Therefore, improving the stability of MOF-based catalysts is a crucial issue that needs to be addressed. As discussed, one of the strategies to overcome this issue is coordination enviorenment engineering through linker selection.

In this manuscript, the importance of CO_2RR and a throughout study of catalytic process and what is expected from a catalyst material in this technology was discussed. From the perspective of targeting one specific product among all possible products, the theory behind the poor selectivity of conventional transition metal based catalyst materials, was fully explained. It is well demonstrated that metal

organic frameworks due to their complex structure and their atomically dispersed active catalytic sites could drastically improve the selectivity of CO_2RR. Through a DFT study on binding energies of CO_2RR key intermediates, We showed that different TMs in the structure of a HAB-based MOF could perform beyond LSR. However, there are different design strategies regarding synthesizing MOFs for various applications that need to be taken into account. In terms of designing a catalyst for CO_2RR, we showed that the preference of the TM towards a specific CO_2RR product does not necessarily change in the format of a MOF but the selectivity changes in comparison with the pristine TM. Furthermore, given high tunability of MOFs in regards to corrdination enviornment and linker selection was discussed as an important strategy to improve the catalytic performance of a MOF. It is shown that the coordination number and environment of the metallic center could change the activity, reaction pathway and stability. Structural modification and post-treatment of MOFs were also discussed in this manuscript for further improving the catalytic performance of MOFs towards CO_2RR. Eventually, determining the connection between catalytic performance and relevant intrinsic descriptors was fully investigated for a series of 2D Hexaaminobenzen and Phthalocyanine-based MOFs. It is more beneficial to identify an intrinsic descriptor with predictive capabilities that do not rely on additional time-consuming DFT calculations for selecting the best catalysts from a broad range of materials. Using this intrinsic descriptor, we could both predict the most effective catalysts and clearly distinguish the catalytic mechanisms for 2D TM-based MOFs.

3.5. CHALLENGES, OPPORTUNITIES AND FUTURE OUTLOOK

It is important to admit that despite numerous attempts, still application of MOFs in CO_2RR needs more and more systematic studies and research. Particularly in terms of rational MOF design, this involves adjusting synthesis parameters and procedures and improving electrical conductivity and chemical stability. In a more general perspective, given the structural tunability of MOFs, research opportunities for designing a suitable electrocatalyst should not be ignored. As an example, the scarcity of MOFs based on the early second- and third-row transition metals is visible in MOF research and can be attributed to a variety of synthetic challenges. Strong coordination of ligands to second-row metals leads to slow kinetics of ligand exchange, which inhibits the reversible coordination necessary to form crystalline frameworks. Second, these metals tend to possess higher oxidation states, higher coordination numbers, and larger oxophilicities than their first-row counterparts, which can lead to the formation of metaloxo species under typical solvothermal synthesis conditions and complicate the synthesis of isostructural frameworks. Finally, common precursors that can be found and used easily for the synthesis of first-row transition metal-based MOFs are not available or behave differently for second and third-row transition metals. Altogether, although many theoretical studies have shown the potential of these metals for CO_2RR, these challenges underscore the need for new synthetic strategies to develop MOFs based on second- and third-row metal ions. This is the same case for MOFs based on Nobel metals such as Ru, which suffer from chemical stability.

Moreover, in regards to Cu-based MOFs as promising candidates for electrochemical CO_2 reduction, further development, potentially enhancing their performance and selectivity is needed. The instability of these MOFs severely restricts their use for large-scale electrochemical CO_2 reduction. Thus, enhancing their resilience through an organic linker and their coordination environment can stabilize copper units. Another important aspect is understanding their properties during CO_2 reduction via in situ methods is crucial for improving stability and performance. Combination of theoretical and experimental studies can elucidate CO_2RR mechanisms, whereas improving energy efficiency requires addressing overpotentials and low conductivity.

REFERENCES

[1] S. Chu, Y. Cui, and N. Liu. "The path towards sustainable energy". In: *Nature materials* 16.1 (2017), pp. 16–22.

[2] Z. Sun, T. Ma, H. Tao, Q. Fan, and B. Han. "Fundamentals and challenges of electrochemical CO_2 reduction using two-dimensional materials". In: *Chem* 3.4 (2017), pp. 560–587.

[3] S. J. Davis, K. Caldeira, and H. D. Matthews. "Future CO_2 emissions and climate change from existing energy infrastructure". In: *Science* 329.5997 (2010), pp. 1330–1333.

[4] J. Wu, Y. Huang, W. Ye, and Y. Li. "CO_2 reduction: from the electrochemical to photochemical approach". In: *Advanced Science* 4.11 (2017), p. 1700194.

[5] L. Zhang, I. Merino-Garcia, J. Albo, and C. M. Sánchez-Sánchez. "Electrochemical CO_2 reduction reaction on cost-effective oxide-derived copper and transition metal–nitrogen–carbon catalysts". In: *Current Opinion in Electrochemistry* 23 (2020), pp. 65–73.

[6] T. N. Nguyen, M. Salehi, Q. V. Le, A. Seifitokaldani, and C. T. Dinh. "Fundamentals of electrochemical CO_2 reduction on single-metal-atom catalysts". In: *ACS Catalysis* 10.17 (2020), pp. 10068–10095.

[7] A. Bagger, W. Ju, A. S. Varela, P. Strasser, and J. Rossmeisl. "Electrochemical CO_2 reduction: a classification problem". In: *ChemPhysChem* 18.22 (2017), pp. 3266–3273.

[8] P. Yaashikaa, P. S. Kumar, S. J. Varjani, and A. Saravanan. "A review on photochemical, biochemical and electrochemical transformation of CO_2 into value-added products". In: *Journal of CO_2 Utilization* 33 (2019), pp. 131–147.

[9] R.-P. Ye, J. Ding, W. Gong, M. D. Argyle, Q. Zhong, Y. Wang, C. K. Russell, Z. Xu, A. G. Russell, Q. Li, *et al.* "CO_2 hydrogenation to high-value products via heterogeneous catalysis". In: *Nature communications* 10.1 (2019), p. 5698.

[10] W. Zhang, Z. Chen, Y.-X. Jiang, L.-L. Liao, W. Wang, J.-H. Ye, and D.-G. Yu. "Arylcarboxylation of unactivated alkenes with CO_2 via visible-light photoredox catalysis". In: *Nature Communications* 14.1 (2023), p. 3529.

[11] A. D. Kamkeng, M. Wang, J. Hu, W. Du, and F. Qian. "Transformation technologies for CO_2 utilisation: Current status, challenges and future prospects". In: *Chemical Engineering Journal* 409 (2021), p. 128138.

[12] K. Li, B. Peng, and T. Peng. "Recent advances in heterogeneous photocatalytic CO_2 conversion to solar fuels". In: *Acs Catalysis* 6.11 (2016), pp. 7485–7527.

[13] M. Ong, S. Nomanbhay, F. Kusumo, and P. Show. “Application of microwave plasma technology to convert carbon dioxide (CO_2) into high value products: A review”. In: *Journal of Cleaner Production* 336 (2022), p. 130447.

[14] D. R. Kauffman, J. Thakkar, R. Siva, C. Matranga, P. R. Ohodnicki, C. Zeng, and R. Jin. “Efficient electrochemical CO_2 conversion powered by renewable energy”. In: *ACS applied materials & interfaces* 7.28 (2015), pp. 15626–15632.

[15] T. Zheng, K. Jiang, and H. Wang. “Recent advances in electrochemical CO_2-to-CO conversion on heterogeneous catalysts”. In: *Advanced materials* 30.48 (2018), p. 1802066.

[16] B. Kumar, J. P. Brian, V. Atla, S. Kumari, K. A. Bertram, R. T. White, and J. M. Spurgeon. “New trends in the development of heterogeneous catalysts for electrochemical CO_2 reduction”. In: *Catalysis Today* 270 (2016), pp. 19–30.

[17] C. Long, X. Li, J. Guo, Y. Shi, S. Liu, and Z. Tang. “Electrochemical reduction of CO_2 over heterogeneous catalysts in aqueous solution: recent progress and perspectives”. In: *Small Methods* 3.3 (2019), p. 1800369.

[18] C. G. Okoye-Chine, K. Otun, N. Shiba, C. Rashama, S. N. Ugwu, H. Onyeaka, and C. T. Okeke. “Conversion of carbon dioxide into fuelsA review”. In: *Journal of CO_2 Utilization* 62 (2022), p. 102099.

[19] Q. Lu and F. Jiao. “Electrochemical CO_2 reduction: Electrocatalyst, reaction mechanism, and process engineering”. In: *Nano Energy* 29 (2016), pp. 439–456.

[20] S.-L. Hou, J. Dong, and B. Zhao. “Formation of CX Bonds in CO_2 Chemical Fixation Catalyzed by Metal- Organic Frameworks”. In: *Advanced Materials* 32.3 (2020), p. 1806163.

[21] R. Kortlever, J. Shen, K. J. P. Schouten, F. Calle-Vallejo, and M. T. Koper. “Catalysts and reaction pathways for the electrochemical reduction of carbon dioxide”. In: *The journal of physical chemistry letters* 6.20 (2015), pp. 4073–4082.

[22] S. Zhang, Q. Fan, R. Xia, and T. J. Meyer. “CO_2 reduction: from homogeneous to heterogeneous electrocatalysis”. In: *Accounts of chemical research* 53.1 (2020), pp. 255–264.

[23] Y. Zou and S. Wang. “An investigation of active sites for electrochemical CO_2 reduction reactions: from in situ characterization to rational design”. In: *Advanced Science* 8.9 (2021), p. 2003579.

[24] F. Li, D. R. MacFarlane, and J. Zhang. “Recent advances in the nanoengineering of electrocatalysts for CO 2 reduction”. In: *Nanoscale* 10.14 (2018), pp. 6235–6260.

[25] S. Jin, Z. Hao, K. Zhang, Z. Yan, and J. Chen. “Advances and challenges for the electrochemical reduction of CO_2 to CO: from fundamentals to industrialization”. In: *Angewandte Chemie* 133.38 (2021), pp. 20795–20816.

[26] P. Saha, S. Amanullah, and A. Dey. “Selectivity in electrochemical CO_2 reduction”. In: *Accounts of chemical research* 55.2 (2022), pp. 134–144.

[27] S. Gorthy, S. Verma, N. Sinha, S. Shetty, H. Nguyen, and M. Neurock. "Theoretical Insights into the Effects of KOH Concentration and the Role of OH–in the Electrocatalytic Reduction of CO_2 on Au". In: *ACS Catalysis* 13.19 (2023), pp. 12924–12940.

[28] A. A. Peterson, F. Abild-Pedersen, F. Studt, J. Rossmeisl, and J. K. Nørskov. "How copper catalyzes the electroreduction of carbon dioxide into hydrocarbon fuels". In: *Energy & Environmental Science* 3.9 (2010), pp. 1311–1315.

[29] D. Voiry, H. S. Shin, K. P. Loh, and M. Chhowalla. "Low-dimensional catalysts for hydrogen evolution and CO_2 reduction". In: *Nature Reviews Chemistry* 2.1 (2018), p. 0105.

[30] J. Pérez-Ramírez and N. López. "Strategies to break linear scaling relationships". In: *Nature Catalysis* 2.11 (2019), pp. 971–976.

[31] T. Zhan, Y. Zou, Y. Yang, X. Ma, Z. Zhang, and S. Xiang. "Two-dimensional Metal-organic Frameworks for Electrochemical CO_2 Reduction Reaction". In: *ChemCatChem* 14.3 (2022), e202101453.

[32] Y. Zhao, L. Zheng, D. Jiang, W. Xia, X. Xu, Y. Yamauchi, J. Ge, and J. Tang. "Nanoengineering metal–organic framework-based materials for use in electrochemical CO_2 reduction reactions". In: *Small* 17.16 (2021), p. 2006590.

[33] Y. Zhang, X. Zhang, Y. Zhu, B. Qian, A. M. Bond, and J. Zhang. "The Origin of the Electrocatalytic Activity for CO_2 Reduction Associated with Metal-Organic Frameworks". In: *ChemSusChem* 13.10 (2020), pp. 2552–2556.

[34] H. Zhang, J. Li, Q. Tan, L. Lu, Z. Wang, and G. Wu. "Metal–organic frameworks and their derived materials as electrocatalysts and photocatalysts for CO_2 reduction: Progress, challenges, and perspectives". In: *Chemistry–A European Journal* 24.69 (2018), pp. 18137–18157.

[35] H. Furukawa, K. E. Cordova, M. OKeeffe, and O. M. Yaghi. "The chemistry and applications of metal-organic frameworks". In: *Science* 341.6149 (2013), p. 1230444.

[36] H. B. Aiyappa, J. Masa, C. Andronescu, M. Muhler, R. A. Fischer, and W. Schuhmann. "MOFs for electrocatalysis: from serendipity to design strategies". In: *Small Methods* 3.8 (2019), p. 1800415.

[37] H. A. Hansen, J. B. Varley, A. A. Peterson, and J. K. Nørskov. "Understanding trends in the electrocatalytic activity of metals and enzymes for CO_2 reduction to CO". In: *The journal of physical chemistry letters* 4.3 (2013), pp. 388–392.

[38] P. Hirunsit. "Electroreduction of carbon dioxide to methane on copper, copper–silver, and copper–gold catalysts: a DFT study". In: *The Journal of Physical Chemistry C* 117.16 (2013), pp. 8262–8268.

[39] M. Karamad, H. A. Hansen, J. Rossmeisl, and J. K. Nørskov. "Mechanistic pathway in the electrochemical reduction of CO_2 on RuO2". In: *Acs Catalysis* 5.7 (2015), pp. 4075–4081.

[40] G.-L. Chai and Z.-X. Guo. “Highly effective sites and selectivity of nitrogen-doped graphene/CNT catalysts for CO 2 electrochemical reduction”. In: *Chemical Science* 7.2 (2016), pp. 1268–1275.

[41] J. Wu, R. M. Yadav, M. Liu, P. P. Sharma, C. S. Tiwary, L. Ma, X. Zou, X.-D. Zhou, B. I. Yakobson, J. Lou, *et al.* “Achieving highly efficient, selective, and stable CO_2 reduction on nitrogen-doped carbon nanotubes”. In: *ACS nano* 9.5 (2015), pp. 5364–5371.

[42] M. Karamad, V. Tripkovic, and J. Rossmeisl. “Intermetallic Alloys as CO Electroreduction Catalysts Role of Isolated Active Sites”. In: *ACS Catalysis* 4.7 (2014), pp. 2268–2273.

[43] L. Gong, D. Zhang, C.-Y. Lin, Y. Zhu, Y. Shen, J. Zhang, X. Han, L. Zhang, and Z. Xia. “Catalytic mechanisms and design principles for single-atom catalysts in highly efficient CO_2 conversion”. In: *Advanced Energy Materials* 9.44 (2019), p. 1902625.

[44] Y. Ouyang, L. Shi, X. Bai, Q. Li, and J. Wang. “Breaking scaling relations for efficient CO 2 electrochemical reduction through dual-atom catalysts”. In: *Chemical science* 11.7 (2020), pp. 1807–1813.

[45] P. Lobaccaro, M. R. Singh, E. L. Clark, Y. Kwon, A. T. Bell, and J. W. Ager. “Effects of temperature and gas–liquid mass transfer on the operation of small electrochemical cells for the quantitative evaluation of CO 2 reduction electrocatalysts”. In: *Physical Chemistry Chemical Physics* 18.38 (2016), pp. 26777–26785.

[46] A. R. Morrison, M. Ramdin, L. J. Van Der Broeke, W. De Jong, T. J. Vlugt, and R. Kortlever. “Surface Coverage as an Important Parameter for Predicting Selectivity Trends in Electrochemical CO_2 Reduction”. In: *The Journal of Physical Chemistry C* 126.29 (2022), pp. 11927–11936.

[47] Y. Y. Birdja, E. Pérez-Gallent, M. C. Figueiredo, A. J. Göttle, F. Calle-Vallejo, and M. T. Koper. “Advances and challenges in understanding the electrocatalytic conversion of carbon dioxide to fuels”. In: *Nature Energy* 4.9 (2019), pp. 732–745.

[48] G. L. De Gregorio, T. Burdyny, A. Loiudice, P. Iyengar, W. A. Smith, and R. Buonsanti. “Facet-dependent selectivity of Cu catalysts in electrochemical CO_2 reduction at commercially viable current densities”. In: *ACS catalysis* 10.9 (2020), pp. 4854–4862.

[49] A. Bagger, W. Ju, A. S. Varela, P. Strasser, and J. Rossmeisl. “Electrochemical CO_2 reduction: classifying Cu facets”. In: *Acs Catalysis* 9.9 (2019), pp. 7894–7899.

[50] Y.-Y. Liu, H.-L. Zhu, Z.-H. Zhao, N.-Y. Huang, P.-Q. Liao, and X.-M. Chen. “Insight into the Effect of the d-Orbital Energy of Copper Ions in Metal–Organic Frameworks on the Selectivity of Electroreduction of CO_2 to CH4”. In: *Acs Catalysis* 12.5 (2022), pp. 2749–2755.

[51] L. Majidi, A. Ahmadiparidari, N. Shan, S. N. Misal, K. Kumar, Z. Huang, S. Rastegar, Z. Hemmat, X. Zou, P. Zapol, *et al.* “2D copper tetrahydroxyquinone conductive metal-organic framework for selective CO_2 electrocatalysis at low overpotentials”. In: *Advanced Materials* 33.10 (2021), p. 2004393.

[52] S. M. Stratton, S. Zhang, and M. M. Montemore. “Addressing complexity in catalyst design: From volcanos and scaling to more sophisticated design strategies”. In: *Surface Science Reports* (2023), p. 100597.

[53] J. T. Feaster, C. Shi, E. R. Cave, T. Hatsukade, D. N. Abram, K. P. Kuhl, C. Hahn, J. K. Nørskov, and T. F. Jaramillo. “Understanding selectivity for the electrochemical reduction of carbon dioxide to formic acid and carbon monoxide on metal electrodes”. In: *Acs Catalysis* 7.7 (2017), pp. 4822–4827.

[54] F. Abild-Pedersen, J. Greeley, F. Studt, J. Rossmeisl, T. R. Munter, P. G. Moses, E. Skulason, T. Bligaard, and J. K. Nørskov. “Scaling Properties of Adsorption Energies for Hydrogen-Containing Molecules<? format?> on Transition-Metal Surfaces”. In: *Physical review letters* 99.1 (2007), p. 016105.

[55] T. Z. Gani and H. J. Kulik. “Understanding and Breaking Scaling Relations in Single-Site Catalysis: Methane to Methanol Conversion by Fe^{IV} = O”. In: *Acs Catalysis* 8.2 (2018), pp. 975–986.

[56] Y. Xu, M. Chu, F. Liu, X. Wang, Y. Liu, M. Cao, J. Gong, J. Luo, H. Lin, Y. Li, *et al.* “Revealing the correlation between catalytic selectivity and the local coordination environment of Pt single atom”. In: *Nano Letters* 20.9 (2020), pp. 6865–6872.

[57] B. Lu, Q. Liu, and S. Chen. “Electrocatalysis of single-atom sites: impacts of atomic coordination”. In: *Acs Catalysis* 10.14 (2020), pp. 7584–7618.

[58] X. Hong, K. Chan, C. Tsai, and J. K. Nørskov. “How doped MoS2 breaks transition-metal scaling relations for CO_2 electrochemical reduction”. In: *Acs Catalysis* 6.7 (2016), pp. 4428–4437.

[59] P. Shao, L. Yi, S. Chen, T. Zhou, and J. Zhang. “Metal-organic frameworks for electrochemical reduction of carbon dioxide: The role of metal centers”. In: *Journal of Energy Chemistry* 40 (2020), pp. 156–170.

[60] Y. Wang, P. Hou, Z. Wang, and P. Kang. “Zinc imidazolate metal–organic frameworks (ZIF-8) for electrochemical reduction of CO_2 to CO”. In: *ChemPhysChem* 18.22 (2017), pp. 3142–3147.

[61] H. Gholipour-Ranjbar, M. Soleimani, and H. R. Naderi. “Application of Ni/Co-based metal–organic frameworks (MOFs) as an advanced electrode material for supercapacitors”. In: *New Journal of Chemistry* 40.11 (2016), pp. 9187–9193.

[62] L.-Z. Wu, X.-Y. Zhou, P.-C. Zeng, J.-Y. Huang, M.-D. Zhang, and L. Qin. “Hydrothermal synthesis of Ni (II) or Co (II)-based MOF for electrocatalytic hydrogen evolution”. In: *Polyhedron* 225 (2022), p. 116035.

[63] M. Hmadeh, Z. Lu, Z. Liu, F. Gándara, H. Furukawa, S. Wan, V. Augustyn, R. Chang, L. Liao, F. Zhou, *et al.* "New porous crystals of extended metal-catecholates". In: *Chemistry of Materials* 24.18 (2012), pp. 3511–3513.

[64] Y. Zhang, L.-Z. Dong, S. Li, X. Huang, J.-N. Chang, J.-H. Wang, J. Zhou, S.-L. Li, and Y.-Q. Lan. "Coordination environment dependent selectivity of single-site-Cu enriched crystalline porous catalysts in CO_2 reduction to CH4". In: *Nature Communications* 12.1 (2021), p. 6390.

[65] I. Hod, M. D. Sampson, P. Deria, C. P. Kubiak, O. K. Farha, and J. T. Hupp. "Fe-porphyrin-based metal–organic framework films as high-surface concentration, heterogeneous catalysts for electrochemical reduction of CO_2". In: *Acs Catalysis* 5.11 (2015), pp. 6302–6309.

[66] L. Zhang, J. Niu, M. Li, and Z. Xia. "Catalytic mechanisms of sulfur-doped graphene as efficient oxygen reduction reaction catalysts for fuel cells". In: *The Journal of Physical Chemistry C* 118.7 (2014), pp. 3545–3553.

[67] L. Zhang, C.-Y. Lin, D. Zhang, L. Gong, Y. Zhu, Z. Zhao, Q. Xu, H. Li, and Z. Xia. "Guiding principles for designing highly efficient metal-free carbon catalysts". In: *Advanced Materials* 31.13 (2019), p. 1805252.

[68] M. R. Singh, J. D. Goodpaster, A. Z. Weber, M. Head-Gordon, and A. T. Bell. "Mechanistic insights into electrochemical reduction of CO_2 over Ag using density functional theory and transport models". In: *Proceedings of the National Academy of Sciences* 114.42 (2017), E8812–E8821.

[69] W. Zhu, R. Michalsky, Ö. Metin, H. Lv, S. Guo, C. J. Wright, X. Sun, A. A. Peterson, and S. Sun. "Monodisperse Au nanoparticles for selective electrocatalytic reduction of CO_2 to CO". In: *Journal of the American Chemical Society* 135.45 (2013), pp. 16833–16836.

[70] B. Hammer and J. K. Nørskov. "Theoretical surface science and catalysiscal-culations and concepts". In: *Advances in catalysis*. Vol. 45. Elsevier, 2000, pp. 71–129.

[71] A. Grimaud, K. J. May, C. E. Carlton, Y.-L. Lee, M. Risch, W. T. Hong, J. Zhou, and Y. Shao-Horn. "Double perovskites as a family of highly active catalysts for oxygen evolution in alkaline solution". In: *Nature communications* 4.1 (2013), p. 2439.

[72] J. Suntivich, H. A. Gasteiger, N. Yabuuchi, H. Nakanishi, J. B. Goodenough, and Y. Shao-Horn. "Design principles for oxygen-reduction activity on perovskite oxide catalysts for fuel cells and metal–air batteries". In: *Nature chemistry* 3.7 (2011), pp. 546–550.

[73] K. Toyoda, R. Hinogami, N. Miyata, and M. Aizawa. "Calculated descriptors of catalytic activity for water electrolysis anode: application to delafossite oxides". In: *The Journal of Physical Chemistry C* 119.12 (2015), pp. 6495–6501.

[74] W. Zhang, Y. Hu, L. Ma, G. Zhu, Y. Wang, X. Xue, R. Chen, S. Yang, and Z. Jin. "Progress and perspective of electrocatalytic CO_2 reduction for renewable carbonaceous fuels and chemicals". In: *Advanced Science* 5.1 (2018), p. 1700275.

[75] M. Yu, R. Dong, and X. Feng. “Two-dimensional carbon-rich conjugated frameworks for electrochemical energy applications”. In: *Journal of the American chemical society* 142.30 (2020), pp. 12903–12915.

[76] H. Zhong, M. Wang, G. Chen, R. Dong, and X. Feng. “Two-dimensional conjugated metal–organic frameworks for electrocatalysis: opportunities and challenges”. In: *ACS nano* 16.2 (2022), pp. 1759–1780.

[77] L. Wang, S. E. Saji, L. Wu, Z. Wang, Z. Chen, Y. Du, X.-f. Yu, H. Zhao, and Z. Yin. “Emerging synthesis strategies of 2D MOFs for electrical devices and integrated circuits”. In: *Small* 18.33 (2022), p. 2201642.

[78] J. Liu, D. Yang, Y. Zhou, G. Zhang, G. Xing, Y. Liu, Y. Ma, O. Terasaki, S. Yang, and L. Chen. “Tricycloquinazoline-based 2D conductive metal-organic frameworks as promising electrocatalysts for CO_2 reduction”. In: *Angewandte Chemie International Edition* 60.26 (2021), pp. 14473–14479.

[79] S. A. A. Razavi and A. Morsali. “Linker functionalized metal-organic frameworks”. In: *Coordination Chemistry Reviews* 399 (2019), p. 213023.

[80] J. Wang, M. Sun, H. Xu, F. Hao, Q. Wa, J. Su, J. Zhou, Y. Wang, J. Yu, P. Zhang, *et al.* “Coordination Environment Engineering of Metal Centers in Coordination Polymers for Selective Carbon Dioxide Electroreduction toward Multicarbon Products”. In: *ACS nano* (2024).

[81] T. A. Al-Attas, N. N. Marei, X. Yong, N. G. Yasri, V. Thangadurai, G. Shimizu, S. Siahrostami, and M. G. Kibria. “Ligand-engineered metal–organic frameworks for electrochemical reduction of carbon dioxide to carbon monoxide”. In: *ACS Catalysis* 11.12 (2021), pp. 7350–7357.

[82] X. Cui, M. Wu, G. Hou, Y. Li, Y. Wang, Y. Wang, J. Huang, M. Zhao, Z.-Z. Luo, Z. Zou, *et al.* “Alkali Metal Ions Stabilizing Copper (I)–Sulfur Bonds for Efficient Formate Production from Electrochemical CO_2 Reduction”. In: *ACS Catalysis* 14.15 (2024), pp. 11857–11864.

[83] W. Lu, Z. Wei, Z.-Y. Gu, T.-F. Liu, J. Park, J. Park, J. Tian, M. Zhang, Q. Zhang, T. Gentle III, *et al.* “Tuning the structure and function of metal–organic frameworks via linker design”. In: *Chemical Society Reviews* 43.16 (2014), pp. 5561–5593.

[84] C. Ding, C. Feng, Y. Mei, F. Liu, H. Wang, M. Dupuis, and C. Li. “Carbon nitride embedded with transition metals for selective electrocatalytic CO_2 reduction”. In: *Applied Catalysis B: Environmental* 268 (2020), p. 118391.

[85] T. Shinagawa, G. O. Larrazábal, A. J. Martín, F. Krumeich, and J. Pérez-Ramírez. “Sulfur-modified copper catalysts for the electrochemical reduction of carbon dioxide to formate”. In: *ACS Catalysis* 8.2 (2018), pp. 837–844.

[86] M. Ding, X. Cai, and H.-L. Jiang. “Improving MOF stability: approaches and applications”. In: *Chemical Science* 10.44 (2019), pp. 10209–10230.

[87] L. Falicov and G. Somorjai. “Correlation between catalytic activity and bonding and coordination number of atoms and molecules on transition metal surfaces: Theory and experimental evidence”. In: *Proceedings of the National Academy of Sciences* 82.8 (1985), pp. 2207–2211.

[88] X. Liang, D. Wang, Z. Zhao, T. Li, Y. Gao, and C. Hu. “Coordination number dependent catalytic activity of single-atom cobalt catalysts for Fenton-like reaction”. In: *Advanced Functional Materials* 32.38 (2022), p. 2203001.

[89] Y. Zhang, L. Jiao, W. Yang, C. Xie, and H.-L. Jiang. “Rational fabrication of low-coordinate single-atom Ni electrocatalysts by MOFs for highly selective CO_2 reduction”. In: *Angewandte Chemie International Edition* 60.14 (2021), pp. 7607–7611.

[90] Y. Xu, F. Li, A. Xu, J. P. Edwards, S.-F. Hung, C. M. Gabardo, C. P. OBrien, S. Liu, X. Wang, Y. Li, *et al.* “Low coordination number copper catalysts for electrochemical CO_2 methanation in a membrane electrode assembly”. In: *Nature communications* 12.1 (2021), p. 2932.

[91] Y. Peng, S. Sanati, A. Morsali, and H. García. “Metal–organic frameworks as electrocatalysts”. In: *Angewandte Chemie International Edition* 62.9 (2023), e202214707.

4

[Cu-S]-Organic Framework for Selective Reduction of CO_2 to Formate

Abstract

The development of advanced catalysts with innovative nanoarchitectures is critical for addressing energy and environmental challenges such as the electrochemical CO_2 reduction reaction (CO_2RR). In this work, we present the synthesis of an innovative copper-sulfur planar structure, Cu-S-BDC, within a metal-organic framework (MOF) catalyst, which demonstrates 100% selectivity towards formate as the sole carbon product. Structural analysis and surface characterizations reveal that Cu-S-BDC exhibits quasi-two-dimensional inorganic building units, with Cu bonded to two S-CH_3 groups and one BDC linker, while carboxylate groups adopt a bridging coordination mode. This unique arrangement not only imparts remarkable structural stability but also enhances the electronic properties of the MOF, as evidenced by a narrow band gap of 1.203 eV that facilitates efficient charge transfer and increased electrochemical current density in CO_2RR. Notably, it offers a Faradaic efficiency (FE) of 92% for formate at an overpotential as low as -0.4 V vs. the reversible hydrogen electrode (RHE) in an aqueous electrolyte of 1 M KOH, as well as a current density of -25.8 mA/cm^2 at -0.9 V vs. RHE, averaged over 24 hours of electrolysis. This study highlights a fresh perspective in the field of MOF electrocatalysts by demonstrating that engineering the metal coordination environment can significantly enhance the electronic properties and conhersequently improve the electrocatalytic performance of these materials.

This chapter has been published as:
K. Roohi, M. Soleimani, N. Khossossi, S. Canossa, A. Kosari, S. Mohseni Armaki, M. Ahmadi, E. van der Veer, M. Ramdin, P. Anusuyadevi, P. Gonugunta, A. Mol, P. Dey, P. Taheri, Planar [CuS]-Organic Framework for Selective and Low Overpotential CO_2 to Formate Reduction, *Small Structures*, 2025: 2500235

4.1. Introduction

The increasing concentration of carbon dioxide (CO_2) in the atmosphere raises significant concerns about our dependence on fossil fuels for energy generation [1]. Consequently, various strategies aimed at achieving a carbon-neutral footprint are being developed, including the exploration of environmentally friendly energy sources and carbon cycles as viable alternatives to fossil fuels. [2, 3]. Electrochemical carbon dioxide reduction reaction (CO_2RR) powered by renewable electricity offers a promising approach to convert CO_2 into valuable chemicals, simultaneously achieving carbon recycling and renewable energy storage [4–6]. However, CO_2RR often encounters challenges such as low selectivity and faradaic efficiency (FE) along with limited current density [7]. Furthermore, electrocatalyst materials employed in CO_2RR often generate a diverse array of products, necessitating supplementary separation or conversion processes. These additional steps incur added costs for both implementation and operation [8]. In this context, the design of efficient electrocatalysts capable of selectively converting CO_2 into targeted products while maintaining a high level of activity represents a significant research opportunity [9, 10].

Commonly investigated CO_2RR electrocatalysts in research include various metal-related substances such as metal oxides, metal alloys, bi-metals, transition metals, metal chalcogenides and metal-organic complexes [11–15]. Pioneering investigations have shown that among all transition metals, copper-based electrodes exhibit the highest catalytic activity in converting CO_2 into valuable chemicals [16–18]. Nevertheless, the selectivity of the reaction towards a specific product on copper-containing electrocatalysts remains considerably below the levels required for practical applications [19]. The fundamental reason for the relatively limited selectivity of metallic copper catalysts is attributed to the linear relationship observed in the binding energies of the three primary CO_2RR intermediates: *CO, *COOH, and *CHO [20, 21].

Various material innovative strategies have been proposed to disrupt the linear scaling of intermediates. A particularly promising approach is ensemble control, which entails identifying the smallest active site and its surrounding space essential for the desired reaction, and then deliberately tailoring it [22]. In this regard, theoretical research suggests that p-block elements, such as sulphur could contribute to CO_2 bond formation on electrocatalyst surfaces, potentially disrupting the linear scaling relationships observed for metals [23]. Specifically, Cu-S bonds could influence the binding strength of *HCOO and *COOH intermediates by suppressing the key intermediate of the hydrogen evolution reaction (HER), i.e.*H, ultimately favouring the formation of the target CO_2RR product, formate [24–26].

While the atomically precise incorporation of selectivity modifiers into the metallic based catalysts is challenging, metal-ligand complexes, such as Metal-Organic Frameworks (MOFs), offer exceptional structural tunability, making them ideal materials for this purpose. Additionally, MOFs provide porosity and a large surface area, further enhancing their suitability for electrocatalyst applications [27–29].

Despite these advantages, the utilization of MOFs in electrocatalyst applications has been limited by their poor conductivity, resulting in low current density [30].

This limitation primarily stems from the use of carboxylate linkers in constructing multidimensional structural frameworks. The high electronegativity of the oxygen atoms in these carboxylates increases the potential required for electron passage through the organic linkers [31]. Consequently, there is a diminished overlap between the oxygen atoms and the metal d-orbitals, leading to the low electrical conductivity observed in most reported MOFs [32].

To address this issue, incorporating metalsulphur bonds improves the electrical conductivity of the MOF due to the strong overlap between the sulphur p-orbitals and the metal d-orbitals, facilitating efficient charge transfer through chemical bonds. Notably, in multidimensional MOFs, the planar metalsulphur bond formed through a chain network demonstrates anisotropic behaviour, restricting charge transport to a single dimension and thereby enhancing the MOF's conductivity. In particular, a 2D building unit of these planar metalsulphur bonds within the MOF structure facilitates charge transfer, consequently enhancing overall conductivity [33–35].

As a result, incorporating planar Cu-S bonds into the MOF structure offers benefits in two critical aspects of CO_2RR. Firstly, it selectively promotes the formation of a single product during CO_2RR by disrupting the linear scaling of intermediates. Secondly, its high conductivity enhances the electrochemical reduction current density due to facile charge transfer. Consequently, our study delves into the structural tuning of copper benzenedicarboxylic acid MOF, Cu-BDC, by incorporating sulfur into the framework in a controlled manner, resulting in the formation of the Cu-S-BDC structure. The resulting enhanced MOF exhibits a thin flake morphology with planar Cu-S bonds , which serve as catalytically active sites for selective CO_2RR towards formate production. This work, supported by experimental and theoretical evidence, marks a significant accomplishment in designing highly conductive and selective MOFs paving the way for the rapid development of novel and highly efficient crystalline materials for CO_2RR applications.

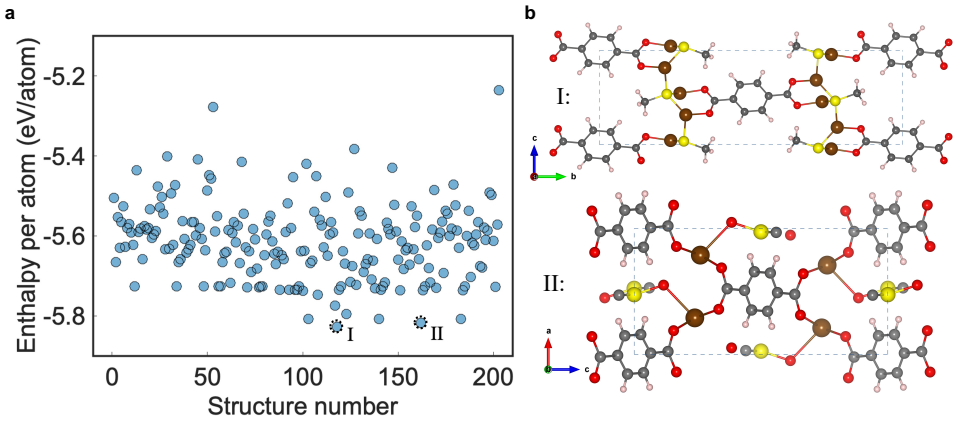

Figure 4.1: Design: **a**, USPEX evolutionary crystal structure prediction of Cu-S-BDC MOF, showcasing the enthalpy per atom of all candidate crystal structures along the evolutionary trajectory. A dashed black circle denotes the first occurrence of the final global minimum, representing the lowest-energy unit cell predicted for Cu-S-BDC MOF. **b,** Two lowest-energy unit cells of Cu-S-BDC MOF, with structure 'I' being more probable due to its slightly lower energy. The color scheme represents Cu (brown), S (yellow), C (grey), O (red), and H (pink) atoms.

4.2. Methodology

Chemicals:

Copper(II) nitrate ($Cu(NO_3)_2.3H_2O$, 99.999%), benzenedicarboxylic ($C_8H_6O_4$), dimethyl sulfoxide (DMSO) (99.999%), dimethylformamide (99,999%), isopropanol and, KOH all were purchased from Sigma-Aldrich. Polytetrafluoroethylene 55 wt % dispersion in water was obtained from FUELCELL store. An ultrapure purification system (Milli-Q advantage A10) produced the deionized water purification system (19.2 MΩcm) used to make the solutions. The gas diffusion electrodes (GDE) from FUELCELL store were cut to 6.76 cm^2 and used as substrates for CO_2RR electrochemical measurements.

MOF synthesis:

For the synthesis of Cu-S-BDC and Cu-BDC MOFs, $Cu(NO_3)_2$ and Terephthalic acid were combined in a 1:2 molar ratio, followed by the addition of 30 mL of DMSO and DMF, respectively. The mixture underwent stirring for 30 minutes to ensure complete dissolution of the precursors. Subsequently, the homogeneous mixture was carefully transferred to a 50 ml Teflon-lined stainless steel autoclave, sealed with Teflon tape. The sealed autoclave was then placed in an oven and heated to 140°C for 24 hours. Once the reaction concluded, the autoclave was cooled to room temperature and the resulting MOF crystals were collected using filter paper. To eliminate any residual unreacted precursors, the collected crystals underwent multiple wash cycles with DMSO and DMF. Finally, the washed crystals were air-dried at room temperature.

Electrode preparation:

Dried Cu-S-BDC and Cu-BDC MOF powders were mixed with PTFE (4:1 w%) in a water and isopropanol solution (1:1 vol%) to form an ink with an active material

concentration of 5 mg/mL. The ink was then drop-cast onto GDE (catalyst loading of 1.5 mg/cm^2) using a pipette and dried under ambient air.

Characterization of materials:

Powder X-ray diffraction (PXRD) was carried out with a Bruker D8 Advance diffractometer X-ray powder diffractometer equipped with a Cu-sealed tube (λ = 1.54178 Å at 45 kV and 40 mA. Single-crystal X-ray diffraction analysis was performed at the Elettra Synchrotron facility (XRD1 beamline). Data have been processed using the CrysAlisPro software package version 42.49. Detailed information on the measurement and interpretation can be found in the Supplementary Information under the SCXRD section. The CIF file containing crystallographic details and structure factors is available free of charge on the Cambridge Crystallographic Data Centre website (www.ccdc.cam.ac.uk) using the identifier CCDC2304584.

Picturing of the main planes was done by a double-corrected and monochromated Themis Z scanning transmission electron microscope (Thermo Fisher Scientific) operating at 300 kV equipped through high-angle annular dark-field (HAADF) STEM mode and integrated differential phase contrast (iDPC) STEM by using 80% coverage of a 4-segmented DF detector. The beam convergence angle was measured 16-24.0 and the probe current of 1.0 pA was used for STEM imaging. Data acquisition and analysis were done using Velox software. For this purpose, TEM samples were prepared by drop-casting a few droplets of NPs in EtOH onto the quanti foil C-support gold grids covered with single/mono layer of CVD-grown graphene to avoid beam damage. Then particles were sandwiched between the graphene layer by placing another grid on top of grids with MOF particles. The details of TEM sample preparation is available under TEM section in Supplementary information. The multislice simulation was performed using the DrProbe software package [36]. An orthogonal unit cell was first constructed with one of its axes aligned along the [1 0 0] zone axis of the experimental image. Phase gratings were calculated over a 5*5 nm area. An inner 3*3 nm square was then used for the subsequent simulation with a total thickness of 6 nm. A relatively large pixel size of 20 pm was chosen to limit computation time. All other simulation parameters were chosen to mimic the experimental setup.

Moreover, ThermoFisher Spectra Ultra (S)TEM operated at 300 kV was used for extremely low-dose imaging through the integrated Differential Phase Contrast (iDPC) STEM technique. This was performed using a Panther Detector, a segmented STEM detection system, with a probe current of 1 pA at a convergence semi-angle of 10 mrad. The sample was prepared by drop-coating the particles, which were sonicated and dispersed in ethanol, onto an ultra-thin carbon support film TEM grid.

Scanning electron microscope (SEM) observation was performed with a field emission-scanning electron microscope (JEOL JSM-7401F or Magellan 400 XHR) equipped with electron dispersive spectroscopy (EDS). X-ray photoelectron spectroscopy (XPS) analysis was conducted using a PHI-TFA XPS spectrometer (Physical Electronic Inc.). The device is equipped with an X-ray Al-monochromatic source. The vacuum level inside the measuring chamber is maintained at 10^{-9} mbar. The analysis region measures 0.4 mm in diameter. We conducted precise multiplex scans of the peaks with a narrow focus, utilizing a pass energy of 71.55 eV and a step size of 0.1 eV.

The measurements were carried out at an angle of 45° with respect to the sample surface. Spectral processing was performed using Multipak v8.0 (Physical Electronics Inc., Chanhassen, MN, USA). Elemental composition was determined from the XPS survey spectra, while high-energy resolution spectra of S2p and Cu2p, C1s and O1s photoelectron peaks were subjected to curve fitting.
A Thermo-Nicolet Nexus Fourier-transform infrared spectroscopy (FTIR) apparatus was used equipped with a liquid-nitrogen-cooled mercury cadmium tellurium detector and a nitrogen-purged measurement chamber. The Raman spectra have been achieved by WiTeC Alpha300R Raman Imaging microscope, using 532nm laser with 0.2mW laser power to avoid damaging the samples with an integration time of 8 seconds and 10 accumulations. The sample was prepared by dissolving sample powder in IPA and drop casting on quartz slides. Thermogravimetric analyses were performed using the TAG 1750 instrument manufactured by Setaram. The powders were heated from ambient temperature to 900 °C with a heating rate of 50 °C/min to mimic the sintering cycle used in the experiments. For the DSC, the powders were heated from ambient temperature up to 600 °C and back to ambient temperature with a heating and cooling rate of 5 °C/min to closely measure heat flow at each temperature step. N_2 physisorption experiments were performed using a Micromeritics Tristar II 3020 at 77 K. Before the gas-sorption experiments 100 mg of MOF was washed and dried for 5 hours at 100 °C.

Electrochemical measurements and product analysis:

A flow cell (Dioxide Materials.) with a Nafion anion exchange membrane from FORBLUE SELEMION was used for all electrochemical measurements (Fig. 4.2). The working electrode was a squared GDE coated with MOF (2.6 × 2.6 cm, area, 6.76 cm^2). An Iridium plate from Magneto Special Anodes B.V. and a leak-free Ag/AgCl reference electrode (Innovative Instruments LF-1-45) were used as counter electrode and reference electrode, respectively. After IR correction, all potentials were converted into those vs. RHE.
1 and 0.5 M KOH solutions were cycled through the cathode and anode compartments, respectively with a 10 mL/min flowrate. CO_2 was bubbled from the back of the cell with a flow rate of 20 mL/min for 1.5 hours to reach the electrolyte saturation. In the case of Ar flow, the same procedure was repeated.
Linear sweep voltammograms (LSV) were recorded in Ar and CO_2-saturated 1 M KOH at a scan rate of 5 mV/s. Electrochemical impedance spectroscopy (EIS) measurements were performed for Cu-S-BDC and Cu-BDC MOFs in CO_2-saturated 1 M KOH in the frequency range of 1 MHz to 100 mHz.
To conduct product analysis measurements, chronoamperometric measurements were conducted in 1 M KOH solution saturated with CO_2 and Ar. The measurements were carried out at constant potentials of -0.4, -0.5, -0.6, -0.7, -0.8, -0.9, and -1 V versus the RHE for a duration of 1 hour each. Samples of 1 mL were collected from the electrolyte reservoir at 10-minute intervals to analyze liquid products using high-performance liquid chromatography (HPLC). Gas and liquid product FE were calculated every 2.5 minutes and 10 minutes, respectively. Gas product analysis from the cathode compartment was done with gas chromatography (GC from Agilent) equipped with two thermal conductivity detectors (TCD) to measure CO_2, CO, and

H_2 in 2-minute intervals. A standard calibration curve was made using custom gas mixture cylinders with known concentrations of product gasses in CO_2 (Linde gas Benelux B.V.). The liquid products were quantified using high-performance liquid chromatography (HPLC, Agilent 1260 Infinity). 5 μL of the liquid sample was injected into two Aminex HPX 87-H columns (Bio-rad) placed in series. The column oven temperature was maintained constant at 60 $°C$, with a steady flow rate of 0.6 mL/min of an aqueous 1 mM H_2SO_4 eluent, and a refractive index detector (RID) was used for product detection.
Faradaic efficiencies were calculated using equation 5.1

$$\frac{n_{\mathrm{i}}NF}{jt} \tag{4.1}$$

where n_i represents the number of moles of the detected product, N is the number of the transferred electrons in a reaction, F is the Faradaic constant (s A/mol), j is the current density (A) and t is the time of the measurement in seconds.

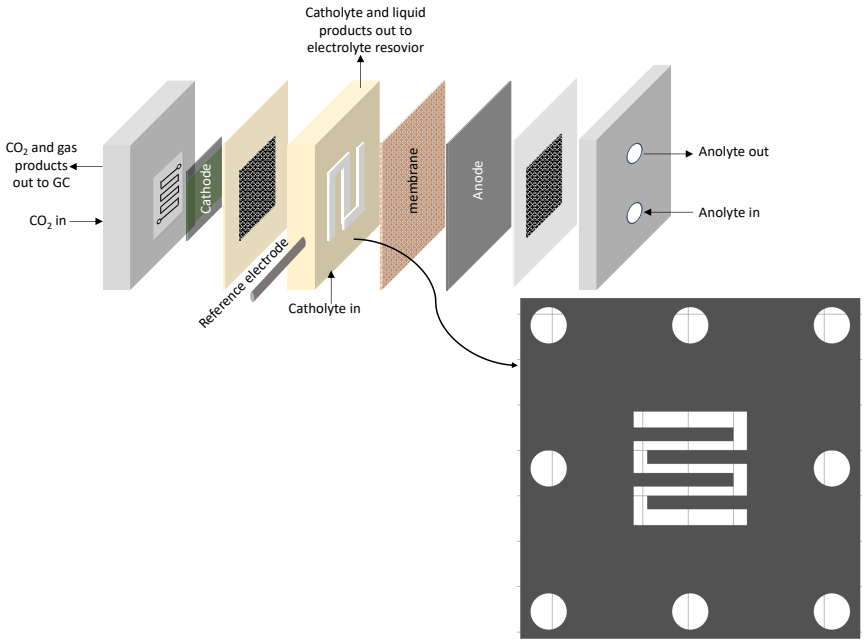

Figure 4.2: Schematic of the modified flow cell utilized for electrochemical measurements and product analyses.

DFT Calculations:
The global optimization of the proposed MOF structure was conducted using the ab initio USPEX evolutionary algorithm methodology for crystal structure prediction. A total of 160 initial structures were considered over 10 distinct generations in the

USPEX simulation. To address the limitations of the local optimizations within USPEX, which are performed using relatively weak convergence criteria and small basis sets to accelerate the evolutionary run, the ground state structures were subsequently subjected to a new local optimization process with a high cut-off and large basis sets. The Density Functional Theory (DFT) computations were carried out based on the Vienna ab initio simulation package (VASP) [37–39]. The generalized gradient approximation in the form of Perdew Burke Ernzerhof (PBE) [40] functional was adopted self-consistently through the approach of the Projector Augmented Wave (PAW) [41] by Kohn-Sham electron wave functions expanded with an energy cutoff of 550 eV and the convergence criteria during the structural optimizations were set to 10^{-6} eV and 10^{-3} eV/Å for energy and force, respectively. The Monkhorst Pack K-point [42] of the $9 \times 1 \times 5$ grid is used in the reciprocal space during the geometrical optimizations. The charge transfer between atoms is evaluated based on the Bader charge algorithm [43]. The open-source package vaspkit [44] was used for the state of density and the thermodynamics (298.15 K and 1 atm) calculations. For Gibbs free energy, the following equation was used:

$$G = H - T\Delta S = E_{\mathrm{DFT}} + E_{\mathrm{ZPE}} + \int_0^{298.15} C_v \, dT - T\Delta S \tag{4.2}$$

where H refers to the enthalpy, E_{DFT} refers to the electronic adsorption energy and E_{ZPE} signifies the zero-point vibrational energy. The calculation also includes the heat capacity ($\int_0^{298.15} C_v \, dT$) and entropy correction ($T\Delta S$) as the third and fourth components, respectively, derived from frequency calculations. For the gas molecules, we referenced the data from the study by Klinkova et al. [45]. To mitigate the overestimation typically seen in DFT calculations [24, 46], these corrections were applied: CO_2 (0.45 eV), HCOOH (0.20 eV), and the adsorbed COOH* (0.20 eV). Finally, the adsorption energy was calculated through the following equations:

$$E^{ads}_{\mathrm{COOH}} = E_{\mathrm{COOH}*} - E_{\mathrm{MOF}} - (E_{\mathrm{HCOOH}} - \frac{1}{2}E_{\mathrm{H_2}}) \tag{4.3}$$

$$E^{ads}_{\mathrm{HCOO}} = E_{\mathrm{HCOO}*} - E_{\mathrm{MOF}} - (E_{\mathrm{HCOOH}} - \frac{1}{2}E_{\mathrm{H_2}}) \tag{4.4}$$

E_{MOF} and E_{Molecule} refer to the ground state energy of the pristine MOF system and isolated molecule, respectively. Herein, we take the following reaction 5.5 as an example to show the calculation of Gibbs free energy variation based on the equation 5.6, where e is the charge number, and U is the external applied voltage, for the calculation of free energy of H^+ and e^-, the computational hydrogen electrode model [47] was used to calculate the Gibbs free energy of proton/electron:

$$COOH* + H^+ + e^- \leftrightarrow HCOOH^+ \tag{4.5}$$

$$\begin{aligned}\Delta G &= G_* + G_{\mathrm{HCOOH}} - G_{\mathrm{COOH}^*} - (G_{\mathrm{H}^+} + G_{e^-}) \\ &= G_* + G_{\mathrm{HCOOH}} - G_{\mathrm{COOH}^*} - \left(\frac{1}{2}G_{\mathrm{H_2}} - eU\right)\end{aligned} \tag{4.6}$$

Working Principle of the USPEX

The crystal structure prediction was carried out by using USPEX 9.4.4 Package [48, 49]. All quantum chemical calculations within the USPEX simulations were performed using the VASP package [37–39] for the local optimization of candidate structures. A typical USPEX workflow is illustrated in Supplementary Fig. 4.3. USPEX first randomly generates a set of structures known as candidate structures. These structures are called a generation or, depending on the context, population. We use the term generation when discussing a particular set of structures, for example, from Generation I. Population refers to all considered candidate structures within one USPEX structure prediction run. After random generation, the candidate structures are locally optimized by VASP package. When the local optimizations of all structures in the generation are finished, the next generation has to be built by using variation operators on the lowest-energy structures from the previous generation. Furthermore, a small number of randomly generated structures are added to diversify the population. USPEX uses the following variation operators: heredity, permutation, lattice mutation, and atomic mutations. Next, the structures from the new generation are locally optimized and the above-described process is repeated until the halting criterion is met. Usually, USPEX stops when the same lowest-energy structure is produced in several generations in a row. Overall, a minimal USPEX input file contains (a) atom types and the amount of each element, (b) size and number of generations, and (c) parameters of the USPEX algorithm (Fig. 4.3).

Single crystal XRD

SCXRD data were collected at the Elettra Synchrotron facility (Beamline XRD1). Suitable crystals were isolated and mounted on a MiTeGen loop in a droplet of a perfluoropolyether oil. Diffraction data were acquired using a monochromatic 0.650 Å radiation at a temperature of 100K, using a cold dry nitrogen stream produced with an Oxford Cryostream (Oxford Cryosystems Ltd., Oxford, United Kingdom). The crystal was placed directly under the Cryostream at 100K without any temperature ramp in going from room temperature to cryogenic conditions. Frames were collected on a Pilatus 2M hybrid pixel photon counting detector, running a phi scan with oscillation 0.5° and covering an angular range of 360°. The resulting diffraction images were processed using the software CrysAlisPro version 43.90.

Data integration based on the two major domains provided the best reflection file when only the first domain was considered. Structure solution and refinement using the intensities from this domain were conducted using suite Olex2-1.5 (OlexSys Ltd. 20042023) software. Structure solution was achieved by the program ShelXT, while refinements were based on the least-squares method by the program ShelXL [50]. All atoms except hydrogens were refined anisotropically, with occupancy factors fixed at 1. Free occupancy refinements provided analogous values, indicating that no missing

linkers/metal defects can be detected from the available data. Hydrogen atoms were fixed in idealized positions by appropriate AFIX commands. Residual electron densities could be recognized around the heavy atoms, likely due to the relatively poor quality of the extracted intensities due to the complex twinning. Such residues reasonably oscillate around 0, having a maximum peak at 1.7 and a minimum hole at -1.6 electrons/$Å^3$.

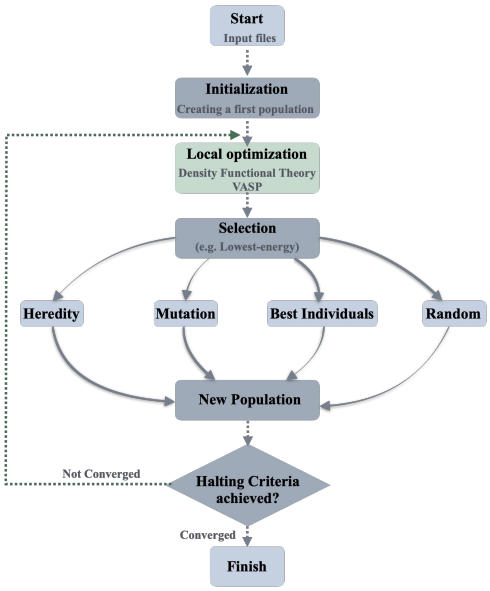

Figure 4.3: Typical USPEX and DFT workflow used for the Cu-S-BDC MOF crystal structure prediction

Transmission electron microscopy

Procedure of fabricating the graphene-coated TEM grids:

Materials:

Au TEM grids coated with amorphous carbon layer, Graphene on Cu foil, Isopropyl Alcohol (IPA, anhydrous), Cu etchant (Sigma), Convex cover glass with significant curvature, Beaker as an enclosure while etching, distilled water, glass vial, pasteur pipette, vacuum pump.

Methods:

Graphene on Cu foil is placed on a clean convex cover glass. The Au TEM grid coated with an amorphous carbon layer then is placed over it with the carbon side facing down. Afterwards, anhydrous IPA is poured onto the cover glass such that the TEM grids remained afloat. IPA is slowly decanted with the help of a long-tip Pasteur pipette. Following, 2-3 mL of Cu etchant (Ferric chloride solution) is, and it undergoes etching of the Cu foil for 30 minutes. Within a few minutes, the solution starts to turn green, showing the oxidation of Cu foil. Further, etchant solution should be removed and be added freshly again at least thrice every 10 minutes to achieve the complete etching of Cu foil. Once all the copper is etched away, only the TEM grids remain

floating. The graphene is then carefully ruptured using tweezers to separate the TEM grids. The etching solution should be completely washed away using distilled water. Lastly, graphene-coated TEM grids are carefully removed and rinsed with distilled water in a glass vial, and then transferred to a grid holder to dry under high vacuum.

4.3. DESIGN, SYNTHESIS AND CRYSTAL STRUCTURE DETERMINATION

With the primary objective of introducing sulphur into the structural composition of Cu-BDC, dimethyl sulfoxide solvent (DMSO) together with Cu(II) salt and BDC linker were defined as precursors. Using the ab initio USPEX method, the optimized Cu-S-BDC MOF candidates were generated (Fig. 4.1a). The most optimized MOF structure candidates, I and II, are shown in Fig. 4.1b. As aimed, the high feasibility of sulphur binding with Cu is exhibited in 4.1b-(I). The prospective cell parameters of both structures are listed in Table 4.1. Also, the Cu-S, C-H, C-S, and C-O bond lengths in the predicted structure are equal to 2.2305, 1.093, 1.820, and 1.275 Å, respectively.

Accordingly, Cu-BDC MOF was synthesized in DMSO solvent, resulting in the formation of a green-colored, rectangular, thin sheet of crystalline Cu-S-BDC MOF (Fig. 4.6a). This differs from the conventional Cu-BDC MOF synthesized in dimethylformamide (DMF) solvent, which typically displays a thicker plate morphology, as previously reported [51]. The formation mechanism of Cu-S-BDC MOF could be explained through the reaction of Cu(II) salt with decomposed DMSO in the presence of BDC linker. At a temperature of 140^{o}C, DMSO undergoes decomposition to form thiol (RSH) [52], which serves as a reducing agent. Due to the excess amount of DMSO in the precursor mixture, Cu^{2+} ions are reduced by S-CH_3 compounds to Cu^{+}, which initially react with the thiols. Subsequently, the BDC linker becomes engaged in the reaction, occupying the remaining coordination sites of Cu^{+}.

Table 4.1: Computed structural properties of the most stable structures predicted by USPEX

Predicted Cu-S-BDC	Lattice parameters (Å)			Lattice angle (°)		
	a	b	c	α	β	γ
Cu-S-BDC-I	3.945	23.471	7.470	90.00	99.951	90.00
Cu-S-BDC-II	6.829	21.826	13.757	90.00	90.00	90.00

Energy dispersive spectroscopy (EDS) analyses of Cu-S-BDC MOF sample confirm the distribution of S, C, O, and Cu (Fig. 4.4a). Moreover, Fourier-transform infrared spectroscopy (FTIR) of the synthesized MOF (Fig. 4.4b) indicates the presence of Cu-S bond demonstrated by the peak at 823 cm^{-1} [53] whereas as the highlighted peaks at 1294 cm^{-1}, and 1316 cm^{-1} are attributed to C-H vibrations originating from DMSO. The major peaks at wavelengths of 1398 and 1550 cm^{-1} are respectively correlated to symmetric and asymmetric stretching modes of coordinated carboxylate. Moreover, peaks at 971 and 1013 cm^{-1} are related to C-H and Cu-O-C, respectively [54]. The peak at 741 cm^{-1} originates from the C-H vibrational band of the aromatic ring [55]. Thermogravimetric analysis (TGA) and mass spectrometry (MS) were conducted to

identify the compounds released from the MOF at elevated temperatures and to evaluate its thermal stability (Fig. 4.4c,d). The analysis confirms the presence of sulphur-containing compounds, as these compounds are observed to decompose and exit when the temperature reaches 320°C. The TGA profile of Cu-S-BDC MOF suggests that the MOF is stable up to 300°C. However, beyond this temperature, the MOF undergoes significant decomposition, concurrent with the simultaneous breakage of Cu-O and Cu-S bonds, as indicated by online MS measurements. The observed decomposition of the BDC linker aligns well with the reported decomposition temperature [54]. It is also observed from the pore size distribution plot from BET measurements (Supplementary Fig. 4.4e) that the effective pore size of the MOF is 3.95 nm. This is almost 10 times bigger than the kinetic diameter of CO_2 molecule, 3.3 Å, which assures the diffusion of CO_2 into the pores for further reaction at the active sites [56].

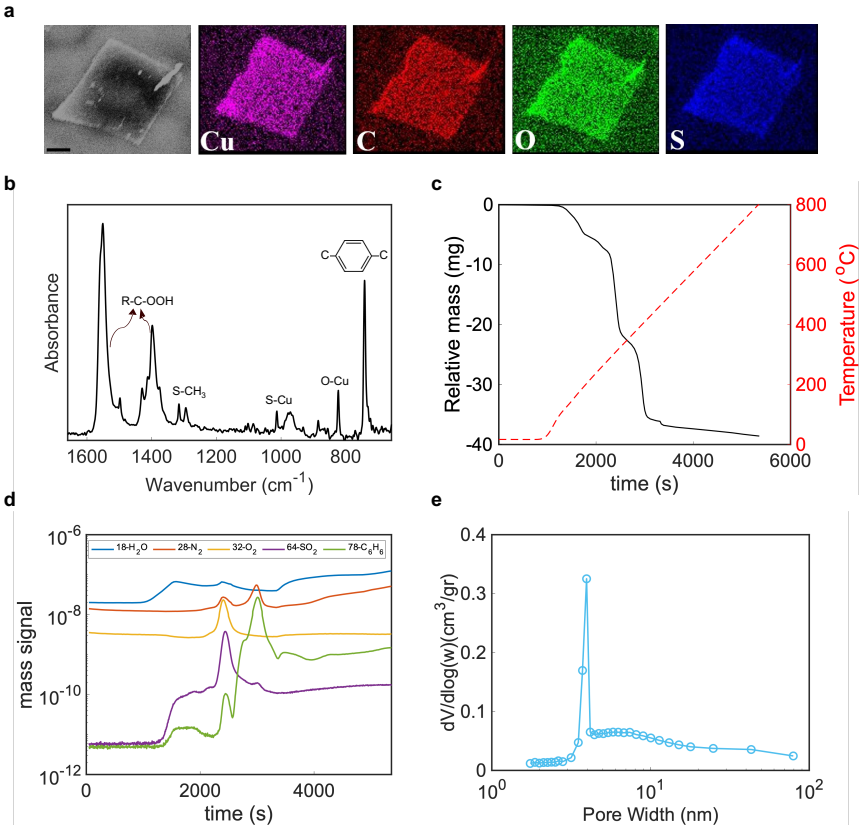

Figure 4.4: **a**, SEM and EDS of the as-synthesized Cu-S-BDC. Scale bar, 5 μm. Cu, C, O, and S were the only elements detected by EDS on nanosheets. **b**, FTIR spectrum of the as-synthesized Cu-S-BDC. **c**, TGA plot of the as-synthesized Cu-S-BDC MOF and **d**, Coupled mass spectrometry with TGA reveals the compounds leaving the system at elevated temperatures. **e**, The pore size distribution analysis of Cu-S-BDC.

Reciprocal space reconstructed of Cu-S-BDC MOF obtained from single crystal X-ray diffraction (SCXRD) are shown in Fig. 4.5. Four different twins were identified in the data with the following information. Twin information:
1: 3.9881 23.5911 7.5710 90.048 98.667 89.863 704.2
2: 3.9820 23.5798 7.5870 89.686 98.748 89.954 704.1
3: 3.9895 23.6156 7.5692 89.358 98.752 89.138 704.7
4: 3.9948 23.5827 7.5746 89.632 98.775 90.533 705.2

1: Total: 2652(61.1%) Separate: 963(22.2%) Overlapped: 1689(38.9%)
2: Total: 1075(24.8%) Separate: 535(12.3%) Overlapped: 540(12.4%)
3: Total: 1240(28.6%) Separate: 339(7.8%) Overlapped: 901(20.8%)
4: Total: 1570(36.2%) Separate: 331(7.6%) Overlapped: 1239(28.5%) unindexed: 164 (3.8%)

Refinements of the respective orientation matrices provided the following UB matrix relationships:
Rot(UB1,UB2)= 179.6639° around -0.00 1.00 -0.01 (rec) -0.13 0.99 -0.09 (dir)
Rot(UB1,UB3)= 179.8775° around -0.00 1.00 -0.00 (rec) -0.10 0.99 -0.02 (dir)
Rot(UB1,UB4)= 0.8306° around 0.02 -0.07 1.00 (rec) 0.35 -0.01 0.94 (dir)
Rot(UB2,UB3)= 2.6005° around -0.88 0.35 0.31 (rec) -1.00 0.01 0.02 (dir)
Rot(UB2,UB4)= -179.7055° around -0.00 1.00 -0.01 (rec) -0.09 0.99 -0.11 (dir)
Rot(UB3,UB4)= -179.9004° around 0.00 1.00 -0.00 (rec) -0.06 0.99 -0.09 (dir)

Data integration based on the two major domains provided the best reflection file when only the first domain was considered. Structure solution and refinement using the intensities from this domain were conducted using suite Olex2-1.5 (OlexSys Ltd. 20042023) software. Structure solution was achieved by the program ShelXT, while refinements were based on the least-squares method by the program ShelXL [50]. All atoms except hydrogens were refined anisotropically, with occupancy factors fixed at 1. Free occupancy refinements provided analogous values, indicating that no missing linkers/metal defects can be detected from the available data. Hydrogen atoms were fixed in idealized positions by appropriate AFIX commands. Residual electron densities could be recognized around the heavy atoms, likely due to the relatively poor quality of the extracted intensities due to the complex twinning. Such residues reasonably oscillate around 0, having a maximum peak at 1.7 and a minimum hole at -1.6 electrons/$Å^3$.

One major component accounted for around 61% of the harvested maxima. The obtained crystalline structure from SXRD, represented in Fig. 4.6b, with unit cell parameters of a = 3.98762 Å, b = 7.5698 Å, and c = 23.5895 Å, is in line with the structure from DFT optimization indicating a quasi-2D inorganic building unit in the MOF structure. It is observed that the structural parameters of the predicted Cu-S-BDC MOF (I) configuration closely match the experimentally obtained data, exhibiting minor variations ranging from a decrease of approximately 0.27% to an increase of up to 1.26%.

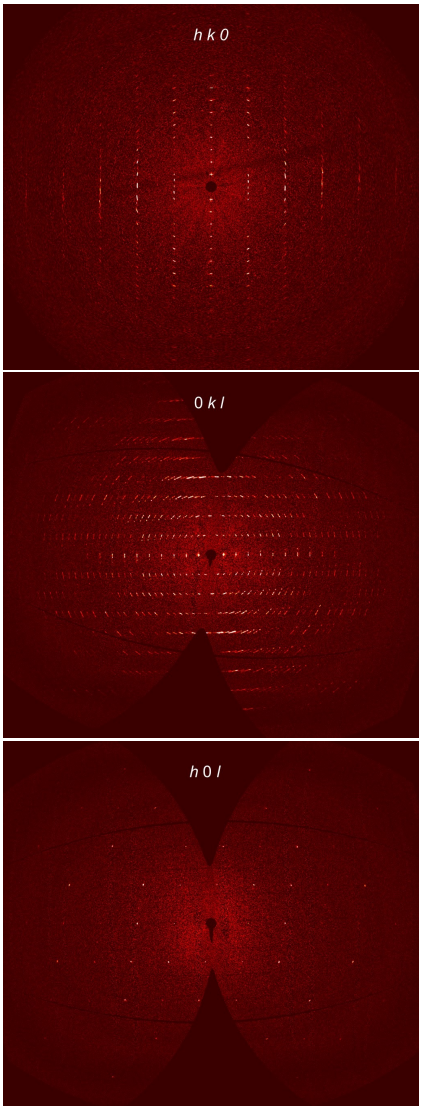

Figure 4.5: he main slabs of the reciprocal space (hk0, h0l, 0kl) reconstructed from the data based on the main orientation matrix (no symmetry averaging or slab thickness was used).

As per the structural analysis derived from SCXRD, Cu-S-BDC MOF forms in the P21/c space group, featuring unit cells containing five Cu^+ cations (Supplementary Table 4.2). Each Cu^+ cation displays a trigonal coordination environment with two S-CH_3 from reduced DMSO, and an oxygen atom from the BDC linker. The higher concentration of DMSO in the synthetic mixture, results in increased presence of sulphur-containing compounds in the Cu coordination environment. Therefore, as it

can be seen in the structure in Fig. 4.6b, carboxylate groups in the BDC linker exhibit bridging coordination mode for the chain of Cu-S-CH_3 formed roughly along the *c* axis. Thus, the synthesized MOF represents a novel Cu-S-BDC MOF framework featuring a quasi-2D inorganic building unit.
The average structure model derived from SCXRD was utilized for a subsequent powder X-ray diffraction (PXRD) simulation. As depicted in Fig. 4.6c, the simulation closely aligns with the experimental PXRD data obtained from Cu-S-BDC MOF powder, indicating a high level of agreement. The observed shifts in peak positions, especially pronounced at higher angles of 2θ, can be attributed to the SCXRD data collection conducted at 100K. Any additional peaks observed could stem from impurities or structural alterations occurring at low temperatures. The main PXRD peaks correspond to *d*-spacings of 11.5 Å, 5.8 Å, and 3.9 Å, which are associated with the (0n0) planes as indicated in the graph.

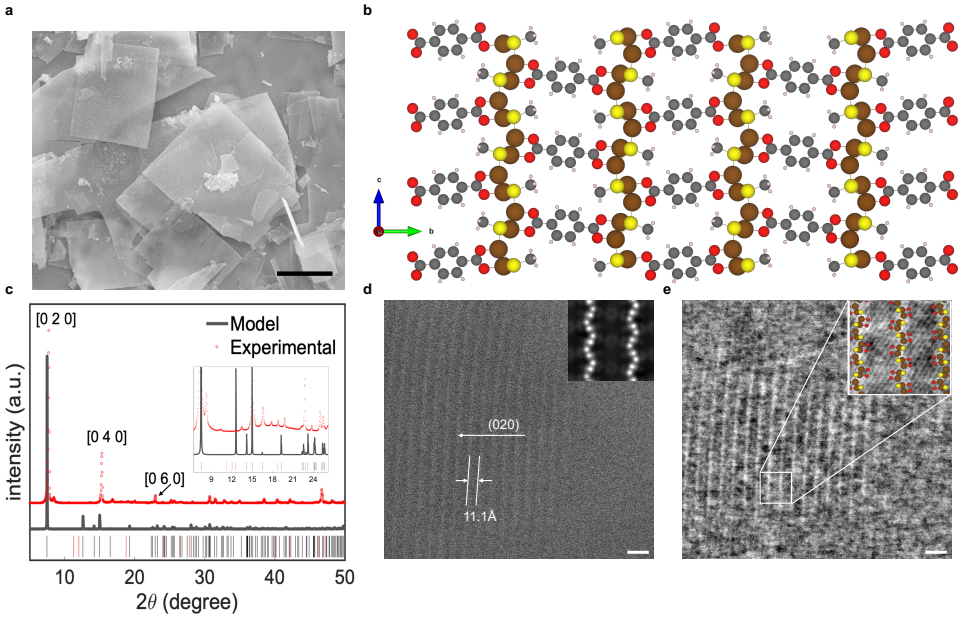

Figure 4.6: Structural Characterization and determination: **a**, SEM image of as-synthesized Cu-S-BDC MOF powder, scale bar, 10 μm **b**, Structure of Cu-S-BDC MOF simulated based on the single crystal XRD data exhibiting the formation of (-Cu-S-) plane along the *c* axis. The color scheme represents Cu (brown), S (yellow), C (gray), O (red) **c**, PXRD patterns of Cu-S-BDC MOF powder obtained from the experiment in red and model in black. Reflection positions are indicated by black and red ticks below the main plot, where black lines represent observed reflections and red lines denote missing reflections. **d**, HAADF-TEM image of the Cu-S-BDC showing the main plane of the MOF crystal (020) with d-spacing$_{020}$ of 11.1 Å. Scale bar, 2 nm. Inset, simulated HAADF-TEM of [1 0 0] direction, perpendicular to (020) planes. **e**, STEM-TEM image of the same zone as **d**. Scale bar, 2 nm. Inset, zoomed-in image of the area within the white square, including the MOF structure at [1 0 0] direction.

The high crystallinity of the MOF powder is evident in both the high-angle annular dark-field transmission electron microscopy (HAADF-TEM) and scanning transmission electron microscopy (STEM) images depicted in Fig. 4.6d and e. Due to the presence of organic components, the sample displays sensitivity to damage induced by the electron beam. Nonetheless, measured *d*-spacing, shown in Fig. 4.6d, is in good agreement with the *d*-spacing of the (020) planes. Moreover, the simulated HADDF image of the structure mirrors the pattern observed in the experimental image. The atomic arrangement of Cu-S-BDC MOF along the [1 0 0] direction, perpendicular to (020) planes, is also depicted in the inset of Fig. 4.6e. Notably, the lines depicted in the STEM image correspond to the O-Cu-S chain. Another orientation of the crystal was also investigated using STEM, perpendicular to the (031) planes with d-spacing of 5.6 Å. Fig. 4.7 represents zone [0 7 -20] of the Cu-S-BDC crystal and O-Cu-S planes are well visible.

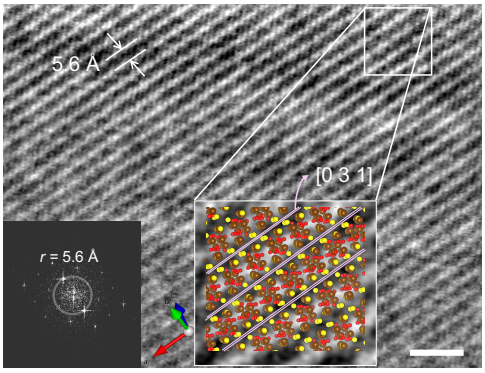

Figure 4.7: STEM image of Cu-S-BDC MOF with d_{031} = 5.6 Å. Scale bar, 5 nm. Inset: bottom right is the zoomed-in image of the region within the white square together with the structure of Cu-S-BDC MOF oriented perpendicular to the (031). The purple lines are (031) planes. The bottom left is the Fourier transform of the image, showing the *d*-spacing of 5.6 Å.

The Raman spectrum (Fig. 4.8a) exhibits peaks at 438 cm^{-1} and 272 cm^{-1}, corresponding to Cu-S, [57] which further confirms the formation of crystal I, generated by DFT optimization shown in Fig. **??**b(I). The peaks observed at 98 cm^{-1} and 141 cm^{-1} are associated with the Cu-O bonds, while the remaining peaks indicated in the graph in black originate from the BDC linker. [58, 59]. Additionally, the X-ray photoelectron spectroscopy (XPS) survey shows the expected elements only, i.e. Cu, C, O, and S (Fig. 4.8b). High-resolution XPS results of Cu2p (Fig. 4.8c) show $Cu2p_{3/2}$ sub-peak at 933.1 eV attributed to Cu-bonding with S-CH_3 [60], whereas the peak at 935.3 eV corresponds to Cu-bonding to BDC linker through oxygen [54]. The sub-peak area ratios of Cu-S/Cu-O are calculated to be 71.91/28.08 = 2.56, which closely matches the expected coordination environment of Cu within the MOF structure. A small shift of 0.5 eV for both sub-peaks to higher binding energies suggests the charging effect induced by the presence of organic linkers. On the other hand, the S2p spectrum (Fig. 4.8d) displays two main peaks, confirming

sulfur bonding with a metal, i.e., Cu, appearing at higher binding energies. The peak at 163.6 eV represents both $2p_{3/2}$ and $2p_{1/2}$ signals of S-CH_3 [61], Notably, the C-S interaction can also be discerned in the C1s spectrum (Supplementary Fig. 4.8e). The sub-peak at 284.8 eV is attributed to C=C/C-C and C-H bondings originating from the benzene ring. The sub-peaks at 287.9 eV and 288.8 eV are related to C-S and C-O, respectively. [62, 63]

Table 4.2: Crystallographic data and structure refinement of Cu-S-BDC MOF, derived from SCXRD

Chemical formula	$Cu_4C_{10}H_{10}O_4S_2$
Formula weight	512.46
Temperature/K	100
Crystal system	monoclinic
Space group	P 21/c
a/Å	3.98762
b/Å	23.5895
c/Å	7.5698
β/°	98.690(3)
Volume/Å^3	703.88(5)
Z	2
ρ_{calc}/g.cm^{-3}	2.418
μ /mm^{-1}	4.891
F(000)	500.0
Crystal size/mm^3	0.050×0.050×0.010
Radiation	Synchrotron (λ=0.650)
2θ range for data collection/°	5.896 to 47.918
Index range	-4 ≤ h ≤ 4, -29 ≤ k ≤ 29, -9 ≤ l ≤ 9
Reflections collected	9278
Independent reflections	1346 [R_{int} = 0.0848, R_{sigma} = 0.0529]
Data/restraints/parameters	1346/0/93
Goodness-of-fit on F^2	1.001
Final R indexes [l≥2δ (l)]	R_1 = 0.0605, wR_2 = 0.1570
Final R indexes [all data]	R_1 = 0.0754, wR_2 = 0.1687
Largest diff. peak/hole/ eÅ^{-3}]	1.87/-1.49

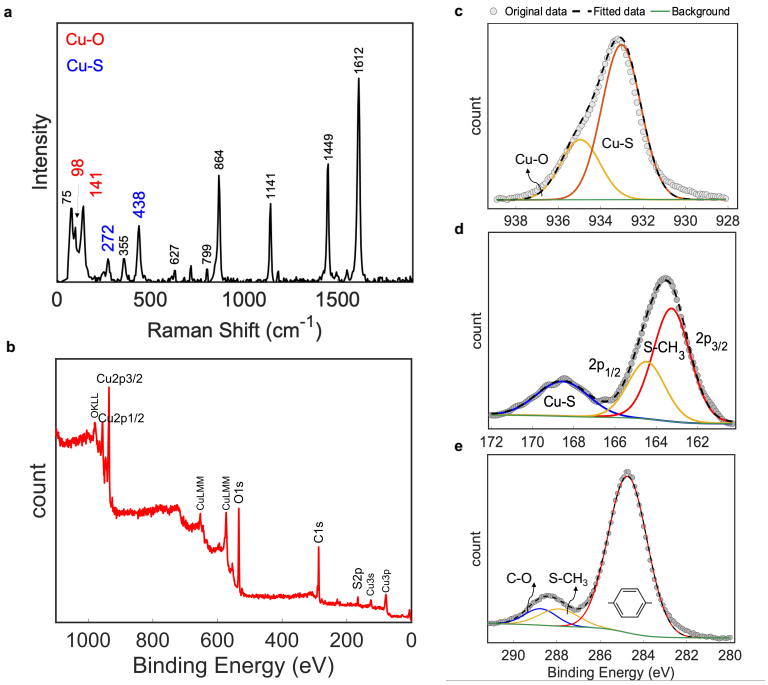

Figure 4.8: Surface characterization: **a**, The Raman spectrum of Cu-S-BDC MOF. **b**, XPS survey spectrum of the as-synthesized Cu-S-BDC MOF. XPS high-resolution spectra of **c** Cu2p, **d** S2p, and **e**, C1s; with peak fittings, labeled with the corresponding bonds. The dashed curve represents the sum of fitted peaks, and the gray dots are the measured peaks.

4.4. Electrochemical Characterizations and Reaction Mechanism

The electrocatalytic performance of the Cu-S-BDC MOF was assessed using linear sweep voltammetry (LSV) in a 1 M aqueous KOH electrolyte within a flow cell setup (Fig. 4.2). Additionally, LSV results for conventional Cu-BDC are presented in Fig. 4.9a for a comparison. LSV measurements were conducted in saturated electrolytes within the potential range of 0.5 to -1 V versus the reversible hydrogen electrode (RHE). It can be seen that the Cu-S-BDC MOF presents a more cathodic activity than Cu-BDC, favouring reduction reactions. Notably, an increase in the reductive current density of the Cu-S-BDC MOF under a CO_2 atmosphere, compared to that under an Ar atmosphere, becomes evident starting from 0 V vs. RHE. As previously reported [19], the standard reduction potential for CO_2RR products generally begins at around 0.2 V vs. RHE, while the reduction of CO_2 to formate in an alkaline environment occurs at approximately +0.2 V vs. RHE. This aligns with the observed activity of the Cu-S-BDC catalyst at lower potentials. A comparison of the LSV results of Cu-S-BDC MOF obtained in Ar- and CO_2- saturated gases indicates an overpotential of -0.46 V vs RHE for the Ar-saturated one, attributed to the hydrogen evolution reaction, whereas

Cu-S-BDC MOF can convert CO_2 at lower potentials. Furthermore, LSV graphs of Cu-S-BDC generally exhibit significantly higher catalytic activity compared to Cu-BDC MOF, attributable to higher conductivity. To dive further into the electrical properties of the proposed Cu-S-BDC MOF structure, electrochemical impedance spectroscopy (EIS) measurements were conducted in CO_2-saturated 1 M KOH for both Cu-S-BDC and Cu-BDC MOFs at OCP. Fig. 4.9b shows a lower charge transfer resistance (Rct) of approximately 40 Ω for Cu-S-BDC compared to that of Cu-BDC appearing around 60 Ω, indicating an improved conductivity due to the incorporation of sulphur in the form of Cu-S planes.

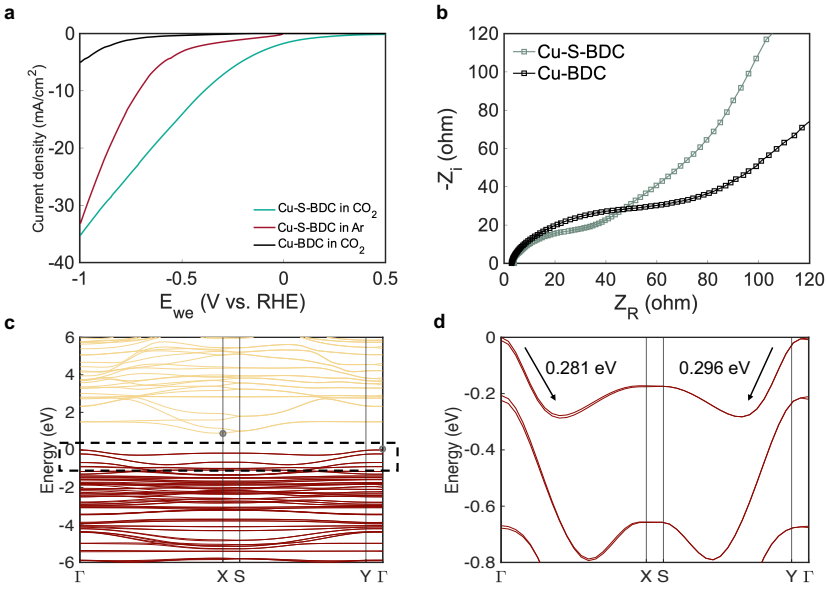

Figure 4.9: Electrochemical performance: a, LSV performance of the Cu-S-BDC MOF in Ar and CO_2 and Cu-BDC in CO_2 in 1M KOH in a flow cell, with a scan rate of 50 mV/s **b**, EIS Nyquist plots of Cu-S-BDC and Cu-BDC MOFs obtained in CO_2-saturated 1 M KOH solution. **c**, Electronic band structure and **d**, an expanded plot within the black dashed box in **c** showing the steep dispersion of the valence bands

Furthermore, the electronic band structure of Cu-S-BDC MOF was computed and depicted in Fig. 4.9c. The calculated electronic band gap is estimated through the energy difference between the valence band maximum (VBM) and the conduction band minimum (CBM). The computed band structure indicates that the narrowest electronic bandgap is 1.203 eV which occurs at the Γ (VBM) and X (CBM) points (gray dots in Fig. 4.9c). It is noteworthy that semiconductor MOFs typically exhibit flat band lines [64–70], characterized by bands with less than 0.05 eV dispersion widths, due to minimal orbital overlap caused by weak hybridization of the orbitals in the metal nodes and organic linkers. However, the synthesized Cu-S-BDC MOF exhibits a unique band structure with a marked steep dispersion, as indicated in Fig. 4.9d.

Specifically, the VBM shows a relatively flat trend along the XS and Y-Γ paths, but a steep decline along the Γ-X and -YS directions. The energy differences at the VBM between Γ-X and Y-S are 0.281 eV and 0.296 eV, respectively, as shown in the expanded Fig. 4.9d. [65, 67, 71]. The steep dispersion in the VBM is a clear sign of the unique charge transport properties, in particular, the extraordinary conductivity along $\Gamma - X$ and Y-S directions compared to other directions of the Cu-S-BDC MOF. This observation provides compelling evidence that higher conduction values occur in the direction along the Cu-S plane. Specifically, as the dispersion deviates from a flat profile to a sudden steep decrease, the effective mass of charge becomes lighter, consequently enhancing hole mobility and increasing electrical conductivity.

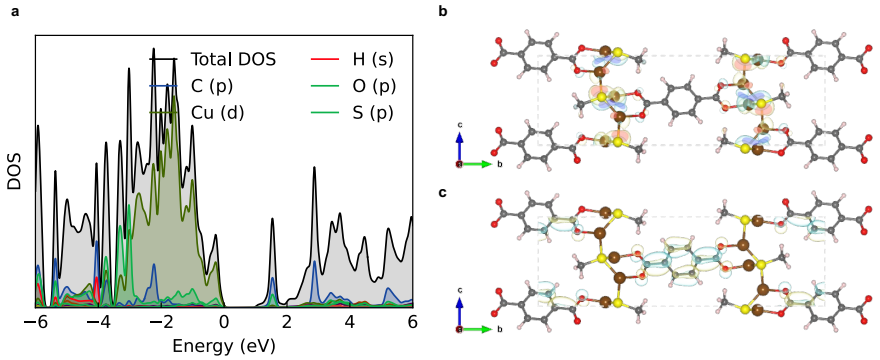

Figure 4.10: (a), Total DOS (black line) and the PDOS (other colored lines) of Cu-S-BDC MOF. The zero energy is set to the Fermi level. **(b,c)**, The isosurface of the band decomposed partial charge density of the valence band maximum (VBM) on the top and conduction band minimum (CBM) on the bottom. The charge accumulation and depletion regions are represented by pink and blue, respectively, and 0.13×10^{-3} e/Å^{-3} has been set as the isosurface value. In combination with the PDOS, band-decomposed partial charge density plots show that the VBM is mainly decomposed of the states of Cu and S, and the Cu-S plane generates a highly dense pathway for charge transport through it.

The analysis of total and partial density of states (DOSs), as depicted in Fig. 4.10a, indicates that both valence and conduction bands are composed of states from Cu, C, H, O, and S atoms. The orbital-decomposed density of state data reveals that the VBM largely consists of the states of Cu atoms with 3d-orbital, with some contributions from the states of S (3p-orbital), and with nearly negligible contributions from states of the other elements in the ligand. Moreover, the CBM predominantly consists of carbon atom states, with a minor contribution from oxygen atoms, and even less from copper and sulphur atoms. Hydrogen atoms have an almost negligible impact on both the VBM and CBM near the Fermi energy level. We have also provided the band-decomposed partial charge density for the VBM and CBM in Supplementary Fig. 4.10b,c. These plots reveal that the VBM is primarily formed by the states of Cu and S, with the Cu-S plane providing a dense route for charge conduction.

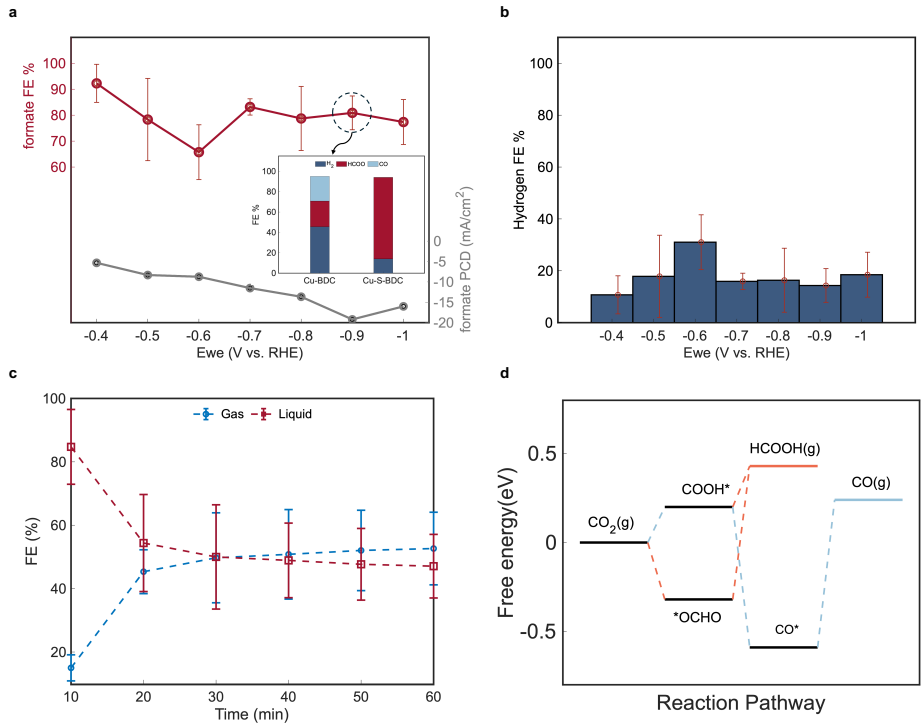

Figure 4.11: Product anlysis a: FE of Cu-S-BDC MOF powder deposited on GDE substrate in different potentials vs RHE. The black line shows the trend of the partial current density. Inset: Calculated FE values of Cu-BDC and Cu-S-BDC MOFs. The measurements were performed at -0.9 V vs. RHE in 1 M KOH under CO_2 flow **b**, The reaction pathway for CO and HCOOH formation on Cu-S-BDC MOF surface in the absence of an external potential (U = 0 eV). **c**, FE of hydrogen for Cu-S-BDC electrocatalyst in different potentials conducted in 1 M KOH electrolyte and **d**, H_2 and $HCOO^-$ Faradaic efficiency (FE) variations with time at -0.9 V vs RHE.

The flow cell shown in Fig. 4.2 coupled with gas chromatography (GC) was used to analyse the CO_2RR products of the Cu-S-BDC MOF catalyst. The measurements were conducted at different applied potentials between -0.4 and -1 V vs. RHE in CO_2-saturated 1 M KOH solution, at room temperature and under atmospheric pressure. Cu-S-BDC MOF shows selectivity towards formate only, in all studied potentials (Fig. 4.11a) whereas H_2 is the sole detected gas product (Fig. 4.11b). Inset Fig. 4.11a presents a comparison of the CO_2RR products of Cu-S-BDC and Cu-BDC MOFs. While Cu-S-BDC MOF shows a FE ($HCOO^-$) of ≈80%, Cu-BDC MOF has a total FE of 49%, divided into FE($HCOO^-$) of 25% and FE(CO) of 24%. This represents a substantial improvement in formate selectivity for Cu-S-BDC MOF, highlighting the crucial role of sulphur in the coordination environment of copper. The highest faradaic efficiency of Cu-S-BDC MOF for formate is 92% ± 7.3% at a relatively low overpotential of -0.4 V vs RHE. In contrast, metallic copper in various

polycrystalline nanostructures deposited on GDEs, under the same potential range and electrolyte conditions, has been reported to produce a variety of gas and liquid products, including CH_4, C_2H_2, and others [72]. The results also reveal that the partial current density (PCD) of formate increases with the cathodic overpotential, thereby corroborating the findings of the LSV results depicted in Fig. 4.9a. Specifically, at more cathodic potentials, the current responses of the catalyst in different media tend to converge, as water molecules increasingly engage with the active sites and drive higher HER. Conversely, the maximum PCD observed for formate is -19.2 mA cm^{-2} at the potential of -0.9 V vs RHE, which subsequently decreases at -1 V vs. RHE.

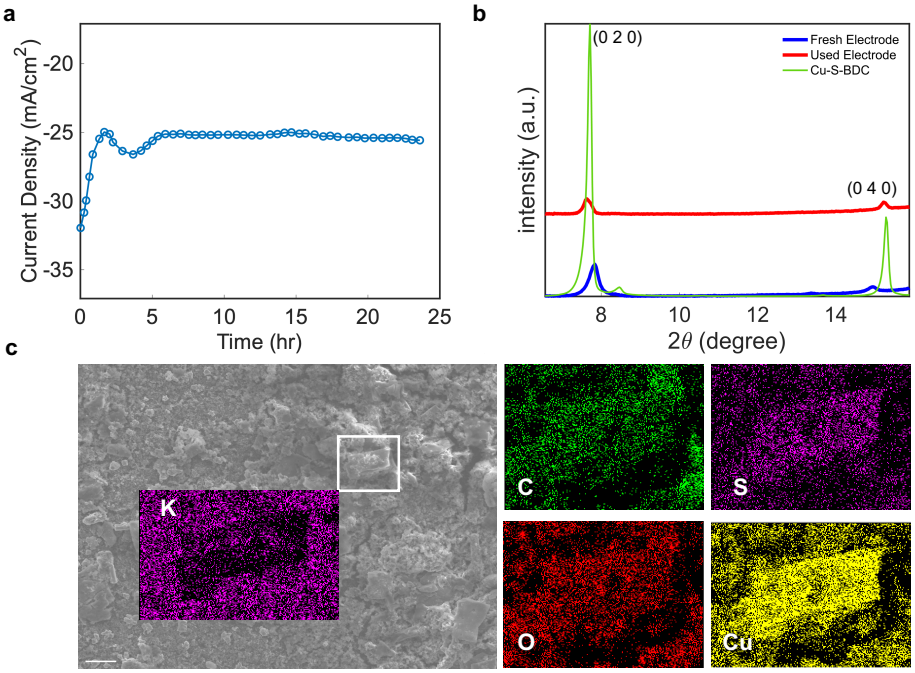

Figure 4.12: a, Chronoamperometry test conducted for the Cu-S-BDC MOF in 1 M KOH at a potential of -0.9 V vs RHE in the flow cell, with CO_2 purged at a flow rate of 20 ml/min. The current density exhibits relative stability at this potential throughout the 24-hour trial. **b**,PXRD pattern of fresh electrode, used electrode after CO_2RR in 1 M KOH at -0.9 V vs. RHE together with PXRD of powder Cu-S-BDC for better detection of main planes of the MOF crystal and, **c**, SEM and EDS images of the Cu-S-BDC MOF coated on the GDE after long-term chronoamperometry. The MOF flakes are visible in their original shape, and all the elements present in the pristine MOF are identified. inset SEM: Elemental mapping within the white square shows the presence of potassium from KOH, of the electrolyte, a sign of flooding of the GDE during electrolysis.

The trend of averaged FE(COOH) and FE(H_2) over time from different product analysis trials (Fig. 4.11c) at constant potentials of -0.4 and -0.9 V vs. RHE indicates that the majority of formate production occurs within the first ten minutes of the

reaction. This can be attributed to the initially high concentration of CO_2 molecules and the surface saturation of active sites, which gradually diminishes as the reaction proceeds. Additionally, continuous formation of formate, a liquid product that remains dissolved in the electrolyte reservoir, can gradually lead to electrolyte saturation and potentially shift the local reaction equilibrium, thereby hindering further formate production.

To further elucidate the underlying CO_2RR mechanism, we constructed models and conducted DFT studies to calculate the reaction energy on Cu-S-BDC MOF. The possible reaction pathways indicate that the production of formate occurs through two distinct pathways: via HCOO* or COOH* [19, 73–75]. The concerted proton-electron transfer (CPET) mechanisms governing the electrochemical reduction of CO_2 to HCOOH and CO. Upon CO_2^* adsorption onto the Cu-S-BDC catalyst surface, the initial CPET step can yield two distinct intermediates, HCOO* or *COOH, contingent on whether the coordination occurs via an oxygen or carbon atom. Subsequently, the second CPET step results in the formation of either HCOOH or CO. We have calculated the Gibbs free energy changes (ΔG) associated with the elementary steps leading to HCOOH and CO production. For HCOOH, these steps include the CPET process that transforms the adsorbed CO_2^* into an oxygen-coordinated intermediate ($CO_2^* + H^* + e^- \rightarrow HCOO^*$, ΔG_{HCOO^*}) followed by another CPET step converting HCOO* into gas phase formic acid ($HCOO^* + H^* + e^- \rightarrow HCOOH$, ΔG_{HCOOH}). In the case of CO formation, the elementary steps involve the CPET reaction converting adsorbed CO_2^* into a carbon-coordinated intermediate ($CO_2^* + H^* + e^- \rightarrow COOH^*$, ΔG_{COOH^*}), followed by a subsequent CPET step that converts COOH* to adsorbed carbon monoxide ($COOH^* + H^+ + e^- \rightarrow CO^* + H_2O$, ΔG_{CO^*}). The final step entails the desorption of CO* from the Cu-S-BDC catalyst surface, resulting in the release of gas-phase CO (ΔG_{CO}). As shown in Fig. 4.11d, the Cu-S-BDC catalyst surface favors the formation of the HCOO* intermediate, thus inhibiting the *COOH pathway. The free-energy diagrams in Fig. 4.10b clearly indicate that HCOO* is the key intermediate for formate production. The potential-limiting step is identified as the second CPET processconversion of HCOO* to HCOOHwith a calculated theoretical overpotential of 0.27 V.

The stability of the catalyst was also investigated with chronoamperometry (CA) for 24 hours at a constant potential of -0.9 V vs. RHE in 1 M KOH (Fig. 4.12a). The recorded current of -25.79 mA cm^{-2} remained relatively constant over 24 hours, indicating no significant deterioration or poisoning of the active sites during the measurement period. In addition, the morphology and elemental composition of the catalyst after long-term CA measurement remained unchanged (Fig. 4.12b,c). The XRD spectrum of the Cu-S-BDC crystal remains the same after CA measurement at -0.9 V vs. RHE, which is an additional demonstration of the stability of the MOF structure following electrochemical reaction. This indicates that by integrating the BDC linker into the coordination environment of Cu, we have successfully stabilized the Cu(I)-S active sites under the potential, extending stability. This is a key benefit of embedding the Cu(I)-S planes as catalytic active sites within the MOF structure, compared to non-MOF structures, generally exhibiting a lower stability. In this case, Cu-S-BDC MOF demonstrates the highest stability among Cu-S-based electrocatalysts, to the

best of our knowledge. Notably, given the proven evidence of catalyst stability, the observed drop in FE(COOH) (Fig. 4.11d) is mirrored by an equivalent rise in hydrogen FE at both potentials, strongly suggesting that flooding in the GDE-based electrolyzer reduces CO_2 availability at the catalyst surface, as previously reported [76].

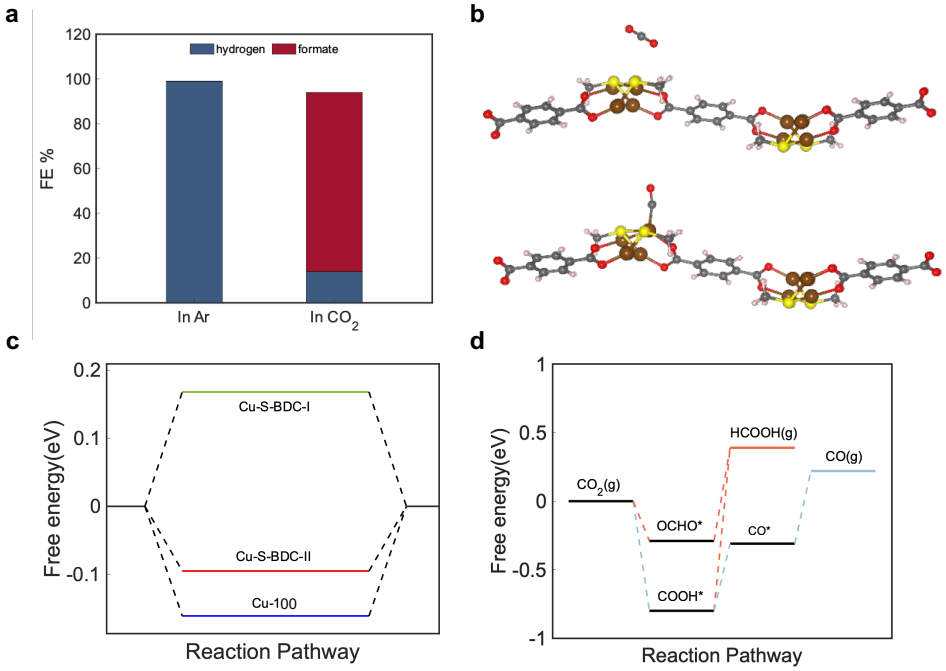

Figure 4.13: a, Faradaic efficiency of the electrolyzer products measured while Ar and CO_2 were purged into the flow cell at a potential of -0.9 V vs RHE in 1 M KOH. It is evident that the only product in Ar-saturated media is H_2, which refutes the decomposition of the Cu-S-BDC MOF. **b**, Optimized Cu-S-BDC structure in the presence of CO_2 (top), and CO molecules (bottom). It can be seen that CO_2 gets adsorbed to Cu-S. Also, CO, if formed, could change the structure of the Cu-S-BDC MOF which can potentially cause CO adsorption. **c**, Gibbs free energies of H^* adsorbed on Cu-S-BDC MOF-I and II and Cu(100). The Cu-S-BDC-II MOF exhibits a significantly higher theoretical HER overpotential of approximately 0.17 V. This value is notably greater than that of our synthesized Cu-S-BDC MOF, which has an HER overpotential of 0.11 V, and Cu (100), with an HER overpotential of 0.15 V. **d**, Reaction energy for CO and formate formation on the Cu-S-BDC-II MOF.

Furthermore, as illustrated in Fig. 4.13a, no carbon products were observed when an Ar flow was used instead of CO_2. This confirms that the organic linker remains stable at the studied cathodic potential and the detected formate is not a result of BDC decomposition. The optimized structure of Cu-S-BDC with the HCOO* intermediate shows that the CO_2 molecule is adsorbed onto the surface through both of its oxygen atoms. Additionally, the formation of CO is hindered by the strong binding affinity of CO to the Cu-S-BDC surface, evidenced by a binding energy of -0.79 eV (Fig. 4.13b).

To better understand the influence of the copper-sulphur bond on the reaction mechanism, we also investigated the CO_2RR pathway on Cu-S-BDC structure II (Fig. **??**b), which features a reduced concentration of sulphur and a rearranged configuration of Cu and S atoms. As demonstrated in Fig. **??**c, the binding strength of H* on the Cu atoms is increased in this configuration, thereby limiting the CPET step required for formate production. Our computational results indicate that the formation of both formate and CO is thormodynamically favorable on the Cu-S-BDC-II MOF (Fig. 4.13d) while strong binding of H* to the Cu atoms in structure II makes the formation of HCOOH challenging. Conversely, in our synthesized Cu-S-BDC MOF, the presence of sulphur in the Cu coordination environment results in weaker hydrogen binding on the catalyst surface, thus promoting favorable conditions for formate formation.

4.5. CONCLUSION

We have redesigned the structure of Cu-BDC MOF by introducing sulfur into its framework. The resulting Cu-S-BDC MOF features a planar structure of Cu-S units, exhibiting excellent selectivity for formate production as the sole detectable carbon product in a wide potential range. In contrast, Cu-BDC MOF produces both formate and carbon monoxide. The mechanism underlying this improvement involves a higher occupancy of Cu coordination sites by sulfur, as opposed to carbon, resulting in increased selectivity. Additionally, compared to Cu-BDC MOF, Cu-S-BDC MOF demonstrates improved current density, thanks to its planar Cu-S structure, as quasi-2D inorganic building units, that facilitate charge transfer. Our findings highlight the potential of MOFs as atomically dispersed electrocatalysts for CO_2RR, demonstrating their capacity to simultaneously enhance both selectivity and conductivity, the latter having traditionally been a limiting factor in their applications in electrochemical processes.

REFERENCES

[1] M. Li, H. Wang, W. Luo, P. C. Sherrell, J. Chen, and J. Yang. "Heterogeneous single-atom catalysts for electrochemical CO_2 reduction reaction". In: *Advanced Materials* 32.34 (2020), p. 2001848.

[2] X. Chen, J. Chen, N. M. Alghoraibi, D. A. Henckel, R. Zhang, U. O. Nwabara, K. E. Madsen, P. J. Kenis, S. C. Zimmerman, and A. A. Gewirth. "Electrochemical CO_2-to-ethylene conversion on polyamine-incorporated Cu electrodes". In: *Nature Catalysis* 4.1 (2021), pp. 20–27.

[3] S. Zhang, P. Kang, and T. J. Meyer. "Nanostructured tin catalysts for selective electrochemical reduction of carbon dioxide to formate". In: *Journal of the American Chemical Society* 136.5 (2014), pp. 1734–1737.

[4] J. Ding, H. Bin Yang, X.-L. Ma, S. Liu, W. Liu, Q. Mao, Y. Huang, J. Li, T. Zhang, and B. Liu. "A tin-based tandem electrocatalyst for CO_2 reduction to ethanol with 80% selectivity". In: *Nature Energy* 8.12 (2023), pp. 1386–1394.

[5] J. W. Blake, V. Konderla, L. M. Baumgartner, D. A. Vermaas, J. T. Padding, and J. Haverkort. "Inhomogeneities in the Catholyte Channel Limit the Upscaling of CO_2 Flow Electrolysers". In: *ACS Sustainable Chemistry & Engineering* 11.7 (2023), pp. 2840–2852.

[6] D. Gao, H. Zhou, F. Cai, J. Wang, G. Wang, and X. Bao. "Pd-containing nanostructures for electrochemical CO_2 reduction reaction". In: *Acs Catalysis* 8.2 (2018), pp. 1510–1519.

[7] Y. Chen, X.-Y. Li, Z. Chen, A. Ozden, J. E. Huang, P. Ou, J. Dong, J. Zhang, C. Tian, B.-H. Lee, *et al.* "Efficient multicarbon formation in acidic CO_2 reduction via tandem electrocatalysis". In: *Nature nanotechnology* (2023), pp. 1–8.

[8] J. Y. 'T. Kim, C. Sellers, S. Hao, T. P. Senftle, and H. Wang. "Different distributions of multi-carbon products in CO_2 and CO electroreduction under practical reaction conditions". In: *Nature Catalysis* 6.12 (2023), pp. 1115–1124.

[9] D.-H. Nam, P. De Luna, A. Rosas-Hernández, A. Thevenon, F. Li, T. Agapie, J. C. Peters, O. Shekhah, M. Eddaoudi, and E. H. Sargent. "Molecular enhancement of heterogeneous CO_2 reduction". In: *Nature materials* 19.3 (2020), pp. 266–276.

[10] H. Xu, D. Rebollar, H. He, L. Chong, Y. Liu, C. Liu, C.-J. Sun, T. Li, J. V. Muntean, R. E. Winans, *et al.* "Highly selective electrocatalytic CO_2 reduction to ethanol by metallic clusters dynamically formed from atomically dispersed copper". In: *Nature Energy* 5.8 (2020), pp. 623–632.

[11] X. Li, X. Wu, X. Lv, J. Wang, and H. B. Wu. “Recent advances in metal-based electrocatalysts with hetero-interfaces for CO_2 reduction reaction”. In: *Chem Catalysis* (2022).

[12] W. Yang, K. Dastafkan, C. Jia, and C. Zhao. “Design of electrocatalysts and electrochemical cells for carbon dioxide reduction reactions”. In: *Advanced Materials Technologies* 3.9 (2018), p. 1700377.

[13] Q. Lu and F. Jiao. “Electrochemical CO_2 reduction: Electrocatalyst, reaction mechanism, and process engineering”. In: *Nano Energy* 29 (2016), pp. 439–456.

[14] B. Zhang, Y. Jiang, M. Gao, T. Ma, W. Sun, and H. Pan. “Recent progress on hybrid electrocatalysts for efficient electrochemical CO_2 reduction”. In: *Nano Energy* 80 (2021), p. 105504.

[15] Y. Y. Birdja, E. Pérez-Gallent, M. C. Figueiredo, A. J. Göttle, F. Calle-Vallejo, and M. T. Koper. “Advances and challenges in understanding the electrocatalytic conversion of carbon dioxide to fuels”. In: *Nature Energy* 4.9 (2019), pp. 732–745.

[16] Y. Hori, K. Kikuchi, and S. Suzuki. “Production of CO and CH4 in electrochemical reduction of CO_2 at metal electrodes in aqueous hydrogencarbonate solution”. In: *Chemistry letters* 14.11 (1985), pp. 1695–1698.

[17] F. Li, Y. C. Li, Z. Wang, J. Li, D.-H. Nam, Y. Lum, M. Luo, X. Wang, A. Ozden, S.-F. Hung, *et al.* “Cooperative CO_2-to-ethanol conversion via enriched intermediates at molecule–metal catalyst interfaces”. In: *Nature Catalysis* 3.1 (2020), pp. 75–82.

[18] D. Cheng, Z.-J. Zhao, G. Zhang, P. Yang, L. Li, H. Gao, S. Liu, X. Chang, S. Chen, T. Wang, *et al.* “The nature of active sites for carbon dioxide electroreduction over oxide-derived copper catalysts”. In: *Nature communications* 12.1 (2021), p. 395.

[19] R. Kortlever, J. Shen, K. J. P. Schouten, F. Calle-Vallejo, and M. T. Koper. “Catalysts and reaction pathways for the electrochemical reduction of carbon dioxide”. In: *The journal of physical chemistry letters* 6.20 (2015), pp. 4073–4082.

[20] D. Voiry, H. S. Shin, K. P. Loh, and M. Chhowalla. “Low-dimensional catalysts for hydrogen evolution and CO_2 reduction”. In: *Nature Reviews Chemistry* 2.1 (2018), p. 0105.

[21] A. A. Peterson and J. K. Nørskov. “Activity descriptors for CO_2 electroreduction to methane on transition-metal catalysts”. In: *The Journal of Physical Chemistry Letters* 3.2 (2012), pp. 251–258.

[22] J. Pérez-Ramírez and N. López. “Strategies to break linear scaling relationships”. In: *Nature Catalysis* 2.11 (2019), pp. 971–976.

[23] T. Shinagawa, G. O. Larrazábal, A. J. Martín, F. Krumeich, and J. Pérez-Ramírez. “Sulfur-modified copper catalysts for the electrochemical reduction of carbon dioxide to formate”. In: *ACS Catalysis* 8.2 (2018), pp. 837–844.

[24] J. S. Yoo, R. Christensen, T. Vegge, J. K. Nørskov, and F. Studt. “Theoretical insight into the trends that guide the electrochemical reduction of carbon dioxide to formic acid”. In: *ChemSusChem* 9.4 (2016), pp. 358–363.

[25] C. H. van Oversteeg, M. T. Rosales, K. H. Helfferich, M. Ghiasi, J. D. Meeldijk, N. J. Firet, P. Ngene, C. de Mello Donegá, and P. E. de Jongh. "Copper sulfide derived nanoparticles supported on carbon for the electrochemical reduction of carbon dioxide". In: *Catalysis Today* 377 (2021), pp. 157–165.

[26] Y. Deng, Y. Huang, D. Ren, A. D. Handoko, Z. W. Seh, P. Hirunsit, and B. S. Yeo. "On the role of sulfur for the selective electrochemical reduction of CO_2 to formate on CuS_x catalysts". In: *ACS applied materials & interfaces* 10.34 (2018), pp. 28572–28581.

[27] L. Majidi, A. Ahmadiparidari, N. Shan, S. N. Misal, K. Kumar, Z. Huang, S. Rastegar, Z. Hemmat, X. Zou, P. Zapol, *et al.* "2D copper tetrahydroxyquinone conductive metal-organic framework for selective CO_2 electrocatalysis at low overpotentials". In: *Advanced Materials* 33.10 (2021), p. 2004393.

[28] J. Liu, D. Yang, Y. Zhou, G. Zhang, G. Xing, Y. Liu, Y. Ma, O. Terasaki, S. Yang, and L. Chen. "Tricycloquinazoline-based 2D conductive metal-organic frameworks as promising electrocatalysts for CO_2 reduction". In: *Angewandte Chemie International Edition* 60.26 (2021), pp. 14473–14479.

[29] M. Bonneau, C. Lavenn, J.-J. Zheng, A. Legrand, T. Ogawa, K. Sugimoto, F.-X. Coudert, R. Reau, S. Sakaki, K.-i. Otake, *et al.* "Tunable acetylene sorption by flexible catenated metal-organic frameworks". In: *Nature Chemistry* 14.7 (2022), pp. 816–822.

[30] C. A. Downes and S. C. Marinescu. "Electrocatalytic metal–organic frameworks for energy applications". In: *ChemSusChem* 10.22 (2017), pp. 4374–4392.

[31] L. Sun, M. G. Campbell, and M. Dinc. "Electrically conductive porous metal–organic frameworks". In: *Angewandte Chemie International Edition* 55.11 (2016), pp. 3566–3579.

[32] L. S. Xie, G. Skorupskii, and M. Dinc. "Electrically conductive metal–organic frameworks". In: *Chemical reviews* 120.16 (2020), pp. 8536–8580.

[33] L. Sun, T. Miyakai, S. Seki, and M. Dinc. "Mn2 (2, 5-disulfhydrylbenzene-1, 4-dicarboxylate): a microporous metal–organic framework with infinite (-Mn–S-)∞ chains and high intrinsic charge mobility". In: *Journal of the American Chemical Society* 135.22 (2013), pp. 8185–8188.

[34] A. Pathak, J.-W. Shen, M. Usman, L.-F. Wei, S. Mendiratta, Y.-S. Chang, B. Sainbileg, C.-M. Ngue, R.-S. Chen, M. Hayashi, *et al.* "Integration of a (-Cu-S–)n plane in a metal organic framework affords high electrical conductivity". In: *Nature communications* 10.1 (2019), p. 1721.

[35] P. Ayala, S. Naghdi, S. P. Nandan, S. N. Myakala, J. Rath, H. Saito, P. Guggenberger, L. Lakhanlal, F. Kleitz, M. C. Toroker, *et al.* "The Emergence of 2D Building Units in Metal-Organic Frameworks for Photocatalytic Hydrogen Evolution: A Case Study with COK-47". In: *Advanced Energy Materials* 13.31 (2023), p. 2300961.

[36] J. Barthel. “Dr. Probe: A software for high-resolution STEM image simulation”. In: *Ultramicroscopy* 193 (2018), pp. 1–11. ISSN: 0304-3991. DOI: https://doi.org/10.1016/j.ultramic.2018.06.003. URL: https://www.sciencedirect.com/science/article/pii/S0304399118301402.

[37] G. Kresse and J. Hafner. “Ab initio molecular dynamics for open-shell transition metals”. In: *Physical Review B* 48.17 (1993), p. 13115.

[38] G. Kresse and J. Furthmüller. “Efficiency of ab-initio total energy calculations for metals and semiconductors using a plane-wave basis set”. In: *Computational materials science* 6.1 (1996), pp. 15–50.

[39] G. Kresse and J. Furthmüller. “Efficient iterative schemes for ab initio total-energy calculations using a plane-wave basis set”. In: *Physical review B* 54.16 (1996), p. 11169.

[40] J. P. Perdew, K. Burke, and M. Ernzerhof. “Generalized gradient approximation made simple”. In: *Physical review letters* 77.18 (1996), p. 3865.

[41] P. E. Blöchl. “Projector augmented-wave method”. In: *Physical review B* 50.24 (1994), p. 17953.

[42] M. Methfessel and A. Paxton. “High-precision sampling for Brillouin-zone integration in metals”. In: *physical review B* 40.6 (1989), p. 3616.

[43] G. Henkelman, A. Arnaldsson, and H. Jónsson. “A fast and robust algorithm for Bader decomposition of charge density”. In: *Computational Materials Science* 36.3 (2006), pp. 354–360.

[44] Q. Gong, P. Ding, M. Xu, X. Zhu, M. Wang, J. Deng, Q. Ma, N. Han, Y. Zhu, J. Lu, *et al.* “Structural defects on converted bismuth oxide nanotubes enable highly active electrocatalysis of carbon dioxide reduction”. In: *Nature communications* 10.1 (2019), p. 2807.

[45] A. Klinkova, P. De Luna, C.-T. Dinh, O. Voznyy, E. M. Larin, E. Kumacheva, and E. H. Sargent. “Rational design of efficient palladium catalysts for electroreduction of carbon dioxide to formate”. In: *Acs Catalysis* 6.12 (2016), pp. 8115–8120.

[46] R. Christensen, H. A. Hansen, and T. Vegge. “Identifying systematic DFT errors in catalytic reactions”. In: *Catalysis Science & Technology* 5.11 (2015), pp. 4946–4949.

[47] J. K. Nørskov, J. Rossmeisl, A. Logadottir, L. Lindqvist, J. R. Kitchin, T. Bligaard, and H. Jonsson. “Origin of the overpotential for oxygen reduction at a fuel-cell cathode”. In: *The Journal of Physical Chemistry B* 108.46 (2004), pp. 17886–17892.

[48] A. R. Oganov, A. O. Lyakhov, and M. Valle. “How Evolutionary Crystal Structure Prediction Works and Why”. In: *Accounts of chemical research* 44.3 (2011), pp. 227–237.

[49] A. O. Lyakhov, A. R. Oganov, H. T. Stokes, and Q. Zhu. “New developments in evolutionary structure prediction algorithm USPEX”. In: *Computer Physics Communications* 184.4 (2013), pp. 1172–1182.

[50] G. M. Sheldrick. “Crystal structure refinement with SHELXL”. In: *Acta Crystallographica Section C: Structural Chemistry* 71.1 (2015), pp. 3–8.

[51] C. G. Carson, K. Hardcastle, J. Schwartz, X. Liu, C. Hoffmann, R. A. Gerhardt, and R. Tannenbaum. *Synthesis and structure characterization of copper terephthalate metal–organic frameworks*. 2009.

[52] D. Head and C. McCarty. “The thermal decomposition of DMSO”. In: *Tetrahedron Letters* 14.16 (1973), pp. 1405–1408.

[53] M. Sajjad, M. B. Tahir, I. Mubeen, and M. R. Kabli. “Tailorable and rationally designed MoS_2 based heterostructure photocatalyst for efficient photocatalytic degradation of phenol under the visible light”. In: *Journal of Inorganic and Organometallic Polymers and Materials* 30 (2020), pp. 3965–3972.

[54] G. Zhan, L. Fan, F. Zhao, Z. Huang, B. Chen, X. Yang, and S.-f. Zhou. “Fabrication of Ultrathin 2D Cu-BDC Nanosheets and the Derived Integrated MOF Nanocomposites”. In: *Advanced Functional Materials* 29.9 (2019), p. 1806720.

[55] R. S. Salama, S. El-Hakam, S. Samra, S. El-Dafrawy, A. Ahmed, *et al.* “Adsorption, equilibrium and kinetic studies on the removal of methyl orange dye from aqueous solution by using of copper metal organic framework (Cu-BDC)”. In: *Int. J. Modern Chem* 10.2 (2018), pp. 195–207.

[56] T. Ghanbari, F. Abnisa, and W. M. A. W. Daud. In: *Science of The Total Environment* 707 (2020), p. 135090.

[57] S. H. Chaki, J. Tailor, and M. Deshpande. “Covellite CuS-Single crystal growth by chemical vapour transport (CVT) technique and characterization”. In: *Materials science in semiconductor processing* 27 (2014), pp. 577–585.

[58] L. Sun, Y. Zhao, Y. Shang, C. Sun, and M. Zhou. “The phase stability of terephthalic acid under high pressure”. In: *Chemical Physics Letters* 689 (2017), pp. 56–61.

[59] L. Debbichi, M. Marco de Lucas, J. Pierson, and P. Kruger. “Vibrational properties of CuO and Cu_4O_3 from first-principles calculations, and Raman and infrared spectroscopy”. In: *The Journal of Physical Chemistry C* 116.18 (2012), pp. 10232–10237.

[60] I. Mínguez-Bacho, M. Courté, C. Shi, and D. Fichou. “Controlling the nanomorphology of thin conformal Cu2S overlayers grown on Cu_2O compact layers and nanowires”. In: *Materials Letters* 159 (2015), pp. 47–50.

[61] P. M. Shanthi, P. J. Hanumantha, K. Ramalinga, B. Gattu, M. K. Datta, and P. N. Kumta. “Sulfonic acid based complex framework materials (CFM): nanostructured polysulfide immobilization systems for rechargeable lithium-sulfur battery”. In: *Journal of The Electrochemical Society* 166.10 (2019), A1827.

[62] G. Zheng, Z. Xing, X. Gao, C. Nie, Z. Xu, and Z. Ju. “Fabrication of 2D Cu-BDC MOF and its derived porous carbon as anode material for high-performance Li/K-ion batteries”. In: *Applied Surface Science* 559 (2021), p. 149701.

[63] C. He, C. Liu, M. Li, M. Li, J. Yin, S. Han, J. Xia, D. Chen, W. Cao, Q. Lu, *et al.* "3D hierarchical Cu-MOF nanosheets-based antibacterial mesh". In: *Chemical Engineering Journal* 446 (2022), p. 137381.

[64] M. Usman, S. Mendiratta, S. Batjargal, G. Haider, M. Hayashi, N. Rao Gade, J.-W. Chen, Y.-F. Chen, and K.-L. Lu. "Semiconductor behavior of a three-dimensional strontium-based metal–organic framework". In: *ACS applied materials & interfaces* 7.41 (2015), pp. 22767–22774.

[65] E. A. Dolgopolova, A. J. Brandt, O. A. Ejegbavwo, A. S. Duke, T. D. Maddumapatabandi, R. P. Galhenage, B. W. Larson, O. G. Reid, S. C. Ammal, A. Heyden, *et al.* "Electronic properties of bimetallic metal-organic frameworks (MOFs): tailoring the density of electronic states through MOF modularity". In: *Journal of the American Chemical Society* 139.14 (2017), pp. 5201–5209.

[66] A. S. Duke, E. A. Dolgopolova, R. P. Galhenage, S. C. Ammal, A. Heyden, M. D. Smith, D. A. Chen, and N. B. Shustova. "Active sites in copper-based metal-organic frameworks: understanding substrate dynamics, redox processes, and valence-band structure". In: *The Journal of Physical Chemistry C* 119.49 (2015), pp. 27457–27466.

[67] S. S. Park, E. R. Hontz, L. Sun, C. H. Hendon, A. Walsh, T. Van Voorhis, and M. Dinc. "Cation-dependent intrinsic electrical conductivity in isostructural tetrathiafulvalene-based microporous metal–organic frameworks". In: *Journal of the American Chemical Society* 137.5 (2015), pp. 1774–1777.

[68] M. L. Aubrey, B. M. Wiers, S. C. Andrews, T. Sakurai, S. E. Reyes-Lillo, S. M. Hamed, C.-J. Yu, L. E. Darago, J. A. Mason, J.-O. Baeg, *et al.* "Electron delocalization and charge mobility as a function of reduction in a metal–organic framework". In: *Nature materials* 17.7 (2018), pp. 625–632.

[69] T. Hu, W. Zhong, T. Zhang, W. Wang, and Z. Wang. "Identifying topological corner states in two-dimensional metal-organic frameworks". In: *Nature Communications* 14.1 (2023), p. 7092.

[70] B. G. Diamond, L. I. Payne, and C. H. Hendon. "Ligand field tuning of d-orbital energies in metal-organic framework clusters". In: *Communications Chemistry* 6.1 (2023), p. 67.

[71] K. T. Butler, C. H. Hendon, and A. Walsh. "Electronic structure modulation of metal–organic frameworks for hybrid devices". In: *ACS Applied Materials & Interfaces* 6.24 (2014), pp. 22044–22050.

[72] G. L. De Gregorio, T. Burdyny, A. Loiudice, P. Iyengar, W. A. Smith, and R. Buonsanti. "Facet-dependent selectivity of Cu catalysts in electrochemical CO_2 reduction at commercially viable current densities". In: *ACS catalysis* 10.9 (2020), pp. 4854–4862.

[73] M. Van den Bossche, C. Rose-Petruck, and H. Jonsson. "Competing HCOOH and CO pathways in CO_2 electroreduction at copper electrodes: calculations of voltage-dependent activation energy". In: *The Journal of Physical Chemistry C* 125.25 (2021), pp. 13802–13808.

[74] Z. Yang, H. Wang, X. Fei, W. Wang, Y. Zhao, X. Wang, X. Tan, Q. Zhao, H. Wang, J. Zhu, *et al.* “MOF derived bimetallic CuBi catalysts with ultra-wide potential window for high-efficient electrochemical reduction of CO_2 to formate”. In: *Applied Catalysis B: Environmental* 298 (2021), p. 120571.

[75] B. Ren, G. Wen, R. Gao, D. Luo, Z. Zhang, W. Qiu, Q. Ma, X. Wang, Y. Cui, L. Ricardez–Sandoval, *et al.* “Nano-crumples induced Sn-Bi bimetallic interface pattern with moderate electron bank for highly efficient CO_2 electroreduction”. In: *Nature Communications* 13.1 (2022), p. 2486.

[76] P. Gonugunta, K. Roohi, M. Soleimani, P. R. Anusuyadevi, P. Taheri, and M. Ramdin. “Screening of Binder Materials for Ag-Based Gas Diffusion Electrodes for CO_2 Conversion to CO”. In: *Industrial & Engineering Chemistry Research* (2025).

5

TAILORING COPPER COORDINATION FOR ENHANCED SELECTIVITY IN CO_2 REDUCTION

Abstract

*Recent advances in electrocatalyst design have intensified efforts to improve selectivity in the electrochemical CO_2 reduction reaction (CO_2RR). Among candidate materials, copper remains the most intrinsically active, yet its inability to favor a single carbonaceous product has motivated studies into the structural origins of its broad product spectrum. Here, we investigate two Cu-BDC-based (BDC = benzenedicarboxylic acid) metalorganic frameworks (MOFs) with distinct copper coordination environments of four and five oxygen atoms. Modulating the coordination number from five (Cu-BDC-5) to four (Cu-BDC-4) shifts the product distribution from CO to formate. At 1 V vs. RHE in 1 M KOH, the formate Faradaic efficiency increases from 3% on Cu-BDC-5 to 40% on Cu-BDC-4, underscoring the decisive influence of local coordination environment on selectivity. Density functional theory reveals that the square-planar CuO_4 in Cu-BDC-4 favors *OCHO formation via oxygen-end CO_2 adsorption, while the trigonal-bipyramidal CuO_5 in Cu-BDC-5 stabilizes *COOH, steering the reaction toward CO. Operando Raman spectroscopy further supports this mechanism, identifying a CuO vibration at 536 cm^{-1} as the spectroscopic fingerprint of the oxygen-bound formate intermediate. These results establish copper coordination number as a key parameter for tuning selectivity in MOF-based CO_2RR electrocatalysts.*

A revised version of this chapter *will be submitted* as a scientific manuscript:
K.Roohi, S. Mohseni Armaki, N. Khossossi, M. Soleimani, A. Lanza, S. Canossa, P. Ravi Anusuyadevi, P. Gonugunta, A. Mol, P. Dey, P. Taheri, The Role of Copper Coordination in Metal Organic Frameworks in CO_2RR Selectivity

5.1. INTRODUCTION

The rising concentration of carbon dioxide (CO_2) in the atmosphere, primarily driven by fossil fuel consumption, poses significant environmental and climate challenges [1, 2]. Projections indicate that global energy consumption will increase by 1.3 times by 2040, resulting in the emission of approximately 500 gigatons of CO_2 from fossil fuel combustion [3, 4]. This, necessitates the development of carbon-neutral technologies and alternative energy sources [5]. In this context, converting CO_2 into valuable chemicals has gained significant attention as a promising strategy to close the carbon cycle and reduce CO_2 emissions [6]. Among the various CO_2 conversion methods, electrochemical CO_2 reduction reaction (CO_2RR), powered by renewable electricity, offers notable advantages, including integration with existing industrial infrastructure [7, 8]. Electrochemical systems, with their modular design, allow for scalable and efficient CO_2 conversion, positioning them as a key technology for supporting sustainable energy solutions and industrial applications [9, 10]. However, one of the biggest challenges CO_2RR faces is low selectivity and faradaic efficiency (FE), as well as the formation of a diverse range of products, which necessitates additional post-separation processes [11, 12]. Thus, designing and engineering the electrocatalyst material no, alter the reaction pathway and result into more favourable products.

Traditional copper-based catalysts, such as metallic Cu, Cu_2O, and CuO, have demonstrated intrinsic catalytic activity for CO_2RR, yet their poor stability and low selectivity toward a single carbon-based product limit their practical application [13, 14]. The linear relationship between the binding energies of key CO_2RR intermediates (*CO, *COOH, *CHO) on the surface of transition metals further complicates the optimisation of Cu-based catalysts [15, 16]. Thus, materials capable of decoupling these energetics toward enhanced selectivity are highly desirable. Metalorganic frameworks (MOFs), with their exceptional structural tunability, offer significant advantages over conventional materials for this purpose [17–19]. Unlike metal- or metal-oxide-based electrocatalysts, MOFs enable precise engineering of the coordination environment at the metallic active sites, thereby facilitating the rational design of catalysts with enhanced performance [20].

It is well known that the coordination environment of the copper catalyst including the neighbouring atoms, coordination number and the geometery strongly influences the adsorption energies of key intermediates and thereby dictates the CO_2RR pathway [21, 22]. In such systems, the local electronic environment of the copper center modulates the binding and reactivity of the *COOH/*CO intermediate, directing the reaction toward distinct products. Consequently, variations in coordination environment of copper can shift the reaction pathway and result in notable differences in product distribution [23, 24].

This study explores the structural tuning of a copper benzenedicarboxylic acid MOF (Cu-BDC) by modulating the coordination environment of the copper centers within the framework. By controlling the coordination number, we demonstrate a clear shift in CO_2RR selectivityfrom CO to formatehighlighted by distinct surface intermediates and product distributions. Supported by in situ spectroscopic and theoretical analyses, this work showcases how precise control over local coordination geometry in MOFs can be leveraged to steer catalytic behavior. Our findings underscore the potential

of coordination-engineered MOFs as a powerful platform for selective and tunable electrochemical CO_2 reduction.

5.2. METHODOLOGY

Copper(II) nitrate ($Cu(NO_3)_2.3H_2O$, 99.999%), benzenedicarboxylic ($C_8H_6O_4$), dimethylformamide (99,999%), isopropanol and, KOH all were purchased from Sigma-Aldrich. Polytetrafluoroethylene 55 wt % dispersion in water was obtained from FUELCELL store. The gas diffusion electrodes (GDE) from FUELCELL store with the size of 6.76 cm^2 and 1 cm^2 were used as substrates for CO_2RR electrochemical measurements and In-situ Raman measurements, respectively.

MOF synthesis:

For the synthesis of Cu-BDC MOFs, $Cu(NO_3)_2$ and Terephthalic acid were combined in a 1:2 molar ratio, followed by the addition of 30 mL of water in case of Cu-BDC-4 and 30 mL 1:1 V mixture of ethanol and DMF in case of Cu-BDC-5. The mixture underwent stirring for 30 minutes to ensure complete dissolution of the precursors. Subsequently, the homogeneous mixture was carefully transferred to a 50 ml Teflon-lined stainless steel autoclave, sealed with Teflon tape. The sealed autoclave was then placed in an oven and heated to 140°C for 24 hours. Once the reaction concluded, the autoclave was cooled to room temperature and the resulting MOF crystals were collected using filter paper. To eliminate any residual unreacted precursors, the collected crystals underwent multiple wash cycles with water, DMF and ethanol. Finally, the washed crystals were air-dried at room temperature.

Electrode preparation:

Dried MOF powders were mixed with PTFE (4:1 w%) in a water and isopropanol solution (1:1 vol%) to form an ink with an active material concentration of 5 mg/mL. The ink was then dropcasted onto GDE (catalyst loading of 1.5 mg/cm^2) using a pipette and dried under ambient air.

Characterization of materials:

Powder X-ray diffraction (PXRD) was carried out with a Bruker D8 Advance diffractometer X-ray powder diffractometer equipped with a Cu-sealed tube (λ = 1.54178 Å at 45 kV and 40 mA. Scanning electron microscope (SEM) observation was performed with a field emission-scanning electron microscope (JEOL JSM-7401F or Magellan 400 XHR) equipped with electron dispersive spectroscopy (EDS). X-ray photoelectron spectroscopy (XPS) analysis was conducted using a PHI-TFA XPS spectrometer (Physical Electronic Inc.). The device is equipped with an X-ray Al-monochromatic source. The vacuum level inside the measuring chamber is maintained at 10^{-9} mbar. The analysis region measures 0.4 mm in diameter. We conducted precise multiplex scans of the peaks with a narrow focus, utilizing a pass energy of 71.55 eV and a step size of 0.1 eV. The measurements were carried out at an angle of 45° with respect to the sample surface. Spectral processing was performed using Multipak v8.0 (Physical Electronics Inc., Chanhassen, MN, USA). Elemental composition was determined from the XPS survey spectra, while high-energy resolution spectra of S2p and Cu2p, C1s and O1s photoelectron peaks were subjected to curve fitting.

A Thermo-Nicolet Nexus Fourier-transform infrared spectroscopy (FTIR) apparatus was used equipped with a liquid-nitrogen-cooled mercury cadmium tellurium detector and a nitrogen-purged measurement chamber. The Raman spectra have been achieved by WiTeC Alpha300R Raman Imaging microscope, using 532nm laser with 0.2mW laser power to avoid damaging the samples with an integration time of 8 seconds and 10 accumulations. The sample was prepared by dissolving sample powder in IPA and drop casting on quartz slides. Thermogravimetric analyses were performed using the TAG 1750 instrument manufactured by Setaram. The powders were heated from ambient temperature to 900 °C with a heating rate of 50 °C/min to mimic the sintering cycle used in the experiments. For the DSC, the powders were heated from ambient temperature up to 600 °C and back to ambient temperature with a heating and cooling rate of 5 °C/min to closely measure heat flow at each temperature step.

Crystal determination:

For structural characterization with 3D electron diffraction (3D ED), the light blue dry powder of Cu-BDC-4 was deposited on a 300-mesh copper TEM grid coated with a continuous film of ultrathin amorphous carbon (from EMS). 3D ED measurements were performed at ambient temperature and high vacuum on a Rigaku XtaLAB Synergy-ED [25], equipped with a LaB6 source operating at 200 kV (λ= 0.0251) and a Rigaku HyPix-ED detector. The diffraction patterns were collected during continuous rotation of the crystals over ca. 145°, with a width of 0.25° and an exposure time of 1 s per frame, using a selected area aperture with an apparent diameter of 2 μm. The program CrysAlisPro[26] was used to control the data collection and to process the diffraction data, for indexing, data reduction and space group determination. four crystals were examined and all showed unit cell parameters in good agreement with copper(II) hydroxy-terephthalate $Cu_2(OH)_2(C_8H_4O_4)$ [27].

Electrochemical measurements and product analysis:

A flow cell (Dioxide Materials.) with a Nafion anion exchange membrane from FORBLUE SELEMION was used for all electrochemical measurements. The working electrode was a squared GDE coated with MOF (2.6 × 2.6 cm, area, 6.76 cm^2). An Iridium plate from Magneto Special Anodes B.V. and a leak-free Ag/AgCl reference electrode (Innovative Instruments LF-1-45) were used as counter electrode and reference electrode, respectively. After IR correction, all potentials were converted into those vs. RHE. 1 and 0.5 M KOH solutions were cycled through the cathode and anode compartments, respectively with a 10 mL/min flowrate. CO_2 was bubbled from the back of the cell with a flow rate of 20 mL/min for 1.5 hours to reach the electrolyte saturation. In the case of Ar flow, the same procedure was repeated. Linear sweep voltammograms (LSV) were recorded in Ar and CO_2-saturated 1 M KOH at a scan rate of 5 mV/s. To conduct product analysis measurements, chronoamperometric measurements were conducted in 1 M KOH solution saturated with CO_2. The measurements were carried out at constant potentials of -0.5, -0.8, and -1 V versus the RHE for a duration of 30 minutes each. Samples of 1 mL were collected from the electrolyte reservoir at the end of 30 min to analyse liquid products. Gas product analysis from the cathode compartment was done with gas chromatography (GC from Agilent) equipped with two thermal conductivity detectors (TCD) to measure CO_2, CO, and H_2 in 2-minute intervals. A standard calibration curve was made using custom

gas mixture cylinders with known concentrations of product gasses in CO_2 (Linde gas Benelux B.V.). The liquid products were quantified using high-performance liquid chromatography (HPLC, Agilent 1260 Infinity). 5 μL of the liquid sample was injected into two Aminex HPX 87-H columns (Bio-rad) placed in series. The column oven temperature was maintained constant at 60 $^{\circ}C$, with a steady flow rate of 0.6 mL/min of an aqueous 1 mM H_2SO_4 eluent, and a refractive index detector (RID) was used for product detection.
Faradaic efficiencies were calculated using equation 5.1

$$\frac{n_i NF}{jt} \tag{5.1}$$

where n_i represents the number of moles of the detected product, N is the number of the transferred electrons in a reaction, F is the Faradaic constant (s A/mol), j is the current density (A) and t is the time of the measurement in seconds.

DFT Calculations:

The Density Functional Theory (DFT) computations were carried out based on the Vienna ab initio simulation package (VASP) [28–30]. The generalized gradient approximation in the form of Perdew Burke Ernzerhof (PBE) [31] functional was adopted self-consistently through the approach of the Projector Augmented Wave (PAW) [32] by Kohn-Sham electron wave functions expanded with an energy cutoff of 550 eV and the convergence criteria during the structural optimizations were set to 10^{-6} eV and 10^{-3} eV/Å for energy and force, respectively. The Monkhorst Pack K-point [33] of the $9 \times 1 \times 5$ grid is used in the reciprocal space during the geometrical optimizations. The charge transfer between atoms is evaluated based on the Bader charge algorithm [34]. The open-source package vaspkit [35] was used for the state of density and the thermodynamics (298.15 K and 1 atm) calculations. For Gibbs free energy, the following equation was used:

$$G = H - T\Delta S = E_{\mathrm{DFT}} + E_{\mathrm{ZPE}} + \int_0^{298.15} C_v \, dT - T\Delta S \tag{5.2}$$

where H refers to the enthalpy, E_{DFT} refers to the electronic adsorption energy and E_{ZPE} signifies the zero-point vibrational energy. The calculation also includes the heat capacity ($\int_0^{298.15} C_v \, dT$) and entropy correction ($T\Delta S$) as the third and fourth components, respectively, derived from frequency calculations. For the gas molecules, we referenced the data from the study by Klinkova et al. [36]. To mitigate the overestimation typically seen in DFT calculations [37, 38], these corrections were applied: CO_2 (0.45 eV), HCOOH (0.20 eV), and the adsorbed COOH* (0.20 eV). Finally, the adsorption energy was calculated through the following equations:

$$E^{ads}_{\mathrm{COOH}} = E_{\mathrm{COOH}*} - E_{\mathrm{MOF}} - (E_{\mathrm{HCOOH}} - \frac{1}{2}E_{\mathrm{H_2}}) \tag{5.3}$$

$$E^{ads}_{\mathrm{HCOO}} = E_{\mathrm{HCOO}*} - E_{\mathrm{MOF}} - (E_{\mathrm{HCOOH}} - \frac{1}{2}E_{\mathrm{H_2}}) \tag{5.4}$$

E_{MOF} and $E_{Molecule}$ refer to the ground state energy of the pristine MOF system and isolated molecule, respectively. Herein, we take the following reaction 5.5 as an example to show the calculation of Gibbs free energy variation based on the equation 5.6, where e is the charge number, and U is the external applied voltage, for the calculation of free energy of H^+ and e^-, the computational hydrogen electrode model [39] was used to calculate the Gibbs free energy of proton/electron:

$$COOH* + H^+ + e^- \leftrightarrow HCOOH^+ \tag{5.5}$$

$$\begin{aligned} \Delta G &= G_* + G_{\mathrm{HCOOH}} - G_{\mathrm{COOH}^*} - (G_{\mathrm{H}^+} + G_{e^-}) \\ &= G_* + G_{\mathrm{HCOOH}} - G_{\mathrm{COOH}^*} - \left(\frac{1}{2}G_{\mathrm{H_2}} - eU\right) \end{aligned} \tag{5.6}$$

In-situ Raman measurements

Raman spectroscopy was performed using a WiTec alpha300R Raman Imaging Microscope. To enhance the Raman signal at the interface, shell-isolated nanoparticle-enhanced Raman spectroscopy (SHINERS) was employed. Gold nanospheres (40 nm in diameter, OD20) in aqueous sodium citrate solution were purchased (AUCR40, NanoComposix) and diluted 20 times prior to use. The Au shell-isolated nanoparticles (Au-SHINs) were prepared following the method described in Reference [40]. Specifically, 0.4 mL of (3-aminopropyl) trimethoxysilane (APTMS) solution (1 mM) was mixed with 30 mL of the as-prepared gold colloid. Subsequently, 3.2 mL of sodium silicate solution (0.54 wt%) with a pH of 10 was added. The mixture was then transferred to a water bath at 95 °C and stirred for approximately 30 minutes to facilitate the formation of a 2-nm silica shell. The synthesized Au-SHINs were centrifuged twice and washed with ultrapure water. Finally, the concentrated sol was diluted with ultrapure water before application. The prepared Au-SHINs were drop-cast onto the sample surface and dried on a hot plate at 80 °C. The GDE coated with MOF samples was subsequently exposed then prepared for Raman spectroscopy measurements. For ex situ Raman measurements, a 633 nm wavelength laser was employed with a 50Œ Zeiss objective (working distance: 9.1 mm) and a laser power of 1 mW to prevent damage. For in situ measurements, the same 633 nm laser was used with a 63 Zeiss water-dipping objective (working distance: 2.4 mm) and a laser power of 5 mW. Raman spectra were collected every 10 minutes with an integration time of 20 seconds and 10 accumulations per measurement.

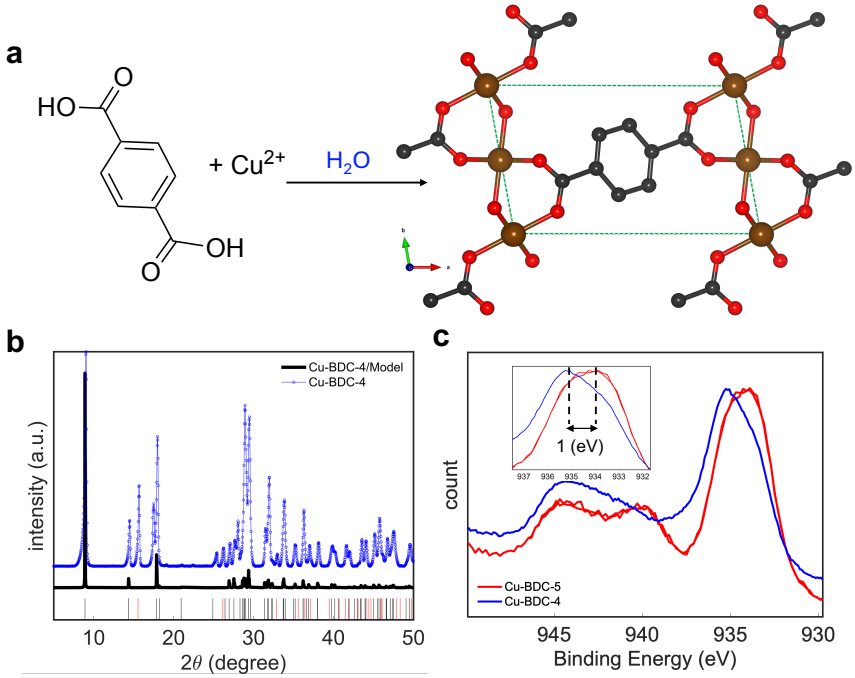

Figure 5.1: a, Synthesis precursors of the Cu-BDC-4 MOF together with its unit cells. **b**, PXRD patterns of Cu-BDC-4 MOF powder obtained from the experiment in dotted blue line and model in black. Reflection positions are indicated by black and red ticks below the main plot, where black lines represent observed reflections and red lines denote missing reflections. **c**, XPS high-resolution Cu2p spectra of Cu-BDC-4 and Cu-BDC-5 MOFs.

5.3. DESIGN OF DIFFERENT COORDINATION ENVIRONMENTS

To understand how the coordination environment of copper centers influences catalytic performance, the conventional Cu-BDC-MOF was redesigned to reduce the coordination number of Cu. As shown in Fig. 5.1a, Cu^{2+} was dissolved together with terephthalic acid in water to form Cu-BDC-4, with four oxygen atoms present in the coordination environment of Cu. This differs from Cu-BDC-5, which was synthesized in a mixture of Dimethylformamide (DMF) and Ethanol (Eth), resulting in five coordinated oxygen atoms 5.2. The detailed synthesis procedure for both MOFs is provided in the Materials and Methods section. Structural analysis, derived from electron diffraction (ED), shows that Cu-BDC-4 crystallizes in the P-1 space group, with lattice parameters listed in Table 5.1, which are consistent with previous reports [27]. The structural model obtained from ED was used for subsequent powder X-ray diffraction (PXRD) simulations. As depicted in Fig. 5.1b, the simulation closely aligns with the experimental PXRD data obtained from the Cu-BDC-4 MOF powder, indicating a high degree of agreement. Any additional peaks observed could be attributed to impurities or structural alterations occurring during the measurement. High-resolution XPS results of Cu2p-3/2 (Fig. 5.1c) of both MOFs, shows a shift of

1 eV, representing a significant difference in the local electronic environment of the Cu atoms [41]. Notably, the CuBDC4 peak appears 1 eV higher, supporting that its squareplanar Cu-O sites are more electrondeficient than in CuBDC5. The stronger CuO bonding in CuBDC4 pulls electron density away from the metal centre, giving it a greater electronaccepting character Moreover, the Cu^{2+} satellite peaks for Cu-BDC-5 demonstrate two different subpeaks, which is an indication of difference in the coordinated compounds.

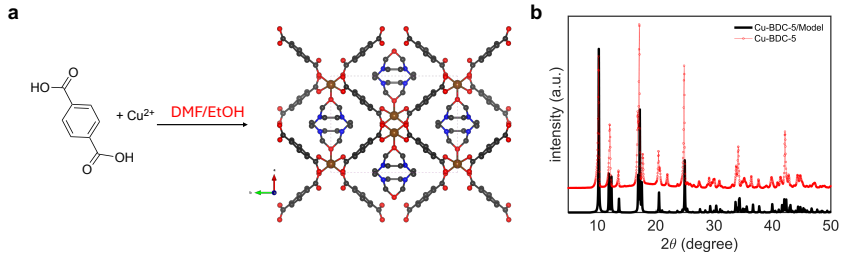

Figure 5.2: a, Synthesis precursors of Cu-BDC-5 and its unit cell. **b**, PXRD pattern of Cu-BDC-5 MOF powders together with Cu-BDC model

Table 5.1: Crystallographic data for the Cu-BDC-4 MOF

Parameter	
Empirical formula	$(C_8H_6Cu_2O_6)_n$
Formula weight	325.24
Technique	3D ED
Radiation (Å)	0.0251 (electrons)
Temperature	ambient
Symmetry	
Crystal system	triclinic
Space group	$P\bar{1}$
Unit-cell parameters	
a (Å)	3.4930(3)
b (Å)	6.3605(4)
c (Å)	10.1961(8)
α (°)	98.624(6)
β (°)	96.553(6)
γ (°)	99.263(6)
Volume (Å^3)	218.81(3)

Further morphological investigation of both MOFs shows that Cu-BDC-4 forms rod-shaped crystals with micrometer length, while Cu-BDC-5 grows in the shape of thick plates (Fig. 5.3a,c) which further concludes their different crystalline structure.

Energy dispersive spectroscopy (EDS) analyzes of both MOF samples confirm the distribution of C, O, Cu and N in the case of Cu-BDC-5 (Fig. 5.3). To better compare the structure of the two MOFs, Raman measurements were conducted on the powders. The Raman spectrum of Cu-BDC-5 (Fig. 5.4a) exhibits peaks at the Raman shifts range of 100 cm^{-1} to 144 cm^{-1} which are associated with the Cu-O bonds streching, while the remaining peaks are almost identical in peak positions for both MOFs and originate from the BDC linker. [42, 43]. The difference in peak position and distribution of peaks in zoomed in Raman from the Cu-O region (100 -140 cm^{-1}, inset of Fig. 5.4a) supports the idea of structural difference for both MOFs. Moreover, Fig. 5.4b depicts the FTIR spectra of both MOFs. The similarity of two patterns indicates the two samples have essentially identical organic-linker, therefore, the change in Cu coordination has not altered the ligand vibrations. The major peaks at wavelengths of 1392 and 1567 cm^{-1} (1606 cm^{-1} in case of Cu-BDC-5) are respectively correlated to symmetric and asymmetric stretching modes of coordinated carboxylate. The second major peak at 733 cm^{-1} (and 753 cm^{-1} in the case of Cu-BDC-5) originates from the C-H vibrational band of the aromatic ring [44]. The peaks at 465 and 562 cm^{-1} for Cu-BDC-4 and at 568 and 675 cm^{-1} for Cu-BDC-5 fall within the CuO fingerprint region [45]. The shift between these peaks reflects differences in CuO bond strength in the two MOFs.

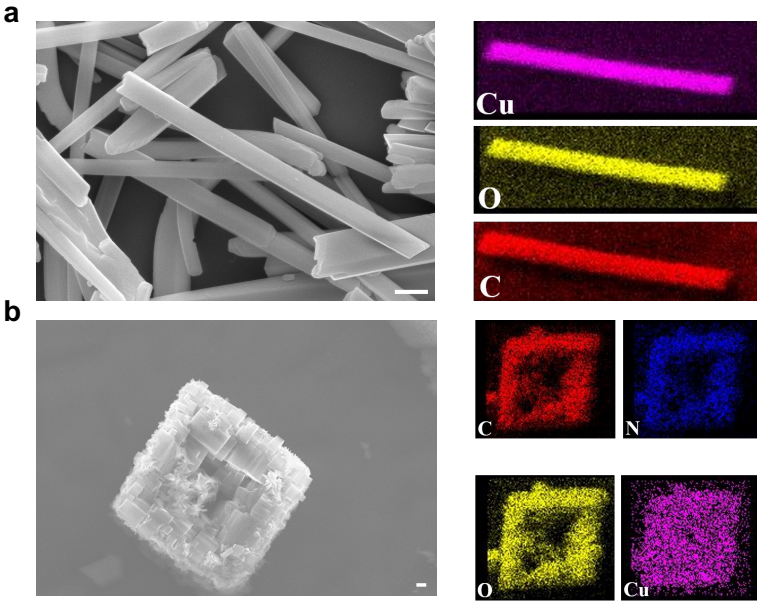

Figure 5.3: **a**, SEM image of as-synthesized Cu-BDC-4 MOF powder, and EDS pattern of MOF needels. **b**, SEM image of as-synthesized Cu-BDC-5 MOF powder, and EDS pattern of MOF cubes; Scale bar, 1 μm

Thermogravimetric analysis coupled with online MS (Fig. 5.4c) shows that both

MOFs have similar thermal stability (320 °C in line with what was reported for Cu-BDC-5 in the literature [46]), losing only 1% of their mass as physisorbed water below 120 °C. During the main decomposition step (320400 °C) Cu-BDC-5 releases 8.8 mg (47 % of its initial mass), whereas Cu-BDC-4 loses 8.0 mg (43 %), leaving larger inorganic residue in the latter. Consistently, the CO_2 and C_6H_6 (m/z 78) signals show higher intensity for Cu-BDC-5, confirming that the four-coordinate material contains less volatile organic content.

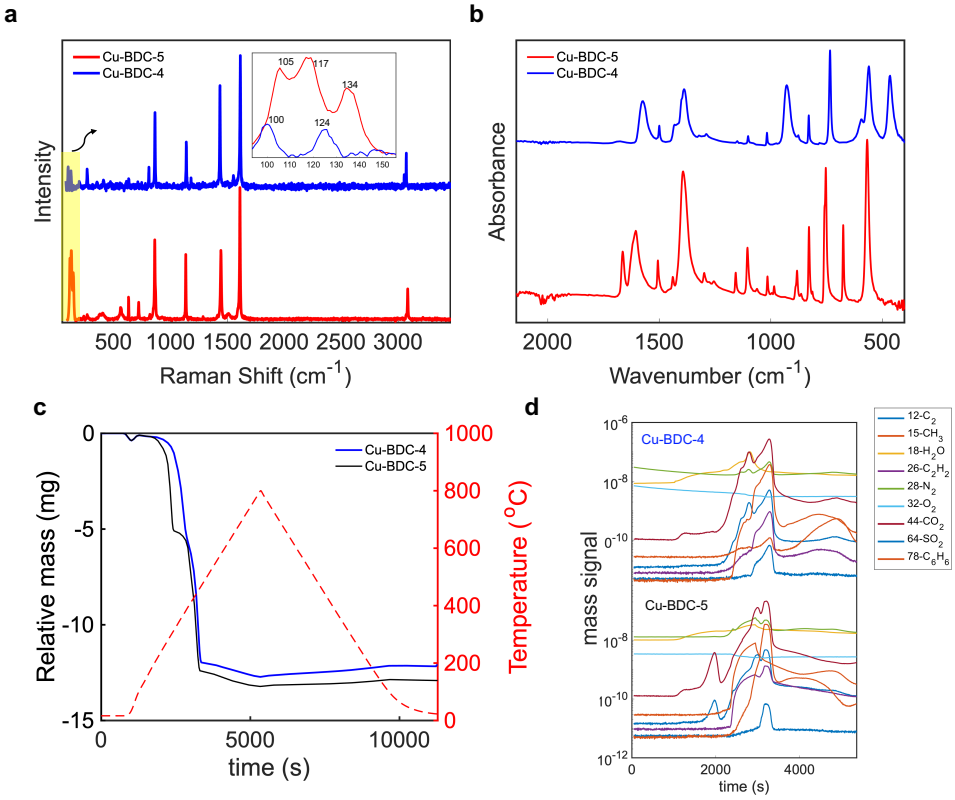

Figure 5.4: **a**, The Raman spectrum of Cu-BDC-4 and 5 and inset, zoomed in spectrum of the range that is assigned to Cu-O vibration. The peaks at 100 and 105 for both MOFs are chracterized as the lattice vibration and peaks at 117, 124 and 134 are related to Cu-O streching. **b**, FTIR spectrum of the as-synthesized Cu-BDC MOFs. **c**, TGA plot of the as-synthesized Cu-BDC MOFs and **d**, Coupled mass spectrometry with TGA reveals the compounds leaving the system at elevated temperatures.

5.4. ELECTROCHEMICAL CHARACTERIZATION AND PRODUCT ANALYSIS:

The electrocatalytic performance of Cu-BDC-4 MOF was evaluated using linear sweep voltammetry (LSV) in 1 M aqueous KOH within a flow cell setup, employing a gas diffusion electrode (GDE). Both MOF crystals were finely dispersed by sonication during ink preparation to minimize morphological differences in electrochemical performance. LSV measurements were conducted in electrolytes saturated with Ar or CO_2 in a potential range of 0.8 to -0.8 V versus RHE. Under the CO_2-saturation, Cu-BDC-4 exhibits more cathodic activity than that of the Ar-saturated electrolyte, suggesting that at more cathodic potentials, the MOF could favor the formation of carbon-based products (Fig. 5.5a). For comparison, the Cu-BDC-5 LSV pattern is presented in Fig. 5.5b, clearly indicating a preference for the hydrogen evolution reaction (HER). The small peak in Fig. 5.5a near 0 V vs. RHE in the LSV indicates a reduction process intrinsic to the Cu-BDC-4 material rather than CO_2-related reactions, as it also appears under Ar saturation.

This behavior can be attributed to partial reduction of Cu^{+2}, which is further evidenced by the increased reduction current in the forward path of the first cyclic voltammetry (CV) scan shown in Fig. 5.5c at around the same potential. The higher cathodic current on the return path of the first cycle represents the irreversibility of the catalyst transformation during the initial potential sweep, a conclusion further supported by the notable discrepancies between the first and second cycles. Moreover, this higher cathodic current on the return path of the first cycle could result from adsorbed intermediates reacting differently than in subsequent scans in the CO_2-saturated electrolyte. By the second cycle, the catalyst appears to reach a more stable state and exhibits a more consistent forwardreverse response.

A flow cell coupled with gas chromatography (GC) was used to analyse the CO_2RR products of the Cu-S-BDC MOF catalyst. The measurements were conducted at three different applied potentials in CO_2-saturated 1 M KOH solution. The results of product distribution for Cu-BDC-4 is shown in Fig. 5.5d. Formate is the dominant carbonous product, with an increasing trend over potential. Faradaic efficiency (FE) of CO remain almost constant by changing the potential and with a good agreement with LSV, CO_2RR to overcome the HER. The similar behaviour is not seen for FE results of Cu-BDC-5 as HER is the dominant reaction in the studied range of potential (see Fig. 5.5e). In addition, as the product distribution of both MOFs shows, changing the coordination number of copper in Cu-BDC- MOF from 5 to 4 could increase the selectivity of the CO_2RR towards production of formate (Fig, 5.5f).

In order to gain an initial understanding of CO_2RR mechanism, density-functional theory (DFT) calculations were carried out to compare the first proton-coupled steps on Cu-BDC-4 and Cu-BDC-5. As shown in Fig. 5.6a, the square-planar CuO polyhedron of Cu-BDC-4 exposes an open axial site that lets CO_2 adsorb through an oxygen atom. The free-energy diagram reveals that this configuration favours the HCOO* pathway: formation of HCOO* is downhill, and every subsequent step toward formate remains thermodynamically favourable, while the competing *COOH branch lies higher in energy, so CO formation is disfavoured. In contrast, Fig.

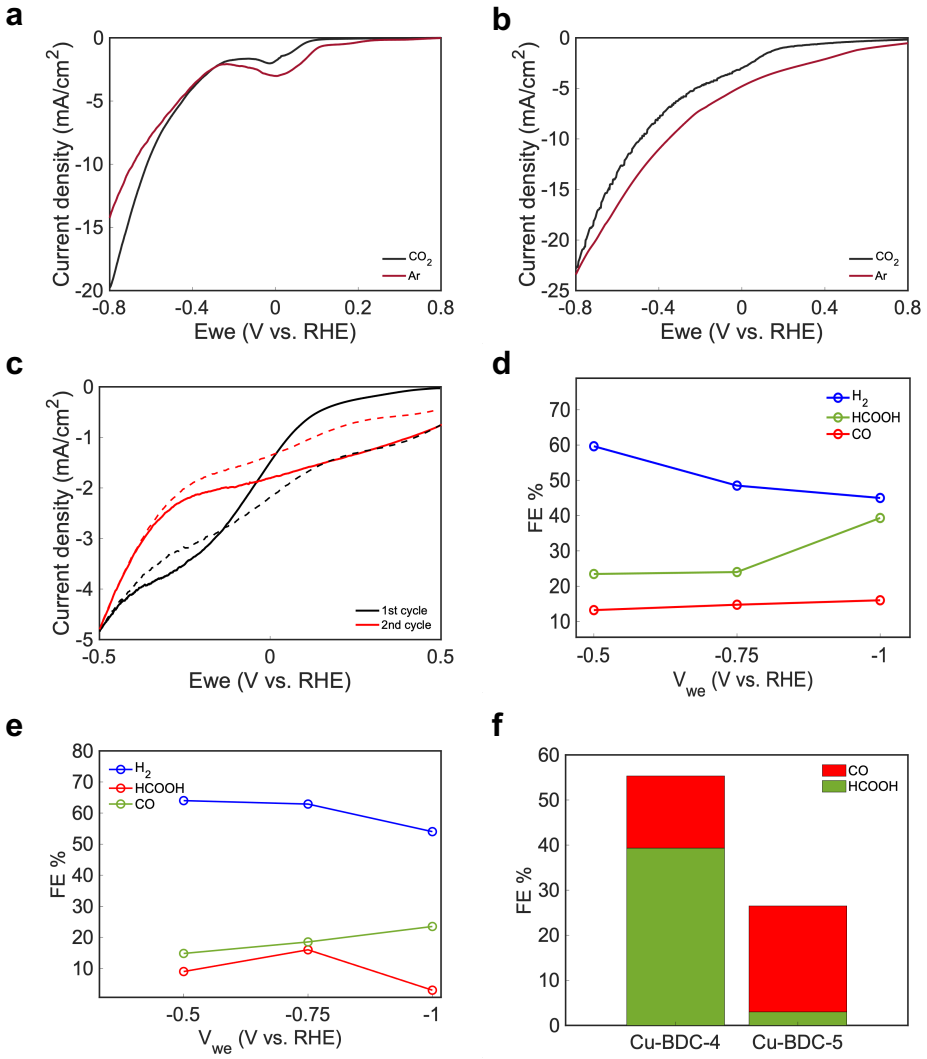

Figure 5.5: LSV performance of the **a** Cu-BDC-4 and **b**, Cu-BDC-5 MOFs, in Ar and CO_2 in 1M KOH in a flow cell, with a scan rate of 50 mV/s **c**, CV performance of Cu-BDC-4 MOF in similar condition as LSV in two sequent cycles. The solid lines and dashed lines represent the reduction and oxidation path, respectively. FE results of **d**, Cu-BDC-4 and **e**, Cu-BDC-5 MOFs powder deposited on GDE substrate in different potentials vs RHE. **f**, FE values for carbnous products on Cu-BDC-4 and -5 MOFs at -1 V vs. RHE in 1 M KOH under CO_2 flow

5.6b indicates that the trigonal-bipyramidal CuO polyhedron of Cu-BDC-5 is more crowded; CO_2 binds through its carbon atom to give *COOH, and that route traces the lowest-energy path, ultimately releasing CO, whereas the *OCHO route is uphill and therefore suppressed. These free-energy landscapes, together with the distinct coordination polyhedra, explain why Cu-BDC-4 is formate-selective, while Cu-BDC-5 mainly produces CO.

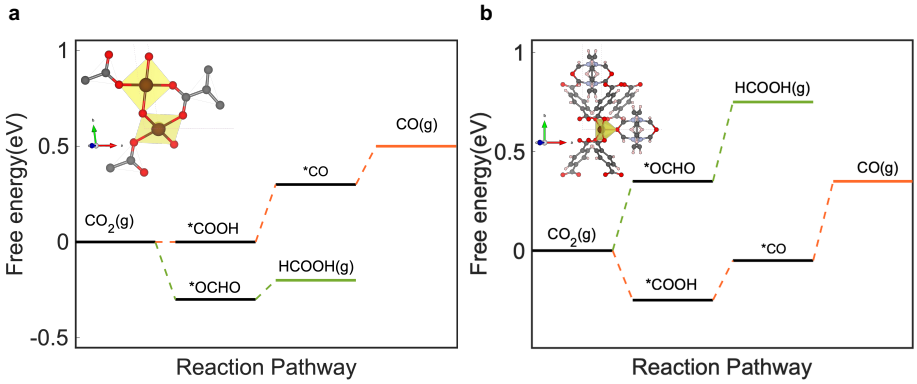

Figure 5.6: The reaction pathway for CO and HCOOH formation on **a**, Cu-BDC-4 and **b**, Cu-BDC-5 MOFs in the absence of an external potential (U = 0 eV). Dashed green and orange lines are representative of the formate and carbon monoxide production pathways, respectively. Inset, Cu-O coordination polyhedron in both MOFs.

Furthermore, Figure 5.7 compares the calculated hydrogen-evolution route on the two MOFs. The Cu-BDC-5-assigned pathway shows a lower free energy at both proton-coupled electron transfer (PCET) steps and leads to H_2 formation on an energetically downhill surface, indicating that HER is facile on this material. By contrast, the red pathway for the square-planar Cu-BDC-4 site sits higher at each stage; both the first hydrogen adsorption (*H) and the second PCET step are less favourable, so H_2 production is thermodynamically suppressed.

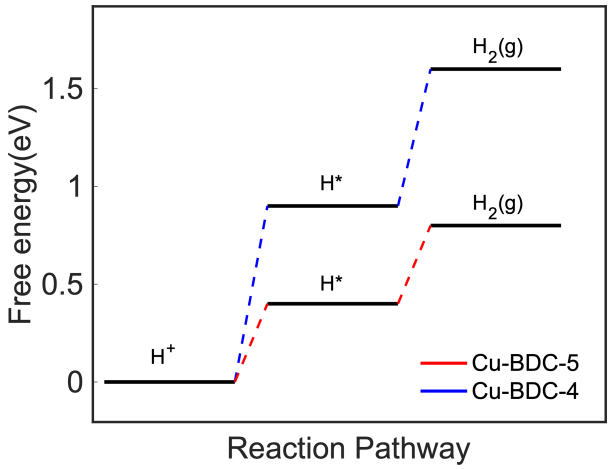

Figure 5.7: The reaction pathway for H_2 formation on Cu-BDC-4 and 5 MOFs in the absence of an external potential (U = 0 eV).

5.5. STUDY OF THE REACTION MECHANISM

In order to elucidate the underlying CO_2RR mechanism and fingerprint of the formate intermediate on the surface of a copper-based electrode, operando shell-isolated nanoparticle-enhanced Raman spectroscopy (SHINERS) was used under a working electrode potential of 0.5 V vs. RHE (Fig. 5.8a). This potential was selected to ensure a moderate reaction rate, allowing detection of intermediates. Previous studies have reported that increasing the potential leads to a reduction in Raman signal intensity for key intermediates [47]. Time-resolved measurements were carried out in 10-second intervals to track the evolution of CO_2RR intermediates throughout the course of the reaction. The electrochemical cell that was used for these measurements, was a flow cell, with CO_2 gas being purged at the back of the GDE-based working electrode to keep the operando measurements as consistent as possible with the product analysis investigation. The surface enhancement for the MOF samples to improve the Raman signal from the interface was done using silicon coated, gold nano particles (details can be found in the methods section).

The dominant peak appearing around 536 cm^{-1} is attributed to CuO bonding, consistent with previous reports on in situ Raman studies of Cu-based CO_2RR catalysts. Notably, this peak is not associated with the CuO bonds of the MOF framework itself, as its intensity increases under negative potentials. If the peak originated from structural CuO bonds, it would be expected to diminish under reducing conditions. Therefore, this peak is assigned to the CuO vibration resulting from CO_2 adsorption through the oxygen side of the molecule, aligning with the observed formate selectivity in the CO_2RR products.

As shown in Fig. 5.8b, the time evolution of the reaction reveals two additional weak peaks emerging at 298 and 386 cm^{-1}, which have been previously assigned to

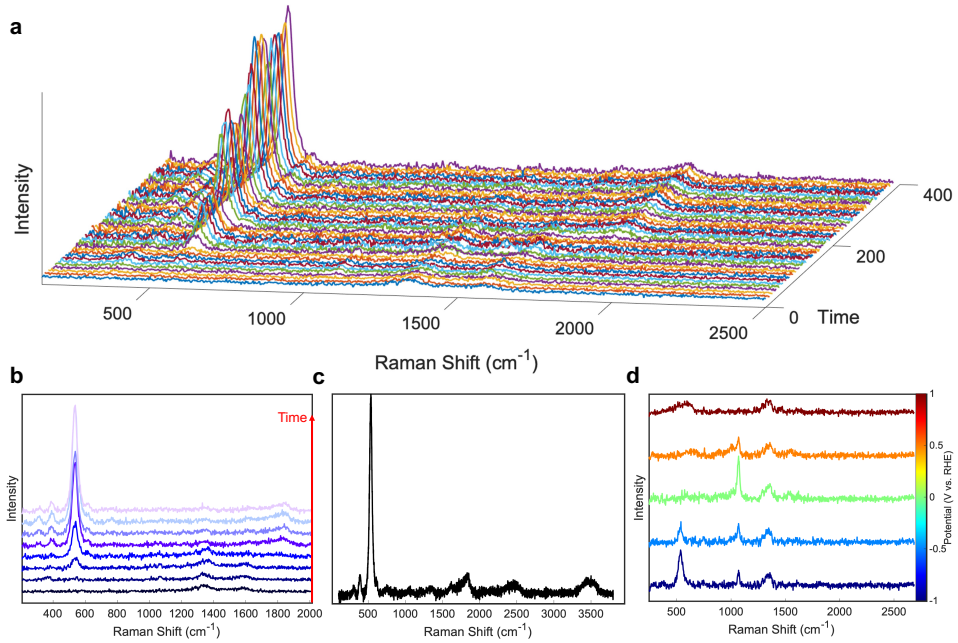

Figure 5.8: a, Three-dimensional stack of Raman spectra collected every 10 s at the interface of Cu-BDC-4 catalyst and electrolyte. **b**, Evolution of adsorbed COO* intermediate during the CO_2 reduction reaction time. **c**, High-resolution spectrum acquired at the end of the run, showing the dominant CuO vibration. All operando measurements were done at -0.5 V vs. RHE in 1 M KOH saturated with CO_2 and **d**, Potential-dependent spectra recorded at steady-state potentials from 1.0 V to +1.0 V vs. RHE.

CuCO stretching and CuCO orientation, respectively. Following the appearance of these peaks, a band at approximately 1850 cm^{-1} also develops, which may correspond to the stretching mode of adsorbed *CO species. High-resolution spectra at the end of the reaction (Fig. 5.8c) further confirm the prominence of the 536 cm^{-1} peak, supporting its assignment to the formate pathway intermediate.

To validate this assignment and rule out structural origins, Raman spectra were collected under different applied potentials (Fig. 5.8d). The results show that as the potential becomes more negative, the 536 cm^{-1} peak intensifies in CO_2-saturated electrolyte. In parallel, the 1070 cm^{-1} peakoriginating from carbonate species formed in 1 M KOHdiminishes with increasing negative bias. This suppression of carbonate, along with the enhancement of CuO vibration associated with adsorbed CO_2, suggests a shift in reaction preference toward formate production, in agreement with the Faradaic efficiency measurements.

The reliability of the observed Raman signals was further validated by performing identical operando measurements on the benchmark Cu-BDC-5 sample. As shown in Fig. 5.9, no signal appeared near 530 cm^{-1} throughout the course of the reaction, in contrast to the Cu-BDC-4 case. Instead, a strong band centered at 2070 cm^{-1} was observed, which corresponds to carbonate species formed in the alkaline electrolyte. This observation is consistent with the lower CO_2RR activity of Cu-BDC-5, as previously confirmed by product analysis. A weak band near 370 cm^{-1}, attributable to *CO, further supports CO as the dominant reduction product for this catalyst. These results reinforce the assignment of the 530 cm^{-1} band in Cu-BDC-4 to a CuO vibration associated with the oxygen-bound formate intermediate, and collectively support its role as a spectroscopic fingerprint for selective formate formation on Cu-based MOFs.

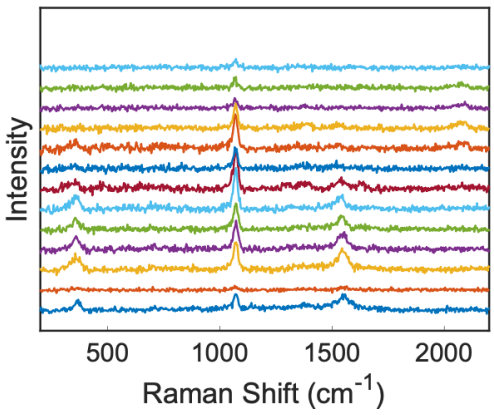

Figure 5.9: Stack of Raman spectra collected every time interval at the interface of Cu-BDC-4 catalyst and electrolyte. All operando measurements were done at -0.5 V vs. RHE in 1 M KOH saturated with CO_2.

5.6. CONCLUSION

We have experimentally identified a spectroscopic fingerprint of the formate intermediate on a copper-based catalyst during CO_2 reduction by tuning the coordination environment of copper within the Cu-BDC MOF structure. By reducing the copper coordination number from five to four, we created a square-planar CuO_4 site (Cu-BDC-4) that promotes oxygen-end adsorption of CO_2 and enables formate as the dominant product. In contrast, the original trigonal-bipyramidal CuO_5 site in Cu-BDC-5 leads primarily to CO formation. Experimental study of the reaction mechanism, reveals a CuO vibration at 536 cm^{-1}absent in Cu-BDC-5that we assign as the experimental fingerprint of the oxygen-bound formate pathway. Structural characterization of the MOFs confirms a more electron-deficient Cu^{2+} center in Cu-BDC-4, while DFT free-energy diagrams support a shift in the preferred reaction mechanism from *COOH to *OCHO. These findings demonstrate that subtle changes in copper coordination can dictate CO_2RR selectivity and provide direct experimental insight into the nature of key surface intermediates in MOF-based catalysts.

REFERENCES

[1] M. Li, H. Wang, W. Luo, P. C. Sherrell, J. Chen, and J. Yang. "Heterogeneous single-atom catalysts for electrochemical CO_2 reduction reaction". In: *Advanced Materials* 32.34 (2020), p. 2001848.

[2] J. Liang, H. Yu, J. Shi, B. Li, L. Wu, and M. Wang. "Dislocated bilayer MOF enables high-selectivity photocatalytic reduction of CO_2 to CO". In: *Advanced materials* 35.10 (2023), p. 2209814.

[3] S. Chu, Y. Cui, and N. Liu. "The path towards sustainable energy". In: *Nature materials* 16.1 (2017), pp. 16–22.

[4] Z. Sun, T. Ma, H. Tao, Q. Fan, and B. Han. "Fundamentals and challenges of electrochemical CO_2 reduction using two-dimensional materials". In: *Chem* 3.4 (2017), pp. 560–587.

[5] L. Zhang, I. Merino-Garcia, J. Albo, and C. M. Sánchez-Sánchez. "Electrochemical CO_2 reduction reaction on cost-effective oxide-derived copper and transition metal–nitrogen–carbon catalysts". In: *Current Opinion in Electrochemistry* 23 (2020), pp. 65–73.

[6] J. Wu, Y. Huang, W. Ye, and Y. Li. "CO_2 reduction: from the electrochemical to photochemical approach". In: *Advanced Science* 4.11 (2017), p. 1700194.

[7] J. Ding, H. Bin Yang, X.-L. Ma, S. Liu, W. Liu, Q. Mao, Y. Huang, J. Li, T. Zhang, and B. Liu. "A tin-based tandem electrocatalyst for CO_2 reduction to ethanol with 80% selectivity". In: *Nature Energy* 8.12 (2023), pp. 1386–1394.

[8] D. Gao, H. Zhou, F. Cai, J. Wang, G. Wang, and X. Bao. "Pd-containing nanostructures for electrochemical CO_2 reduction reaction". In: *Acs Catalysis* 8.2 (2018), pp. 1510–1519.

[9] C. Long, X. Li, J. Guo, Y. Shi, S. Liu, and Z. Tang. "Electrochemical reduction of CO_2 over heterogeneous catalysts in aqueous solution: recent progress and perspectives". In: *Small Methods* 3.3 (2019), p. 1800369.

[10] C. G. Okoye-Chine, K. Otun, N. Shiba, C. Rashama, S. N. Ugwu, H. Onyeaka, and C. T. Okeke. "Conversion of carbon dioxide into fuelsA review". In: *Journal of CO_2 Utilization* 62 (2022), p. 102099.

[11] Y. Chen, X.-Y. Li, Z. Chen, A. Ozden, J. E. Huang, P. Ou, J. Dong, J. Zhang, C. Tian, B.-H. Lee, *et al.* "Efficient multicarbon formation in acidic CO_2 reduction via tandem electrocatalysis". In: *Nature nanotechnology* (2023), pp. 1–8.

[12] J. Y. 'T. Kim, C. Sellers, S. Hao, T. P. Senftle, and H. Wang. "Different distributions of multi-carbon products in CO_2 and CO electroreduction under practical reaction conditions". In: *Nature Catalysis* 6.12 (2023), pp. 1115–1124.

[13] X. Li, X. Wu, X. Lv, J. Wang, and H. B. Wu. “Recent advances in metal-based electrocatalysts with hetero-interfaces for CO_2 reduction reaction”. In: *Chem Catalysis* (2022).

[14] W. Yang, K. Dastafkan, C. Jia, and C. Zhao. “Design of electrocatalysts and electrochemical cells for carbon dioxide reduction reactions”. In: *Advanced Materials Technologies* 3.9 (2018), p. 1700377.

[15] D. Voiry, H. S. Shin, K. P. Loh, and M. Chhowalla. “Low-dimensional catalysts for hydrogen evolution and CO_2 reduction”. In: *Nature Reviews Chemistry* 2.1 (2018), p. 0105.

[16] A. A. Peterson and J. K. Nørskov. “Activity descriptors for CO_2 electroreduction to methane on transition-metal catalysts”. In: *The Journal of Physical Chemistry Letters* 3.2 (2012), pp. 251–258.

[17] L. Majidi, A. Ahmadiparidari, N. Shan, S. N. Misal, K. Kumar, Z. Huang, S. Rastegar, Z. Hemmat, X. Zou, P. Zapol, *et al.* “2D copper tetrahydroxyquinone conductive metal-organic framework for selective CO_2 electrocatalysis at low overpotentials”. In: *Advanced Materials* 33.10 (2021), p. 2004393.

[18] J. Liu, D. Yang, Y. Zhou, G. Zhang, G. Xing, Y. Liu, Y. Ma, O. Terasaki, S. Yang, and L. Chen. “Tricycloquinazoline-based 2D conductive metal-organic frameworks as promising electrocatalysts for CO_2 reduction”. In: *Angewandte Chemie International Edition* 60.26 (2021), pp. 14473–14479.

[19] M. Bonneau, C. Lavenn, J.-J. Zheng, A. Legrand, T. Ogawa, K. Sugimoto, F.-X. Coudert, R. Reau, S. Sakaki, K.-i. Otake, *et al.* “Tunable acetylene sorption by flexible catenated metal-organic frameworks”. In: *Nature Chemistry* 14.7 (2022), pp. 816–822.

[20] L. Wang, J. Mao, G. Huang, Y. Zhang, J. Huang, H. She, C. Liu, H. Liu, and Q. Wang. “Configuration of hetero-framework via integrating MOF and triazine-containing COF for charge-transfer promotion in photocatalytic CO_2 reduction”. In: *Chemical Engineering Journal* 446 (2022), p. 137011.

[21] J. Jiao, X. Kang, J. Yang, S. Jia, Y. Peng, S. Liu, C. Chen, X. Xing, M. He, H. Wu, *et al.* “Steering the reaction pathway of CO_2 electroreduction by tuning the coordination number of copper catalysts”. In: *Journal of the American Chemical Society* 146.23 (2024), pp. 15917–15925.

[22] T. Yang, X. Mao, Y. Zhang, X. Wu, L. Wang, M. Chu, C.-W. Pao, S. Yang, Y. Xu, and X. Huang. “Coordination tailoring of Cu single sites on C3N4 realizes selective CO_2 hydrogenation at low temperature”. In: *Nature Communications* 12.1 (2021), p. 6022.

[23] Y.-Y. Liu, H.-L. Zhu, Z.-H. Zhao, N.-Y. Huang, P.-Q. Liao, and X.-M. Chen. “Insight into the Effect of the d-Orbital Energy of Copper Ions in Metal–Organic Frameworks on the Selectivity of Electroreduction of CO_2 to CH4”. In: *Acs Catalysis* 12.5 (2022), pp. 2749–2755.

[24] P. Saha, S. Amanullah, and A. Dey. “Selectivity in electrochemical CO_2 reduction”. In: *Accounts of chemical research* 55.2 (2022), pp. 134–144.

[25] S. Ito, F. J. White, E. Okunishi, Y. Aoyama, A. Yamano, H. Sato, J. D. Ferrara, M. Jasnowski, and M. Meyer. “Structure determination of small molecule compounds by an electron diffractometer for 3D ED/MicroED”. In: *CrystEngComm* 23.48 (2021), pp. 8622–8630.

[26] Rigaku Corporation. *CrysAlisPro, Version 171.44.93a*. Wroclaw, Poland, 2024.

[27] S. Abdelouhab, M. François, E. Elkaim, and P. Rabu. “Ab initio crystal structure of copper (II) hydroxy-terephthalate by synchrotron powder diffraction and magnetic properties”. In: *Solid state sciences* 7.2 (2005), pp. 227–232.

[28] G. Kresse and J. Hafner. “Ab initio molecular dynamics for open-shell transition metals”. In: *Physical Review B* 48.17 (1993), p. 13115.

[29] G. Kresse and J. Furthmüller. “Efficiency of ab-initio total energy calculations for metals and semiconductors using a plane-wave basis set”. In: *Computational materials science* 6.1 (1996), pp. 15–50.

[30] G. Kresse and J. Furthmüller. “Efficient iterative schemes for ab initio total-energy calculations using a plane-wave basis set”. In: *Physical review B* 54.16 (1996), p. 11169.

[31] J. P. Perdew, K. Burke, and M. Ernzerhof. “Generalized gradient approximation made simple”. In: *Physical review letters* 77.18 (1996), p. 3865.

[32] P. E. Blöchl. “Projector augmented-wave method”. In: *Physical review B* 50.24 (1994), p. 17953.

[33] M. Methfessel and A. Paxton. “High-precision sampling for Brillouin-zone integration in metals”. In: *physical review B* 40.6 (1989), p. 3616.

[34] G. Henkelman, A. Arnaldsson, and H. Jónsson. “A fast and robust algorithm for Bader decomposition of charge density”. In: *Computational Materials Science* 36.3 (2006), pp. 354–360.

[35] Q. Gong, P. Ding, M. Xu, X. Zhu, M. Wang, J. Deng, Q. Ma, N. Han, Y. Zhu, J. Lu, *et al.* “Structural defects on converted bismuth oxide nanotubes enable highly active electrocatalysis of carbon dioxide reduction”. In: *Nature communications* 10.1 (2019), p. 2807.

[36] A. Klinkova, P. De Luna, C.-T. Dinh, O. Voznyy, E. M. Larin, E. Kumacheva, and E. H. Sargent. “Rational design of efficient palladium catalysts for electroreduction of carbon dioxide to formate”. In: *Acs Catalysis* 6.12 (2016), pp. 8115–8120.

[37] J. S. Yoo, R. Christensen, T. Vegge, J. K. Nørskov, and F. Studt. “Theoretical insight into the trends that guide the electrochemical reduction of carbon dioxide to formic acid”. In: *ChemSusChem* 9.4 (2016), pp. 358–363.

[38] R. Christensen, H. A. Hansen, and T. Vegge. “Identifying systematic DFT errors in catalytic reactions”. In: *Catalysis Science & Technology* 5.11 (2015), pp. 4946–4949.

[39] J. K. Nørskov, J. Rossmeisl, A. Logadottir, L. Lindqvist, J. R. Kitchin, T. Bligaard, and H. Jonsson. “Origin of the overpotential for oxygen reduction at a fuel-cell cathode”. In: *The Journal of Physical Chemistry B* 108.46 (2004), pp. 17886–17892.

[40] Y.-J. Zhang, H. Ze, P.-P. Fang, Y.-F. Huang, A. Kudelski, J. Fernández-Vidal, L. J. Hardwick, J. Lipkowski, Z.-Q. Tian, and J.-F. Li. "Shell-isolated nanoparticle-enhanced Raman spectroscopy". In: *Nature Reviews Methods Primers* 3.1 (2023), p. 36.

[41] A. Cano, I. Monroy, M. Ávila, D. Velasco-Arias, J. Rodríguez-Hernández, and E. Reguera. "Relevant electronic interactions related to the coordination chemistry of tetracyanometallates. An XPS study". In: *New Journal of Chemistry* 43.46 (2019), pp. 18384–18393.

[42] L. Sun, Y. Zhao, Y. Shang, C. Sun, and M. Zhou. "The phase stability of terephthalic acid under high pressure". In: *Chemical Physics Letters* 689 (2017), pp. 56–61.

[43] L. Debbichi, M. Marco de Lucas, J. Pierson, and P. Kruger. "Vibrational properties of CuO and Cu_4O_3 from first-principles calculations, and Raman and infrared spectroscopy". In: *The Journal of Physical Chemistry C* 116.18 (2012), pp. 10232–10237.

[44] R. S. Salama, S. El-Hakam, S. Samra, S. El-Dafrawy, A. Ahmed, *et al.* "Adsorption, equilibrium and kinetic studies on the removal of methyl orange dye from aqueous solution by using of copper metal organic framework (Cu-BDC)". In: *Int. J. Modern Chem* 10.2 (2018), pp. 195–207.

[45] X. Fuku, M. Modibedi, and M. Mathe. "Green synthesis of Cu/Cu2O/CuO nanostructures and the analysis of their electrochemical properties". In: *SN Applied Sciences* 2.5 (2020), p. 902.

[46] G. Zhan, L. Fan, F. Zhao, Z. Huang, B. Chen, X. Yang, and S.-f. Zhou. "Fabrication of Ultrathin 2D Cu-BDC Nanosheets and the Derived Integrated MOF Nanocomposites". In: *Advanced Functional Materials* 29.9 (2019), p. 1806720.

[47] D. Zhang, X. Liu, Y. Zhao, H. Zhang, A. V. Rudnev, and J.-F. Li. "In situ Raman spectroscopic studies of CO 2 reduction reactions: from catalyst surface structures to reaction mechanisms". In: *Chemical Science* (2025).

6

Structure-Dependent Selectivity for CO_2 Reduction on Copper Clusters Supported on Carbon Derived from Cu-Based MOFs

Abstract

*This chapter investigates the impact of structural evolution on the electrocatalytic performance of MOF-derived Cu-based materials for the electrochemical CO_2 reduction reaction (CO_2RR). A series of 2D copper-organic frameworks, including Cu-THQ and Cu-HAB, were subjected to controlled carbonization under various conditions and compared against benchmark Cu-BTCderived composites. By adjusting carbonization temperature and method, we systematically tuned the size, dispersion, and coordination environment of in situformed Cu clusters within a conductive carbon matrix. Morphological and spectroscopic analyses revealed that lower-temperature treatments yielded smaller, low-coordination Cu sites, favoring *CO stabilization and CC coupling toward alcohols. In contrast, extended thermal treatments generated larger metallic Cu clusters that, through electronic coupling with the carbon framework, promoted HCOO* formation and enhanced selectivity toward formate. Among the samples studied,* $Cu@C-(THQ)_{1000C}$ *and* $Cu@C-(HAB)_{550C}$ *exhibited the highest formate Faradaic efficiencies and stable current densities. These results establish a direct link between copper cluster evolution and CO_2RR product distribution, providing a pathway for the rational design of MOF-derived electrocatalysts with tailored selectivity.*

A modified version of this chapter *will be submitted* as a scientific manuscript titled: K. Roohi, J. Coppen, H. Brouwer, A. Mol, P. Taheri, Structure-Dependent Selectivity for CO_2 Reduction on Copper Clusters Supported on Carbon Derived from Cu-Based MOFs.

6.1. INTRODUCTION

The escalating atmospheric concentration of carbon dioxide (CO_2) poses significant challenges to global sustainability [1]. While natural processes such as photosynthesis have historically maintained CO_2 levels over millennia [2], modern industrial activities now emit an additional 30 gigatons of CO_2 annually, far exceeding the capacity of existing plant life to sequester it [3]. This imbalance has contributed to a marked rise in global temperatures [4], giving rise to extreme weather events including droughts and floods, and placing immense strain on ecosystems worldwide [5]. In this regard, many research efforts have been directed toward developing green energy production methods that minimize CO_2 emissions.

A further incentive for adopting green energy is related to fuel resource distribution. Fossil fuels are geographically concentrated in limited regions, causing inequalities in resource availability and engendering geopolitical tensions [6, 7]. Shifts in local or global political climates can also lead to fluctuations in the cost of these fuels, thereby influencing global energy prices and economic stability [8, 9]. Since green energy sources often rely on resources that are more broadly dispersed, they offer an avenue to mitigate such issues [10].

Solar and wind power are among the fastest-growing green energy sources [11]. However, large-scale integration of these intermittent energy sources necessitates efficient storage technologies [12]. One promising route involves storing energy in chemical bonds by reducing atmospheric CO_2 into energy-rich fuels [13, 14]. When combusted, these fuels release CO_2, which can either be captured directly at the emission source or extracted from the ambient air, ultimately creating a closed, carbon-neutral cycle analogous to natural processes [15, 16].

In this context, CO_2 reduction reaction (CO_2RR) holds several advantages: the resultant products are generally easier to store than raw electrical energy, and many are compatible with existing fuel infrastructure. Additionally, CO_2 reduction is recognized as a potential strategy for controlling excess CO_2 levels [15, 17, 18]. However, CO_2RR typically requires high overpotentials due to slow intermediate reaction kinetics [19]. Moreover, the formation of multiple products with similar reduction potentials raises concerns regarding post-separation costs. Thus, intrinsic lack of selectivity complicates product separation and increases the net energy expenditure [20]. Consequently, strategies to improve selectivity at lower overpotentials are of substantial interest.

Several parameters influence CO_2 reduction efficiency including electrolyte composition, cell configuration, and, most critically, the choice of electrocatalyst [15]. The electrocatalyst plays a central role in determining both the activity and selectivity of CO_2RR. Numerous catalytic materials have been investigated, such as metals, semiconductors, and novel hybrid compounds [19, 21–24], each offering distinct advantages and limitations. Recent efforts to identify key catalyst properties indicate that high electrical conductivity, chemical stability, and abundant active sites are vital for improved performance.

Metalorganic frameworks (MOFs) have emerged as promising candidates in this context, offering an unusual combination of high surface area, tunable porosity, and precisely defined active sites [25, 26]. MOFs consist of metal centers connected by

organic linkers to form rigid frameworks with nano-sized voids. By modifying the linkers or substituting different metal centers, the size, structure, and reactivity of the pore environment can be tuned [27]. Both the metal node and the organic linker can serve as catalytic sites, enabling high density of accessible active centers [28].

Nevertheless, traditional MOFs suffer from low conductivity, limited mass transport [27], and potentially insufficient chemical stability under electrochemical conditions. Strategies to address these issues often involve tuning the frameworks dimensionality or performing post-synthetic modifications. For instance, restricting growth direction or employing specific linkers during synthesis can yield two-dimensional MOFs (2D-MOFs) with ultrathin layers, facilitating faster electron transport and improved diffusion of reactants and products [29]. Despite these advantages, 2D-MOFs still lag behind metallic conductors in conductivity, and their operational stability remains to be optimized [30].

Post-synthetic modifications are another important approach to improve MOF performance [31]. Thermal and chemical treatments have been widely explored [32, 33], yet the impact of such modifications on 2D-MOFs especially considering their structural distinctions from 3D analogues is scarcely investigated. Understanding this relationship could open new possibilities for optimizing both conductivity and selectivity, ultimately boosting the viability of MOFs as electrocatalysts in CO_2RR. In light of these considerations, the present work surveys potential post-processing routes for 2D MOFs, focusing on carbonization, to enhance CO_2 reduction selectivity. In particular, this study aims to elucidate the relationship between copper cluster size in MOF-derived carbon composites and their selectivity toward desired CO_2RR products.

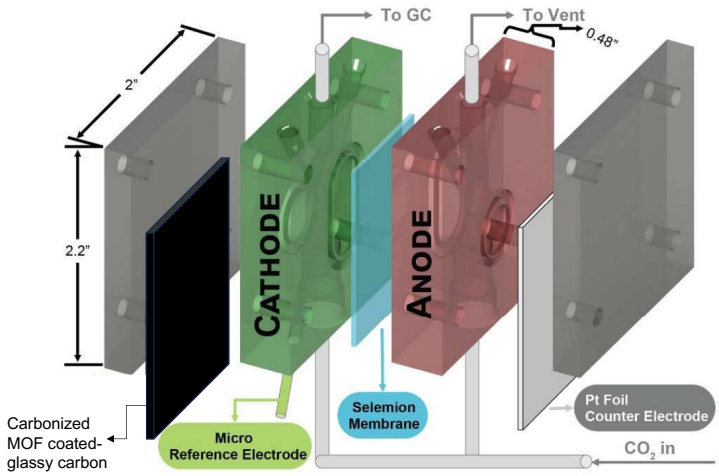

Figure 6.1: Schematic design of the electrochemical cell used for product analysis, inspired by the Lobaccaro et al. [34].

6.2. METHODOLOGY

Materials and Chemicals: Copper(II) nitrate hemi(pentahydrate) ($Cu(NO_3)_2$ů$2.5H_2O$, 99.999%), hexaaminobenzene trihydrochloride (HABů3HCl, 95%), isopropanol, potassium bicarbonate ($KHCO_3$), potassium hydroxide (KOH). Polytetrafluoroethylene (PTFE, 55 wt% dispersion in water) was obtained from FUELCELL store. Ultra-pure water (19.2 MΩcm) was obtained using a Milli-Q Advantage A10 purification system.
MOF Synthesis and Carbonization: Cu-BTC was purchased from Merck with a Cu content between 27 mol% and 30 mol%. Cu-THQ was obtained from CD-bioparticles. Cu-HAB was synthesized following the method reported by Feng et al. [35]. Briefly, 70 mg of $Cu(NO_3)_2.2.5H_2O$ (0.060 mmol) was dissolved in 5 mL of degassed distilled water containing 0.4 mL 28% aqueous NH_4OH. This solution was added to a solution of 30 mg HAB.3HCl in 5 mL distilled water and stirred at room temperature for 2 h. The resulting black powder was centrifuged, filtered, and washed with distilled water.

Cu-BTC was chosen as the reference material for further electrochemical performance comparison. The samples prepared through carbonization fo MOFs and their synthesis conditions and specifications are listed in Table 6.1:

Table 6.1: Summary of Cu/C catalyst synthesis conditions.

Sample	Synthesis Conditions
$Cu/C\text{-}(BTC)_{300C}$	Carbonized at 300 °C (20 °C/min) for 3 h, following Junyu et al. [36].
$Cu/C\text{-}(BTC)_{500C\text{-}SPS}$	Carbonized at 500 °C using Spark Plasma Sintering (SPS) with no applied pressure and rapid heatingcooling cycles, as discussed in methodology.
$Cu/C\text{-}(BTC)_{650C\text{-}SPS}$	Carbonized at 650 °C under identical SPS conditions as above.
$Cu/C\text{-}(BTC)_{1000C}$ and $Cu/C\text{-}(THQ)_{1000C}$	Heated at 1000 °C (5 °C/min) for 6 h in a tube furnace (Lenton PTF 16/75/610). The same procedure was applied to $Cu/C\text{-}(THQ)_{1000C}$.
$Cu/C\text{-}(HAB)_{550C}$	Heated at 550 °C (5 °C/min) for 6 h in the same tube furnace.

Material Characterization: Thermogravimetric analysis (TGA) was performed using a Setaram TAG 1750 instrument under an argon atmosphere. The temperature-dependent decomposition products were identified by coupling TGA with a Pfeiffer Vacuum GSD300 Omnistar Mass Spectrometer (MS). Scanning electron microscopy (SEM) and energy-dispersive spectroscopy (EDS) analyses were conducted using a JEOL JSM-IT100 SEM operating at 10 kV and a working distance of 10 mm.

Electrochemical Measurements: Initial electrochemical experiments were conducted in a three-electrode beaker setup with a glassy carbon working electrode, platinum mesh counter electrode, and standard calomel reference electrode (SCE)/3 M KCl solution. Electrolytes of 1 M $KHCO_3$ were saturated with CO_2 or purged with N_2 prior to testing. Subsequent electrochemical experiments utilized a dual-chamber electrochemical cell separated by an anion exchange membrane (AEM, FAS-PET-130). Cathodic and anodic chambers contained 1.8 mL of 1 M $KHCO_3$, with a miniature Ag/AgCl reference electrode and platinum plate counter electrode. Electrolytes were CO_2 saturated (10 mL/min for 10 min) (Fig. 6.1). Catalyst inks for working electrodes initially consisted of 5 wt% PVA, 5 wt% carbon black, and 90 wt% active material in distilled water, sonicated for 30 min. Later inks contained 20 wt% PTFE, 5 wt% carbon black, and 70 wt% active material in water/isopropanol (1:1 vol%), sonicated for 10 min. Electrodes were prepared by drop-casting inks onto glassy carbon substrates.

Cyclic voltammetry (CV) measurements employed a Biologic VSP-300 potentiostat at 5 mV/s from 0 to -0.5 V vs SCE. Linear sweep voltammetry (LSV) was performed at 50 mV/s from 0 to -2 V vs SCE. Electrochemical impedance spectroscopy (EIS) measurements were conducted from 100 kHz to 100 mHz at open circuit potential (OCP). Chronoamperometric measurements applied a constant potential of -1.6 V vs Ag/AgCl (approximately -0.90 V vs RHE) for 1 h, recording currents every 0.1 s.
Product Analysis: Gas chromatography (GC, Global Analyzer Solutions Compact GC 4.0) equipped with flame ionization (FID) and thermal conductivity detectors (TCD) was used for gaseous product analysis. Measurements were conducted at 5-minute intervals. High-performance liquid chromatography (HPLC, Agilent 1260 Infinity II) with a diode array detector analyzed liquid products. Electrolyte samples were directly injected post-experiment. Nuclear magnetic resonance spectroscopy (NMR) for supplementary liquid analysis was performed using a Bruker Ascend 500 magnet equipped with a NEO console, and data were processed using MestreNova software.
Faradaic Efficiency Calculations: Faradaic efficiencies (FE) were calculated using the equation:

$$\mathrm{FE} = \frac{n_i N F}{j t} \tag{6.1}$$

where n_i represents the number of moles of the detected product, N is the number of the transferred electrons in a reaction, F is the Faradaic constant (s A/mol), j is the current density (A) and t is the time of the measurement in seconds.

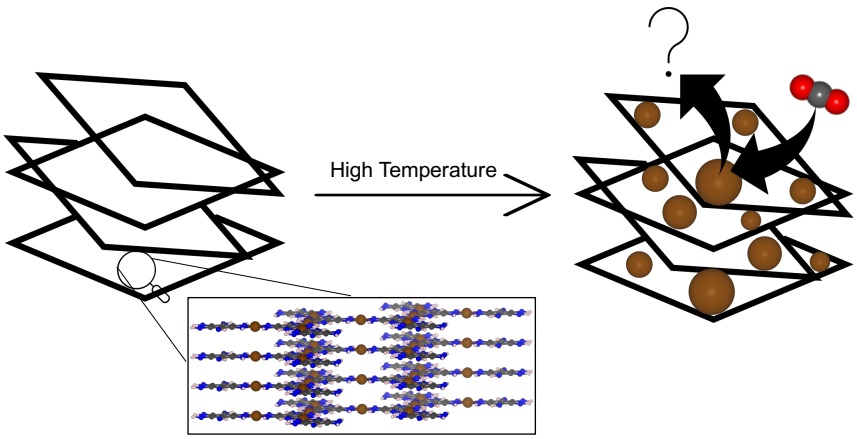

Figure 6.2: Schematic of carbonization process of 2D MOFs.

6.3. STRUCTURAL AND FUNCTIONAL FEATURES OF THE CATALYST

Both partial and full carbonization protocols were applied to Cu-based 2D MOFs and compared against a carbonized Cu-BTC benchmark. Specifically, partial carbonization of Cu-BTC was carried out in a tubular furnace at 300°C, producing $Cu/C-(BTC)_{300C}$, while spark plasma sintering (SPS) at 500°C and 650°C gave rise to $Cu/C-(BTC)_{500C–SPS}$ and $Cu/C-(BTC)_{650C–SPS}$, respectively. Full carbonization of Cu-BTC at 1000 °C yielded $Cu/C-(BTC)_{1000C}$, providing a reference sample with near-complete linker decomposition. In parallel, Cu-THQ was fully carbonized at 1000 °C to obtain $Cu/C-(THQ)_{1000C}$, preserving its sheetlike framework while driving off most of the organic components. By contrast, Cu-HAB was heated to 550 °C, producing $Cu/C-(HAB)_{550C}$, where the lower temperature aimed at retaining a higher fraction of nitrogen in the final carbonized material. Together, six samples $Cu/C-(BTC)_{300C}$, $Cu/C-(BTC)_{500C–SPS}$, $Cu/C-(BTC)_{650C–SPS}$, $Cu/C-(BTC)_{1000C}$, $Cu/C-(THQ)_{1000C}$, and $Cu/C-(HAB)_{550C}$ encompass a range of carbonization methods, temperatures, and dimensionalities. As illustrated in the Fig. 6.2, the partial or full carbonization of 2D MOFs yields a carbon-based matrix with well-dispersed copper clusters, serving as active sites that can be tuned to influence product selectivity in CO_2RR.

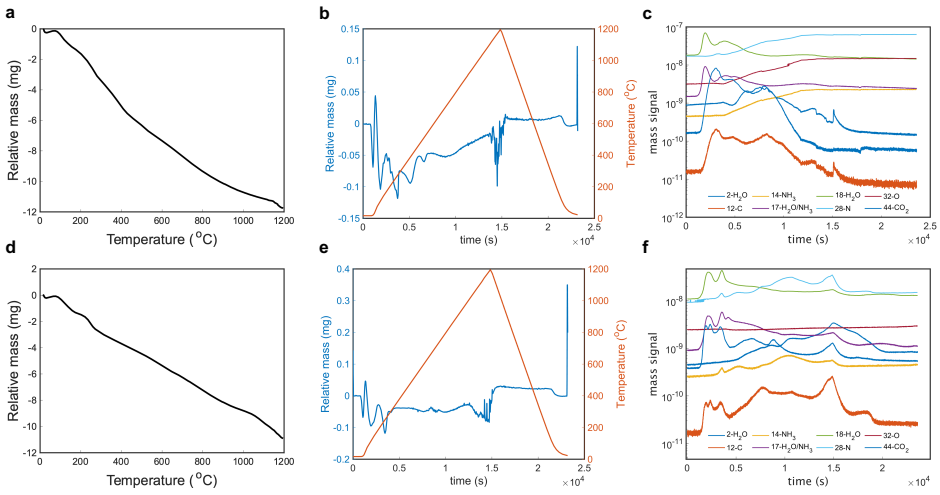

Figure 6.3: a, TGA profile of 20.78 mg Cu-THQ, showing the changes of relative mass of the sample with temperature. **b**, weight loss derivative profile with duration of the measurement and corresponding temperature. **c**, mass spectroscopy of the gasses emitted during the TGA measurement for Cu-THQ-MOF. **d**, TGA profile of 15.68 mg Cu-HAB, showing the changes of relative mass of the sample with temperature. **e**, weight loss derivative profile with duration of the measurement and corresponding temperature. **f**, mass spectroscopy of the gasses emitted during the TGA measurement for Cu-HAB-MOF.

Simultaneous thermogravimetric analysis (TGA) and mass spectrometry (MS) were conducted on Cu-THQ and Cu-HAB MOFs in order to elucidate the decomposition

characteristics of the linkers. In the case of Cu-THQ, the TGA profile indicated considerable mass loss below 400°C, which was attributed to decomposition of the THQ linker and the concurrent release of H_2O and CO_2 (Fig. 6.3a). Corresponding MS data corroborated that evolved gases were predominantly H_2O and CO_2, implying that the organic linker undergoes complete decomposition before reaching 400°C. These observations align with the findings of J. Lisha et al. [37] (Fig. 6.3c). A similar trend was observed for Cu-HAB, which also demonstrated substantial mass loss below 400°C (Fig. 6.3d). However, MS results revealed a marked reduction in nitrogen evolution above 550°C, suggesting that carbonizing Cu-HAB at approximately 550°C preserves a greater amount of nitrogen within the material (Fig. 6.3f). This retained nitrogen could prove advantageous for electrocatalytic performance in CO_2 reduction reactions, as nitrogen sites often play a key role in facilitating CO_2 adsorption and activation [38].

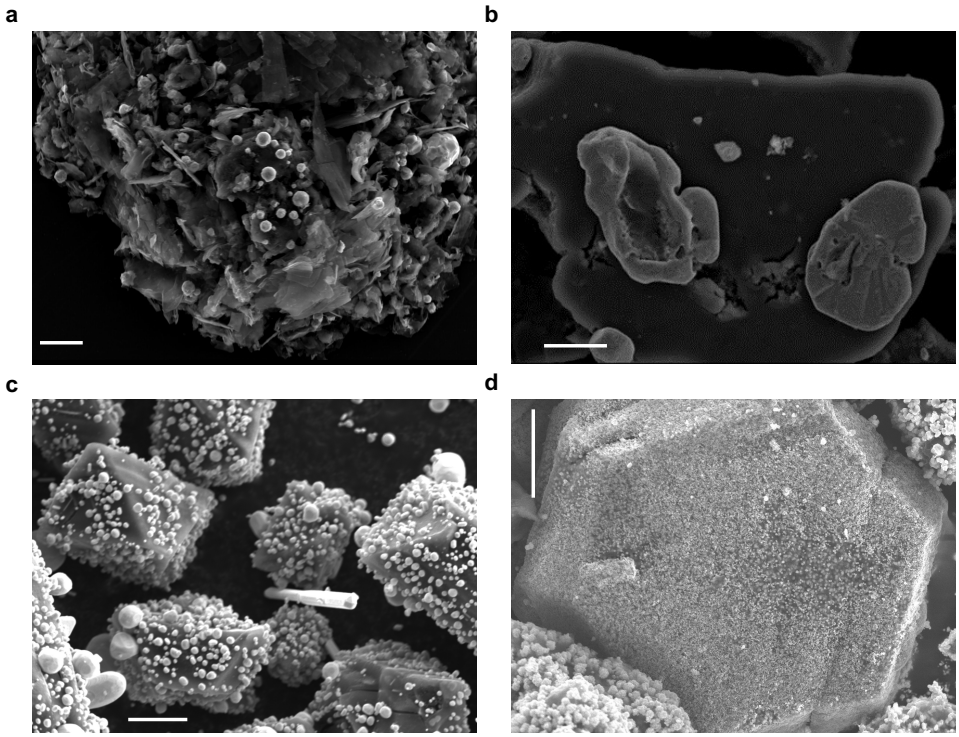

Figure 6.4: SEM images of **a**, Cu/C−$(THQ)_{1000C}$ prepared at 1000°C for 5 h in a tubular furnace under Ar atmosphere with a heating rate of 5°C/min. **b**, Cu/C−$(HAB)_{550C}$ prepared at 550°C for 6 h in a tubular furnace under Ar atmosphere with a heating rate of 5°C/min. **c**, Cu/C−$(BTC)_{1000C}$ prepared at 1000°C for 6 h in a tubular furnace under Ar atmosphere with a heating rate of 5°C/min. **d**, Cu/C−$(BTC)_{650C–SPS}$ prepared at 650°C by SPS. Scale bar: 10 μm.

In the case of Cu-THQ carbonized at 1000°C $\left(\text{Cu/C}-(\text{THQ})_{1000C}\right)$, scanning electron microscopy (SEM) images revealed that the 2D sheet-like morphology was preserved post-carbonization, with copper clusters forming on the surface (Fig. 6.4a). The

particles exhibited a tendency to agglomerate, forming larger structures. Cu-HAB carbonized at 550°C $\left(Cu/C-(HAB)_{550C}\right)$ also retained its 2D morphology. Interestingly, plate-like copper clusters formed on some grain surfaces, which differed from the round clusters observed in carbonized Cu-THQ (Fig. 6.4b). Simultaneous energy-dispersive spectroscopy (EDS) with SEM analysis on spot indicated that these plate-like clusters had a high copper content, and the material partly retained its nitrogen content. The nitrogen retention may influence the electronic properties and catalytic activity of the material.

SEM images of carbonized Cu-BTC at 1000°C $\left(Cu/C-(BTC)_{1000C}\right)$ revealed the formation of similar copper clusters on the MOF surface as in the case of $Cu/C-(THQ)_{1000C}$. Although, the size and distribution of these clusters varied across different particles. In contrast, Cu-BTC carbonized at 650°C $\left(Cu/C-(BTC)_{650C–SPS}\right)$ showed smaller and less abundant copper clusters. No morphological features other than those described were observed across the other carbonized Cu-BTC samples.

6.4. ELECTROCHEMICAL PERFORMANCE AND PRODUCT ANALYSIS

Following morphological characterization, the samples shown in Fig. 6.4 were used to investigate their electrochemical performance toward CO_2RR. To further assess the activity of the samples, linear sweep voltammetry (LSV) measurements were conducted on Cu-based MOF composites deposited on glassy carbon substrates. As shown in Fig. 6.5a $Cu/C-(THQ)_{1000C}$ exhibits the highest activity with current density ($-58\,mA,cm^{-2}$ at $-1.0\,V$vs RHE), followed by $Cu/C-(HAB)_{550C}$ ($-32\,mA,cm^{-2}$). In contrast, both Cu-BTCderived composites are almost inactive under identical conditions, confirming that 2D framework of the carbon substrate on Cu/C samples, leads to higher charge transfer conductivity during the CO_2RR. Product analysis of the samples was done at -1 V vs. RHE using the flow cell shown in Fig. 6.1 with CO_2 being purged continuously in the catholyte. Faradaic efficiency trends extracted from Fig. 6.5b show that all catalysts favour formate production, but the relative partitioning is highly catalyst-specific: $Cu/C-(THQ)_{1000C}$ and $Cu/C-(HAB)_{550C}$ exhibit roughly 60% and 55% FE, respectively, to H_2, while still achieving 3035% FE for formate. Complete linker removal in $Cu/C-(BTC)_{1000C}$ raises $FE_{formate}$ to ~28%, whereas the cluster-poor $Cu/C-(BTC)_{650C–SPS}$ exhibits the broadest product spectrum (40% H_2, 14% formate, 15% 1-propanol, 5% ethyl acetate). This observation was also reported before that abundant, lowcoordination Cu surface sites on carbonized Cu-BTC, stabilize high *CO coverage and favor its hydrogenation to CHO/COH, steering the surface pathway toward alcohols [39]. Taken together, these trends indicate small Cu clusters on functional carbon framework, stabilizes *CO intermediate at moderate coverage, while larger metallic Cu channels selectivity via HCOO* intermediate to formate consistent with previous reports [40, 41]. Thus, longer treatments yields larger Cu clusters that through Cu/carbon electronic coupling, weaken *CO binding, stabilizing HCOO* intermediate, and facilitate formate desorption enhancing its selectivity on Cu-based electrocatalysts [42, 43].

Furthermore, chronoamperometric (CA) traces at -1 V vs. RHE in 1 M

$KHCO_3$ depicted in Fig. 6.5c confirm operational stability during the product analysis measurements. Formate partial current densities of $Cu/C-(THQ)_{1000C}$ and $Cu/C-(HAB)_{550C}$ are calculated to be (-3.2 and $-3.5\,mA,cm^{-2}$, respectively.) Fig. 6.5d, shows the schematic of the proposed reaction pathway on the surface of the prepared Cu/C samples. The diagram illustrates that CO_2 first adsorbs to the catalytic surface and is hydrogenated via a coupled proton/electron transfer to form the surface intermediate HCOO*. This pathway rationalizes the observed formate selectivity when larger, electronically coupled Cu clusters are embedded in the conductive carbon matrix.

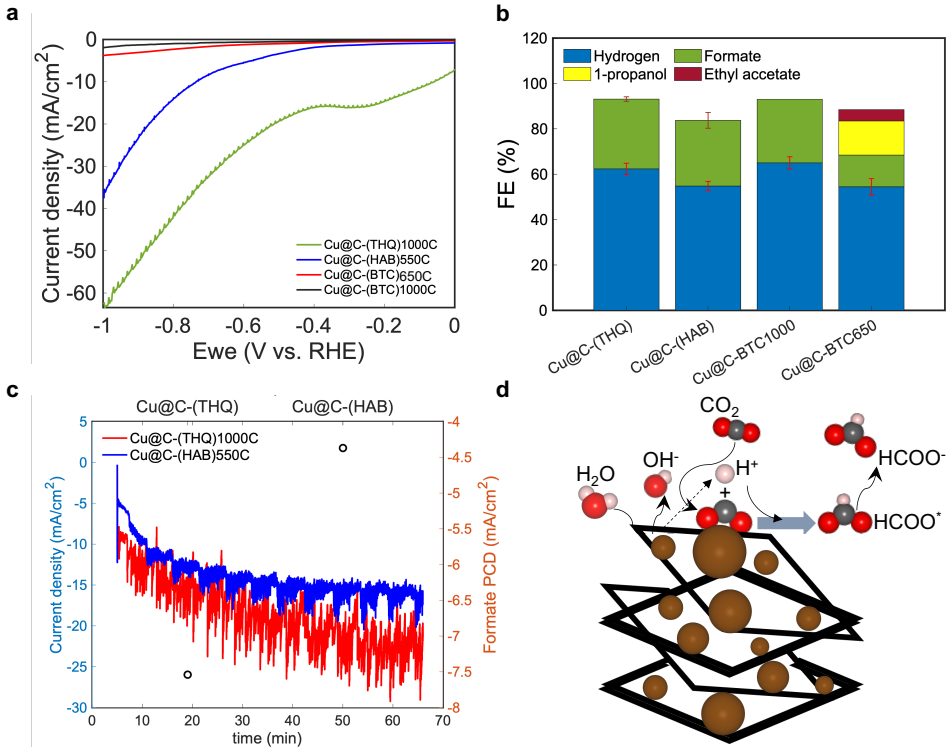

Figure 6.5: a, LSV performance of the carbonized samples in CO_2 in 1 M $KHCO_3$ with a scan rate of 50 mV/s, **b**, CO_2RR product distribution of carbonized samples at -1 V vs. RHE in a flow cell with a continues flow of CO_2 in 1.8 mL of 1 M $KHCO_3$, **c**, CA profile of Cu/C-2D frameworks during product analysis measurements with formate partial current densities and, **d**, Schematic of the proposed CO_2RR mechanism on the surface of the Cu/C-based 2D frameworks.

6.5. CONCLUSION

We have explored the structureselectivity relationship in MOF-derived Cu catalysts by varying the size of the copper active sites via carbonization conditions. Through

the transformation of 2D Cu-THQ and Cu-HAB MOFs into conductive coppercarbon composites, we demonstrate that cluster size and electronic coupling to the carbon matrix play decisive roles in determining CO_2RR product selectivity. While smaller Cu clusters on carbonized Cu-BTC promote *CO accumulation and CC coupling pathways toward alcohols and multi-carbon products, the formation of larger metallic Cu domains in fully carbonized frameworks favors the HCOO* pathway, enhancing formate selectivity. In particular, $Cu/C-(THQ)_{1000C}$ and $Cu/C-(HAB)_{550C}$ exhibit high activity and stable operation with formate as the dominant product. These findings underscore the importance of fine-tuning carbonization protocols to modulate copper cluster size and dispersion, offering a rational design strategy for improving both activity and selectivity in MOF-derived electrocatalysts for CO_2 reduction.

REFERENCES

[1] M. Li, H. Wang, W. Luo, P. C. Sherrell, J. Chen, and J. Yang. "Heterogeneous single-atom catalysts for electrochemical CO_2 reduction reaction". In: *Advanced Materials* 32.34 (2020), p. 2001848.

[2] C. Beer, M. Reichstein, E. Tomelleri, P. Ciais, M. Jung, N. Carvalhais, C. Rödenbeck, M. A. Arain, D. Baldocchi, G. B. Bonan, A. Bondeau, A. Cescatti, G. Lasslop, A. Lindroth, M. Lomas, S. Luyssaert, H. Margolis, K. W. Oleson, O. Roupsard, E. Veenendaal, N. Viovy, C. Williams, F. I. Woodward, and D. Papale. "Terrestrial Gross Carbon Dioxide Uptake: Global Distribution and Covariation with Climate". In: *Science* 329.5993 (2010), pp. 834–838. DOI: 10.1126/science.1184984. eprint: https://www.science.org/doi/pdf/10.1126/science.1184984. URL: https://www.science.org/doi/abs/10.1126/science.1184984.

[3] H. Wang, B. Ang, and B. Su. "A Multi-region Structural Decomposition Analysis of Global CO_2 Emission Intensity". In: *Ecological Economics* 142 (2017), pp. 163–176. ISSN: 0921-8009. DOI: https://doi.org/10.1016/j.ecolecon.2017.06.023. URL: https://www.sciencedirect.com/science/article/pii/S0921800917303749.

[4] A. Stips, D. Macias, C. Coughlan, E. Garcia-Gorri, and X. Liang. "On the causal structure between CO_2 and global temperature". In: *Scientific Reports* 6 (1 2016). ISSN: 2045-2322. DOI: 10.1038/srep21691. URL: https://doi.org/10.1038/srep21691.

[5] U. Nations. *Causes and Effects of Climate Change*. URL: https://www.un.org/en/climatechange/science/causes-effects-climate-change (visited on 11/17/2022).

[6] N. Choucri and V. Ferraro. *International politics of energy interdependence: the case of petroleum*. Massachusetts Institute of Technology, 1976. URL: https://www.osti.gov/biblio/7365581.

[7] M. Kivinen and B. Humphreys. *Russian Modernization: A new Paradigm*. Routledge, 2020, pp. 25–26. DOI: https://doi.org/10.4324/9781003099161.

[8] C. Ang'u, N. Muthama, C. Oludhe, and L. S. Kong'ani. "Effects of Civil Conflicts on Global Oil Prices and their Impact on the Energy Sector". In: *Journal of Sustainability, Environment and Peace* 1 (Apr. 2019). DOI: 10.53537/jsep.2019.02.003.

[9] A. J. Garzon Gordon and L. A. Hierro Recio. "External Effects of the War in Ukraine: The Impact on the Price of Oil in the Short-term". In: 9 (Feb. 2019), pp. 267–276. URL: https://www.econjournals.com/index.php/ijeep/article/view/7380.

[10] G. Kharlamova, S. Nate, and O. Chernyak. “Renewable energy and security for Ukraine: Challenge or smart way?” In: *Journal of International Studies* 9 (Mar. 2016), pp. 88–115. DOI: 10.14254/2071-8330.2016/9-1/7.

[11] IEA. *Global Energy Review 2021*. 2021. URL: https://www.iea.org/reports/global-energy-review-2021 (visited on 08/10/2022).

[12] W. A. Braff, J. M. Mueller, and J. E. Trancik. “Value of storage technologies for wind and solar energy”. In: *Nature Climate Change* 6.10 (2016), pp. 964–969.

[13] M. Yu, R. Dong, and X. Feng. “Two-Dimensional Carbon-Rich Conjugated Frameworks for Electrochemical Energy Applications”. In: *Journal of the American Chemical Society* 142.30 (2020), pp. 12903–12915. DOI: 10.1021/jacs.0c05130. eprint: https://doi.org/10.1021/jacs.0c05130. URL: https://doi.org/10.1021/jacs.0c05130.

[14] P. Gonugunta, K. Roohi, M. Soleimani, P. R. Anusuyadevi, P. Taheri, and M. Ramdin. “Screening of Binder Materials for Ag-Based Gas Diffusion Electrodes for CO_2 Conversion to CO”. In: *Industrial & Engineering Chemistry Research* (2025).

[15] X. Zhang, S.-X. Guo, K. Gandionco, A. Bond, and J. Zhang. “Electrocatalytic carbon dioxide reduction: from fundamental principles to catalyst design”. In: *Materials Today Advances* 7 (Sept. 2020), p. 100074. DOI: 10.1016/j.mtadv.2020.100074.

[16] D. Gao, H. Zhou, F. Cai, J. Wang, G. Wang, and X. Bao. “Pd-containing nanostructures for electrochemical CO_2 reduction reaction”. In: *Acs Catalysis* 8.2 (2018), pp. 1510–1519.

[17] J. Albo, M. Alvarez-Guerra, P. Castaño, and A. Irabien. “Towards the electrochemical conversion of carbon dioxide into methanol”. In: *Green Chem.* 17 (4 2015), pp. 2304–2324. DOI: 10.1039/C4GC02453B. URL: http://dx.doi.org/10.1039/C4GC02453B.

[18] Z. W. Seh, J. Kibsgaard, C. F. Dickens, I. Chorkendorff, J. K. Nørskov, and T. F. Jaramillo. “Combining theory and experiment in electrocatalysis: Insights into materials design”. In: *Science* 355.6321 (2017), eaad4998. DOI: 10.1126/science.aad4998. eprint: https://www.science.org/doi/pdf/10.1126/science.aad4998. URL: https://www.science.org/doi/abs/10.1126/science.aad4998.

[19] X. Nie, M. R. Esopi, M. J. Janik, and A. Asthagiri. “Selectivity of CO_2 Reduction on Copper Electrodes: The Role of the Kinetics of Elementary Steps”. In: *Angewandte Chemie International Edition* 52.9 (2013), pp. 2459–2462. DOI: https://doi.org/10.1002/anie.201208320. eprint: https://onlinelibrary.wiley.com/doi/pdf/10.1002/anie.201208320. URL: https://onlinelibrary.wiley.com/doi/abs/10.1002/anie.201208320.

[20] J. Y. ‘T. Kim, C. Sellers, S. Hao, T. P. Senftle, and H. Wang. “Different distributions of multi-carbon products in CO_2 and CO electroreduction under practical reaction conditions”. In: *Nature Catalysis* 6.12 (2023), pp. 1115–1124.

[21] K. P. Kuhl, E. R. Cave, D. N. Abram, and T. F. Jaramillo. “New insights into the electrochemical reduction of carbon dioxide on metallic copper surfaces”. In: *Energy Environ. Sci.* 5 (5 2012), pp. 7050–7059. DOI: 10.1039/C2EE21234J. URL: http://dx.doi.org/10.1039/C2EE21234J.

[22] A. A. Peterson, F. Abild-Pedersen, F. Studt, J. Rossmeisl, and J. K. Nørskov. “How copper catalyzes the electroreduction of carbon dioxide into hydrocarbon fuels”. In: *Energy Environ. Sci.* 3 (9 2010), pp. 1311–1315. DOI: 10.1039/C0EE00071J. URL: http://dx.doi.org/10.1039/C0EE00071J.

[23] Y. Y. Birdja, E. Pérez-Gallent, M. C. Figueiredo, A. J. Göttle, F. Calle-Vallejo, and M. T. Koper. “Advances and challenges in understanding the electrocatalytic conversion of carbon dioxide to fuels”. In: *Nature Energy* 4.9 (2019), pp. 732–745.

[24] B. Zhang, Y. Jiang, M. Gao, T. Ma, W. Sun, and H. Pan. “Recent progress on hybrid electrocatalysts for efficient electrochemical CO_2 reduction”. In: *Nano Energy* 80 (2021), p. 105504.

[25] J. Liu, D. Yang, Y. Zhou, G. Zhang, G. Xing, Y. Liu, Y. Ma, O. Terasaki, S. Yang, and L. Chen. “Tricycloquinazoline-based 2D conductive metal-organic frameworks as promising electrocatalysts for CO_2 reduction”. In: *Angewandte Chemie International Edition* 60.26 (2021), pp. 14473–14479.

[26] M. Bonneau, C. Lavenn, J.-J. Zheng, A. Legrand, T. Ogawa, K. Sugimoto, F.-X. Coudert, R. Reau, S. Sakaki, K.-i. Otake, *et al.* “Tunable acetylene sorption by flexible catenated metal-organic frameworks”. In: *Nature Chemistry* 14.7 (2022), pp. 816–822.

[27] X. Li and Q.-L. Zhu. “MOF-based materials for photo- and electrocatalytic CO_2 reduction”. In: *EnergyChem* 2.3 (2020), p. 100033. ISSN: 2589-7780. DOI: https://doi.org/10.1016/j.enchem.2020.100033. URL: https://www.sciencedirect.com/science/article/pii/S2589778020300087.

[28] L. Majidi, A. Ahmadiparidari, N. Shan, S. N. Misal, K. Kumar, Z. Huang, S. Rastegar, Z. Hemmat, X. Zou, P. Zapol, *et al.* “2D copper tetrahydroxyquinone conductive metal-organic framework for selective CO_2 electrocatalysis at low overpotentials”. In: *Advanced Materials* 33.10 (2021), p. 2004393.

[29] L. Xiao, Z. Wang, and J. Guan. “2D MOFs and their derivatives for electrocatalytic applications: Recent advances and new challenges”. In: *Coordination Chemistry Reviews* 472 (2022), p. 214777.

[30] Y. Xue, G. Zhao, R. Yang, F. Chu, J. Chen, L. Wang, and X. Huang. “2D metal–organic framework-based materials for electrocatalytic, photocatalytic and thermocatalytic applications”. In: *Nanoscale* 13.7 (2021), pp. 3911–3936.

[31] M. Varsha, G. Nageswaran, L. Jothi, *et al.* “Recent advances in metal organic framework derived carbon materials for electrocatalytic applications”. In: *Journal of the Electrochemical Society* 169.3 (2022), p. 036503.

[32] T. Wang, X. Cao, and L. Jiao. “MOFs-derived carbon-based metal catalysts for energy-related electrocatalysis”. In: *Small* 17.22 (2021), p. 2004398.

[33] S. Zhao, H. Yin, L. Du, L. He, K. Zhao, L. Chang, G. Yin, H. Zhao, S. Liu, and Z. Tang. “Carbonized nanoscale metal–organic frameworks as high performance electrocatalyst for oxygen reduction reaction”. In: *ACS nano* 8.12 (2014), pp. 12660–12668.

[34] P. Lobaccaro, M. R. Singh, E. L. Clark, Y. Kwon, A. T. Bell, and J. W. Ager. “Effects of temperature and gas–liquid mass transfer on the operation of small electrochemical cells for the quantitative evaluation of CO 2 reduction electrocatalysts”. In: *Physical Chemistry Chemical Physics* 18.38 (2016), pp. 26777–26785.

[35] D. Feng, T. Lei, M. Lukatskaya, J. Park, Z. Huang, M. Lee, L. Shaw, S. Chen, A. Yakovenko, A. Kulkarni, J. Xiao, K. Fredrickson, J. Tok, X. Zou, Y. Cui, and Z. Bao. “Robust and conductive two-dimensional metalorganic frameworks with exceptionally high volumetric and areal capacitance”. In: *Nature Energy* 3 (Jan. 2018). DOI: 10.1038/s41560-017-0044-5.

[36] J. Liu, L. Peng, Y. Zhou, L. Lv, J. Fu, J. Lin, D. Guay, and J. Qiao. “MetalOrganic-Frameworks-Derived Cu/Cu2O Catalyst with Ultrahigh Current Density for Continuous-Flow CO_2 Electroreduction”. In: *ACS Sustainable Chemistry and Engineering* 7.18 (2019), pp. 15739–15746. DOI: 10.1021/acssuschemeng.9b03892. eprint: https://doi.org/10.1021/acssuschemeng.9b0382. URL: https://doi.org/10.1021/acssuschemeng.9b0382.

[37] L. Jia, K. Wagner, J. Smyth, D. Officer, J. Chen, and P. Wagner. “Cu-THQ-EFG Composite for Highly Selective Electrochemical CO_2 Reduction to Formate at Low Overpotentials”. In: *Polymers* 14.23 (2022). ISSN: 2073-4360. DOI: 10.3390/polym14235112. URL: https://www.mdpi.com/2073-4360/14/23/5112.

[38] S. Liu, H. Yang, X. Huang, L. Liu, W. Cai, J. Gao, X. Li, T. Zhang, Y. Huang, and B. Liu. “Identifying active sites of nitrogen-doped carbon materials for the CO_2 reduction reaction”. In: *Advanced Functional Materials* 28.21 (2018), p. 1800499.

[39] A. V. Rayer, E. Reid, A. Kataria, I. Luz, S. J. Thompson, M. Lail, J. Zhou, and M. Soukri. “Electrochemical carbon dioxide reduction to isopropanol using novel carbonized copper metal organic framework derived electrodes”. In: *Journal of CO_2 Utilization* 39 (2020), p. 101159.

[40] R. Reske, H. Mistry, F. Behafarid, B. Roldan Cuenya, and P. Strasser. “Particle size effects in the catalytic electroreduction of CO_2 on Cu nanoparticles”. In: *Journal of the American Chemical Society* 136.19 (2014), pp. 6978–6986.

[41] Y.-J. Shen, Y.-H. Hsu, Y.-C. Chang, J.-J. Ma, K.-S. Peng, Y.-R. Lu, S.-H. Hsu, and S.-F. Hung. “Microenvironment Matters: Copper–Carbon Composites Enable a Highly Efficient Carbon Dioxide Reduction Reaction to C2 Products”. In: *ACS Applied Materials & Interfaces* 17.6 (2025), pp. 9378–9390.

[42] D. Li, T. Liu, L. Huang, J. Wu, J. Li, L. Zhen, and Y. Feng. “Selective CO 2-to-formate electrochemical conversion with core–shell structured Cu 2 O/Cu@ C composites immobilized on nitrogen-doped graphene sheets”. In: *Journal of Materials Chemistry A* 8.35 (2020), pp. 18302–18309.

[43] J. Du, Y. Xin, M. Dong, J. Yang, Q. Xu, H. Liu, and B. Han. “Copper/carbon heterogenous interfaces for enhanced selective electrocatalytic reduction of CO_2 to formate”. In: *Small* 17.41 (2021), p. 2102629.

7

Conclusion and Recommendations

7.1. SUMMARY OF KEY FINDINGS

Despite significant advances in activity descriptors for CO_2RR, such as volcano plots based on adsorption energies of key intermediates, current theoretical frameworks still face substantial limitations in predicting and guiding selectivity. Selectivity in CO_2RR, a reaction involving multiple competing pathways and intermediates, cannot be fully captured by single-parameter metrics like *COOH or *OCHO binding energies. Such descriptors overlook the nuanced interplay of thermodynamics, kinetics, and structural effects at the active site. There is therefore a growing need to move beyond traditional approaches and toward structure-based indicators that reflect the local electronic environment, coordination geometry, and bonding characteristics, all of which can dramatically influence product distribution.

This thesis addresses that challenge by employing MOF-based catalysts as a versatile platform for selectivity-focused catalyst design. The modular nature of MOFs provides atomically isolated metal centers in a well-defined coordination environment, making it possible to systematically control metalligand geometry, ligand identity, and electronic structure. These characteristics not only allow for direct investigation of structurefunction relationships but also open the door to overcoming intrinsic limitations of conventional metal catalysts, such as the inability to decouple the adsorption energies of key intermediates due to linear scaling relationships (LSRs). A key motivation throughout this work has been to exploit the atomic precision and post-synthetic tunability of MOFs to address the dual challenges of poor selectivity and low conductivity in CO_2RR.

A unifying theme that emerged from this research is the critical role of local coordination environment in breaking selectivity constraints imposed by LSRs. Copper, one of the most active metals for CO_2RR, is inherently limited by these relationships, which prevent independent tuning of *COOH, *CO, and *OCHO adsorption energies. The studies presented here show that MOFs can serve as a testing ground for overcoming this limitation, as their precisely defined active sites enable the development of structural descriptors for predicting selectivity. By systematically modifying the coordination sphere of copper centers in Cu-BDC MOFs, it was possible to steer the CO_2RR pathway toward different C_1 products. Incorporation of heteroatoms such as sulfur into the Cu-BDC framework generated a quasi-two-dimensional CuSBDC structure with planar CuS building units that selectively favored formate formation. DFT simulations confirmed that sulfur coordination shifts the copper *d*-band center, strengthens *OCHO adsorption, and thereby promotes the formate pathway over CO formation. This demonstrated not only the role of heteroatom coordination in intermediate stabilization but also the structural adaptability of MOFs as a catalyst design platform.

In parallel, coordination geometry was fine-tuned by reducing the number of axial oxygen ligands bound to copper centers in Cu-BDC. This subtle but effective change in local structure shifted selectivity from CO toward formate, reinforcing the conclusion that precise control over metalligand configuration can guide the reaction pathway. Operando Raman spectroscopy directly monitored these changes under reaction conditions, revealing strong *OCHO bands in the four-coordinate material and predominantly *CO bands in the five-coordinate analogue. The identification of a distinct CuO stretching mode associated with *OCHO provided a spectroscopic fingerprint for tracking this intermediate in real time, enabling a direct correlation between surface chemistry and catalytic

performance. This spectroscopic insight adds an important mechanistic tool for studying CO_2RR on Cu-based materials.

While much of this work focused on improving selectivity, the inherently low conductivity of pristine MOFs remains a barrier to achieving high catalytic activity. To address this, the approach was extended to MOF-based composites. Two-dimensional Cu-MOFs were subjected to controlled carbonization, converting the frameworks into conductive carbon-rich networks embedded with copper clusters. This process not only improved charge transport but also allowed for deliberate control over copper cluster size and its electronic coupling to the carbon matrix. The resulting materials exhibited distinct structureselectivity relationships: smaller clusters promoted CO accumulation and CC coupling to generate C_{2+} products, while larger metallic domains enhanced the HCOO pathway and formate selectivity. By adjusting carbonization parameters, both activity and selectivity could be tuned in a predictable manner, demonstrating that post-synthetic transformation is a powerful lever for optimizing MOF-derived CO_2RR catalysts.

Taken together, this body of work demonstrates that MOFs are not merely precursors or structural curiosities but highly tunable platforms capable of atomic-level control over catalytic behavior. The results show that product selectivity in CO_2RR can be rationally directed by adjusting metal identity, ligand environment, and coordination geometry to selectively stabilize key intermediates. This is particularly critical for multi-intermediate reactions like CO_2RR, where even subtle changes in local electronic or structural parameters can dramatically alter the product distribution. By combining synthetic control, operando spectroscopy, electrochemical analysis, and theoretical modeling, this research establishes direct links between catalyst composition, crystal structure, and surface-bound species under operating conditions. The framework developed here provides both a fundamental understanding of selectivity in CO_2RR and a practical roadmap for designing the next generation of efficient, selective, and sustainable electrocatalysts.

7.2. RECOMMENDATIONS

While this work contributes to a deeper understanding of structure-selectivity relationships, it also underscores the need for more experimental investigations aimed at validating or refining theoretical descriptors. Future research should focus on bridging the gap between DFT-based predictions and operando observations, as well as developing new frameworks that incorporate electronic band structure, orbital symmetry, and coordination-induced polarization effects as potential selectivity descriptors in CO_2RR.

While fundamental studies such as this may not lead directly to industrial application, their value lies in advancing the mechanistic understanding of CO_2RR at the molecular level. This perspective differs from process-driven CO_2RR research, which focuses on parameters such as reactor design, electrode engineering, operational stability, or scaling strategies. Nonetheless, mechanistic insight remains critical to the long-term development of the technology. Improved understanding of how structure governs selectivity can inform catalyst development across the field.

To maximize impact, future selectivity-focused studies should aim to bridge this gap by designing experiments that, where possible, incorporate industrially relevant electrode materials or architectures. While MOFs offer control over active site geometry and coordi-

nation, their practical deployment is limited by issues such as stability and conductivity. Translating these design principles to more robust systems, such as transition-metal-based catalysts, may require significant synthetic advancements to recreate the same level of atomic precision. Nonetheless, such efforts could yield materials that combine both mechanistic insight and industrial viability, making them valuable candidates for next-generation CO_2RR technologies.

It is also important to acknowledge that the scope of this study was inherently shaped by the structural characteristics of MOF-based catalysts. Due to their atomically isolated catalytic sites, MOFs are predisposed to favour the formation of single-carbon (C_1) products such as CO and formate, while suppressing C-C coupling necessary for generating multi-carbon (C_2^+) species. This site-isolation effect, although beneficial for mechanistic control and intermediate stabilization, imposes a structural constraint that limits the exploration of pathways leading to heavier hydrocarbon products.

As a result, mechanistic studies based on MOFswhile highly informative for understanding the fundamentals of C_1 product selectivity- do not fully capture the complexities associated with producing C_2 and heavier products in CO_2RR. Therefore, any effort to develop universal selectivity descriptors must also consider catalyst platforms capable of promoting C-C coupling. Expanding these studies to include systems such as oxide-derived metals, nanostructured copper, or bimetallic interfaces could offer a more complete framework for rational catalyst design across the full CO_2RR product range.

An additional recommendation is to couple advanced *operando* characterisation with data-driven modelling to capture the *dynamic* nature of active sites under realistic CO_2RR conditions. Static descriptors derived from ex-situ structures often overlook potentialdependent reconstruction, ligand exchange, or phase segregationall of which can fundamentally alter reaction pathways and product distributions. By integrating timeresolved spectroscopy (e.g. quick-scan XAS, *operando* Raman/IR) and high-throughput electrochemical screening with machine-learning algorithms, it should be possible to extract dynamic descriptorsquantities that correlate transient electronic or geometric states with instantaneous Faradaic efficiencies. Such an approach would not only refine catalyst design rules beyond equilibrium structures, but also accelerate the discovery of materials whose selectivity remains robust under fluctuating industrial operating windows.

ACKNOWLEDGEMENTS

Finally, my favorite part of this dissertation. All in all, from where I'm standing, every journey in life is just an opportunity to get to know wonderful people. Starting with, **Peyman**, I don't think I will have enough chances in my life to thank you properly! For now, I'll just use this chance to say how lucky I was to go through one of the most important journeys of one's life under your supervision. Your calm and understanding personality, together with your scientific attitude, helped me figure out each step of this path, and I sometimes can't believe I'm the same person who started this journey. You never hesitated to offer support, even for the smallest problems. Every piece of advice I received along the way helped me build up a character that can now go on (in science and beyond) with more patience and logic. From every bit of confidence I gained to every big accomplishment during this PhD, I see your kind guidance behind it. I keep hoping that I helped your newly well-established group as much as I wanted.

Next, my biggest gratitude to my wonderful promoter, **Arjan**. You were my very first interaction with Dutch people and their culture, the country I called home for a few years. I still remember how lucky I felt after our first meeting, you kindly pointed out that I need to feel more confident and less shy. That was the moment I knew I had ended up in the most understanding group, department, university, and country. During this journey, I only experienced support, kindness, care, and patience. It will always be an honor to have had the chance to be part of your group.

Poloumi, your kind and cheerful attitude, together with your precise guidance through a path that was so far from my understanding, helped me a lot. I truly appreciate this experience and you, for one of the best collaborations of my PhD. The same goes for **Mahinder**. It was absolutely my pleasure to collaborate with you and to use your years' worth of expertise in CO_2 reduction in my projects.

I need to take a few sentences to express my absolute respect for you, **Stefano**. I've always said getting to know you was one of the best strokes of luck during my PhD! Your kind, helpful, caring, and calm personality while being one of the most successful researchers in your field, always reminded me that arrogance has no place in true science. There's not much more success left that I can wish for you given how far you've come, but I can wish that everyone dealing with crystals gets the same chance as me to work with you.

This PhD, due to the nature of my project, gave me the opportunity to meet many wonderful people, one of whom is **Nabil**. I don't know how many times I showed up at your office to ask the simplest (and sometimes, dumbest!) questions and request meetings. Not once

did I feel I was being too much, even though I knew I probably was. That's how lucky I was to have you as a collaborator. You always supported my ideas and patiently found a way to make them work. Your great personality and your ability to make everything possible in your field have always been inspiring to me. **Mohammad** I've always admired your hard work, focus on details, and scientific adaptability. You made many things possible in my PhD projects. Although our shared time in the lab was short, what you did was so impactful that it continued to the final stages of my PhD. **Arianna**, I thank you for saving the day with such efficiency and accuracy. I really appreciate your help and contribution. I want to also thank our TEM collaborator **Majid** for making impossibles possible and for spending time on helping me improve the quality of my work.

Now, it's time for me to thank my favorite bosses in the world. Starting with **Prasad** - not as my colleague, co-author, or group member, but as a friend! Your scientific support made so many things possible in my PhD, but your moral support is something I will never forget. I know I wasn't always on my best behavior when you needed a favor, but you helped me anyway. I started calling you boss as a joke, but really, it came from deep respect for the way you handled everything in the lab with such patience. I hope we always remain friends, boss! And now, as I call the other boss - **Prasaanth**! Your charm always dragged me into your office, whether for a quick chat or to ask for advice. We had our arguments, but deep down I always cared deeply for you and your sweet wife. While writing this, all I can think about is the opportunity we need to find to finally make the other boss drunk, lol!

I want to take a few moments to thank my office mates through the years. I am absolutely not a good office mate, and these guys were so patient having me around all day, mostly listening to loud music and not maybe being as engaging as I always want to be. But I guess you understand that I'm deeply shy, and it sometimes gets in the way. Still, I was super lucky to share my office with the most understanding people, **Maxine**, **Arash**, and **Elsa**, thanks for putting up with me!

But speaking of office mates opens up a chance for me to go on and on about my favourite person in the whole TU Delft time! **Ursa**, you remember our inside joke (I don't deserve it)? You made me think that way many times. You don't know how much fun I had with you around. From you repeating my name in the office to practice, to opening your house to me in my darkest days, to just changing my mind. You and **Matej**, now your little princess **Lisa**, your wonderful parents are my favourite people ever and I appreciate every bit of our meaningful connection.

I want to thank all my group mates in the **CTE group** through the years - **Yaiza**,**Eszter**, **Keer**, **Can**, **Arjan C.**, **Axel**, **Gaoji**, **Radhey**, **Ziyu** and **Joost**. But among CTE members, I want to especially thank **Agnieszka** for all the help, support, and hard work. Your kind and loving nature made working in the electrochemistry labs so easy and stress-free. I want to acknowledge my wonderful Persian friends around the department, **Kaveh**, **Mir**, **Araz**, **Soroush**, **Ehsan**, **Ali**, and **Sanam**. You guys were truly a blessing to have as friends and colleagues. I also want to send my special gratitude to my colleagues around the

department - **Vivi**, **Joep**, **Yeli** (special thanks to you for such a fun fortune-telling evening), **Gautham**, **Tim**, **Mohammad**, **Camila**, **Alice**, **Philip**, **Fabian**, **Konstantina**, and all the other PhDs and postdocs that I had the chance to spend time with. A special thank you to sweet, brave, and wonderful **Hannah**, who was here for such a short time but I'm super happy that we ended up as friends. I also want to thank **Georgy** for such short though encouraging chats all around the department, and **Hans** for his amazing role in taking care of everything around the labs that I mostly worked in, and for his kind assistance in my projects. I also acknowledge **Kees** and **Ruud** for their amazing role in the surface characterization labs. I want to also thank my colleagues in Kortlever's lab, **Ruud**, **Aswin**, **Nandalal**, **Simone** and **Katie** for their valuable scientific input and help during my PhD.

I want to acknowledge and thank **Reina** in the most special way that I can. You are one of the most organised and hardworking people I've met, and yet you always have time for catching up and sharing positive energy. Thank you so much for your assistance during my PhD and all the amazing work.

One of the favourite parts of my PhD was the time I had the chance to work with my sweet master students. **Yu-Bi** and **Jasper**, you guys were amazing! I could never ask for a better experience. I was learning every step myself and you guys patiently walked through it with me. I will always appreciate you two, and I was absolutely thrilled and proud of you, Jasper, when you joined our group as a colleague! I wish both of you the best in your careers - you both deserve it!

Amir, you probably remember I thanked you in your first year as being a handy freshman! Now I need to thank you a thousand times more, not just because you're handy but also because you never hesitated to help me whether in the lab or in life, over the past two years. I don't know how I could have survived this PhD without our every twenty minute breaks :D. Both you and **Reihaneh** are among my most favourite people in my Netherlands life, and I don't say it enough, but I appreciate every moment of having you guys in my life!

Rishabh, you're the one I always go to for anything! Thank you, my friend, for all these years, for standing beside me through the happiest and saddest moments, for being my moral support, and for all the wonderful experiences - even if it was just as simple as going to a museum. And thank you for introducing me to so many amazing people, even my own next-door neighbour! **Francesco**, thank you for helping me to fight the system (the landlord!) and please lose at a board game just once! **Nikos** and **Irini**, you're among my most favourite people in Delft. Thank you for opening your houses to me and for all the fun times during these years. And yes, I want to thank my favourite animals on this planet, just for their existence - **Mr. Spock**, **Mowgli**, **Loki**, **Odin**, **Marilou**, and **Coco**. Taking care of you made my life so much better!

It's time for me to thank the bubble boys, lol! Starting with **Joe**, my walking talking translator. Thank you for dragging me to concerts (and your own gigs), for always taking time to help me with my English, for always insisting on ordering/drinking one more beer,

and for many insightful although sometimes annoying online lectures. **Wouter**, I won't take your time, I know how valuable it is, but I want to thank you for being one of my closest friends through all these years and thank you for not letting me lose my bike, as much as I deserved it! **Nikhelash** (I want you to know that this time is the only time your name is written incorrectly *on purpose*! Traditions are all we have :D), you're my favourite bubble boy, but don't tell the rest! Thank you for joining our friend group and bringing so much philosophical sophistication with you. **Marko**, you're not a bubble boy, but I do want to acknowledge your friendship here (I don't know why, I just think it's kinda funny!). Also, thanks for driving us around in your Tesla to your penthouse! My wonderful friends **Thanos** and **Thomas** (for political reasons I have to use both your real names), I'm super lucky that I had this chance to meet you guys in one of the dumbest places on the planet, psor! But thank you for your company throughout these years and thanks to sweet **Penny** for liking fleabag!

Amirmasoud, I was super lucky to have you as a friend. Going on trips, laughing at weird random internet videos, walking around Delft - all those moments with you and **Raha** remain among my sweetest memories. My dearest **Leila**, I'm so happy I had the chance to meet the wonderful person that you are, and I hope we always end up taking the same flight to Vienna :D. Thank you to sweet **Saeedeh**, we might meet each other a little late, but you are for sure, one of my favorite people in the NL.

Ramin and **Yosra**, you guys are just perfect! Being lucky to have you close all these years and being part of your celebrations made my life so cheerful. I'm so proud of you both for everything you've become, and I do owe part of me standing back on my feet to your support and confidence boosts whenever I needed them. However, there's more to what I think and have learned from you, **Yosra**! I hope I'll always witness that unique strength you carry within you for the rest of my life which I plan to spend as one of your closest friends, if you're okay with that, of course! :D

Mahsa! Acknowledging you might take a bit too long. It's just too many things to be thankful for that I don't even know where to start. I remember all our good times - from the nice food at your house every time I was starving, to the parties you threw for others (not yourself), to all the movies we watched falling asleep on your couch, to all the drinking evenings. But I also remember all the times I felt unseen, depressed, alone, and lost, and you were there like the big sister I never had. I think it's normal to get lucky once in a while in life, but you joining our group and becoming my closest friend here was my best luck in recent years! I always look up to you! As well as you **Masoud (Dr.)**. Thank you for always helping me, for taking me along with you on trips, for being the best cat dad ever :D, for not leaving me to deal with stuff alone, for letting me think I can do it (no matter what), and more importantly, for giving feedback on my terrible life choices!

Fatemeh and **Alireza**, when it comes to old friends, I can't stop thinking about how brutal life is to keep you two thousands of kilometres away from me. Thank you for always being there and for developing such a unique language that only we understand. All the voice messages we share are among the best comedies ever created in human history. I

know life will bring us back together somehow; I just hope it happens soon. My dearest **Mohsen(s)**, **Amirali** and **Keyvan**, you were and always will be some of my favourite people, and I was so lucky to have the chance to call you my friends. I'm proud of you both so much!

Parsa, I know life wasn't quite fair to any of us in some ways, but I've always seen you as my oldest friend and a family member. Thank you for all the good years from the first months of our bachelor's to the final year of our PhD. The constant presence and support of you and your family made my life so much more beautiful. I'm more than proud of what you've become, and I know well how tough the path was. So, in one simple sentence, but with a memory packed from ten years, *keep shining, you crazy diamond!*

I want to acknowledge my old friends from my old university who supported me constantly throughout all these years - my dear **Morvarid**, **Amirreza**, **Hadis**, **Farshad**, **Majid**, **Saeed**, **Razieh**, **Sayeh**, and **Majedeh**. I love you guys so much! But among whom, my dearest **Arash**, thank you for being in my life! Thank you for all the encouragement, for your well-developed sophistication, for all the times you listened to me and gave me incredible perspectives. And more importantly, thank you for all the fun memories which made some of the most surreal moments of one's life, full of joy and life. :D Your kind attitude, charming personality, and open mind are something to learn from.

I'd like to warmly thank my postdoctoral supervisor, **Nick**, for all the kind assistance during my transition to Switzerland, and also for taking the time to read my thesis. With your super busy schedule which I was indeed a witness to in the office, it means a lot to me that you accepted to be part of my committee. Dear **Zahra**, it was such a joy to see you again after all these years in Switzerland. Seeing the wonderful person you've become made me proud to have had the chance to know you. Thank you so much for all your help over the past few months and for all the encouragement. I also want to acknowledge my wonderful colleagues in the **Thin Film and Interface** group at PSI for their warm attitude, which made PSI feel like a second academic home to me during the past few months.

I would also like to acknowledge my committee members, **Prof. Pescarmona**, **Prof. van der Veen**, **Prof. Vlugt**, **Prof. de Jong**, and **Dr. Rossi** for accepting to be part of my defence journey and for their valuable feedback on my thesis.

Starting to acknowledge my family members with **Sheyda**. I probably need at least a year to properly acknowledge 15 years of friendship. I'm thankful for every moment of these years. We've survived so many things in life that I can't even count. And that's my most valuable asset in life. You and your wonderful family are so close to my heart that I can't even imagine life without you. I'm so proud of you, and I'll always wake up, get ready, and walk to work while sending you looooong messages explaining my day. I can promise you that! :D My dear **Amin**, there are certain times in life when I just want to call you and noone else, and tell you what's going on. I might not say it that often, but it's in those moments I realise how lucky I've been all these years to have you as my older brother. Thank you for always asking about my progress, encouraging me, being caring,

and having my back when I needed someone most. **Amir H.**, you are not only my brother - you are the person I always dreamed of becoming. If there's one thing left in this world for me to be proud of, it's you. I can remember every small step of my life - whether it was building character or a career - you were there. And if there are multiple versions of me in multiple universes, I bet you're leading and paving the way for all of them. **Rahman**, you are that cool dad I always brag about. Your kindness, calmness, and intelligence always surprise me - but more than that, I don't think I've ever seen anyone more humble than you. That's the lesson I try daily to learn from you and admired all my life. I'm so proud to be your daughter. And last, **Parvin**! Any woman's journey in life should be an inspiration to other women and yours truly is. If I ever did anything valuable in life, it was because I learned from the best. Every bit of you is made of bravery, confidence, kindness, and independence. I've watched you all these years and never once doubted your strength. You made all our lives easier and helped each of us become who we are, no matter what we wanted. I won't ever be able to thank you enough, mother, but I'm the proudest to be your daughter.

Khatereh Roohi, July 2025 - Delft, The Netherlands

Curriculum Vitæ

Khatereh Roohi

Education

2013–2017	Bachelor of Science in Chemical Engineering Amirkabir University of Technology (Tehran Polytechnic) Tehran, Iran
2017–2020	Master of Science in Catalysis Engineering Amirkabir University of Technology (Tehran Polytechnic)
2021–2025	PhD Candidate in Materials Science and Engineering Delft University of Technology (TU Delft), Delft, The Netherlands *Thesis:* Metal-Organic Frameworks for the CO_2 Reduction Reaction; A Selectivity Study *Promotors:* Prof. dr. ir. A. Mol, Dr. P. Taheri
2025–present	Postdoctoral Researcher, Thin Film and Interface Group, Paul Scherrer Institute (PSI), Villigen, Switzerland

List of Publications

9. **K. Roohi**, J. Coppen, H. Brouwer, A. Mol, P. Taheri, Structure-dependent selectivity for CO_2 reduction on copper clusters supported on carbon derived from Cu-based MOFs, *To be submitted*.

8. **K. Roohi**, N. Khossossi, M. Soleimani, S. Canossa, et al., Metal-organic framework catalysts for disturbing linear scaling relationships and beyond for enhanced selectivity in electrochemical CO_2 reduction reaction, *To be submitted*.

7. **K. Roohi**, S. Mohseni Armaki, N. Khossossi, M. Soleimani, et al., The role of copper coordination in metal-organic frameworks in CO_2RR selectivity, *To be submitted*.

6. **K. Roohi**, J. Coppen, A. Mol, P. Taheri, Metal-organic framework composites as electrocatalysts for carbon dioxide conversion, in: *Applications of Metal-Organic Framework Composites*, Elsevier, 2025, pp. 539565.

5. **K. Roohi**, M. Soleimani, N. Khossossi, S. Canossa, et al., Planar [CuS]-organic framework for selective and low-overpotential CO_2 to formate reduction, *Small Structures*, 2025, 2500235.

4. P. Gonugunta, **K. Roohi**, M. Soleimani, P. R. Anusuyadevi, P. Taheri, M. Ramdin, Screening of binder materials for Ag-based gas diffusion electrodes for CO_2 conversion to CO, *Industrial & Engineering Chemistry Research*, 64(4), 2025, 21132122.

3. M. Amiri, M. Ahmadi, N. Khossossi, P. Gonugunta, **K. Roohi**, et al., Ultra-thin defective TiO_2 films as photocathodes for selective CO_2 reduction to formate, *Journal of Catalysis*, 445, 2025, 116022.

2. A. Kosimov, **K. Roohi**, P. Taheri, N. Kongi, et al., Template-assisted mechanosynthesis leading to benchmark energy efficiency and sustainability in the production of bifunctional FeNC electrocatalysts, *ACS Sustainable Chemistry & Engineering*, 11(29), 2023, 1082510834.

1. F. Jahanmard, A. Khodaei, J. Flapper, O. Dogan, **K. Roohi**, P. Taheri, S. A. Yavari, Osteoimmunomodulatory GelMA/liposome coatings to promote bone regeneration of orthopaedic implants, *Journal of Controlled Release*, 358, 2023, 667680.